Sedimentation and erosion of fluid-solid systems

Laurence Girolami

UNIVERSITY OF TOURS

Faculty of Sciences & Technology

HABILITATION THESIS IN GEOPHYSICS

Sedimentation and erosion of fluid-solid systems

presented by

Laurence Girolami

Associate Professor at the University of Tours

Defended on September, 5^{th} 2025 with the jury composed of :

Pascale Aussillous (President) ..... Professor of University (AMU) - IUSTI
Philippe Claudin (Reviewer) ..... Research Director (CNRS) - PMMH
Éric Lajeunesse (Reviewer) ..... Physicist of Observatory (CNAP) - IPGP
Valérie Vidal (Reviewer) ..... Research Director (CNRS) - ENS
Simonetta Cola (Examiner) ..... Professor of University (UP, Italy) - DCEAE
Mohammed Boussafir (Examiner) ..... Professor of University (UT) - GéHCO

Laboratoire GéHCO
Campus Grandmont
20, Avenue Monge
37200 Tours

Abstract

This manuscript synthesizes the main research investigations that I developed since my arrival as associate professor at the University of Tours. These activities are mainly devoted to the physical modeling of extreme events (pyroclastic flows, lahars), involving particulate suspensions, while seeking to understand how sediments transported in these flows settle, and later in their course, over a broader time and space scale, how these sedimentary reservoirs rearrange when exposed to erosion processes during floods. The hazardous nature of these phenomena may often limit their direct observation through video footages, then requiring the implementation of indirect observation methods as well as the description of the physical processes involved through laboratory experiments to overcome the persistent locks of the literature. The first research project presents the description of the fluidization and sedimentation of particles (of variable size, density, and shape) homogeneously suspended into a viscous fluid (of variable density and viscosity). Experiments of gas-solid and liquid-solid suspensions generated in a non-confined reservoir allowed us to propose a general expression of the particle sedimentation velocity from that determined for an isolated particle falling into a pure fluid at rest to which a density and a viscosity correction are required, such as considering the suspension as an equivalent fluid of similar properties. This universal law, determined in the Stokes flow regime, allowed us to describe the effect of the solid concentration as well as that of the particle inertia on the settling velocity. The particle inertia was also observed to control the minimum concentration of the mixture and thus the limit of the bed stability. The investigation of the bed surface fluctuations allowed us to highlight the propagation of concentration waves within the suspension, traveling from the base to the surface, whose wavelengths seem indicating that the bed becomes unstable when the size of heterogeneities may become of the order of that of the reservoir. The second research project presents the transport and sedimentation behavior of the suspensions once released down the dam-break flume. To describe such experimental free-surface flows, made with gas-solid and

liquid-solid suspensions taken at different concentrations, we proposed a physical model in which the homogeneous mixture travels and settles independently, at constant speed, while ultimately forming a deposit of constant slope which can be predicted from the two characteristic velocities. Numerical simulations indicate that both the kinematics and deposits geometry are satisfyingly captured by the model, provided that the mixture agitation does not disturb the particle deposition considered similar to that developed in a static suspension of same concentration. Once accumulated down the deltaic plain, the sedimentary reservoir is likely to be confronted to reworking during upcoming events of floods and thus to be affected by erosion through internal seepage flows where a part of the soil, especially the fine matrice, can be ultimately transported towards the surface and gives rise to signatures around the diked river. The third research project presents geophysical observations of the river paleo-environment which provides an overview of the geomorphological situation and allowed us to understand the origin of erosion signatures, while representing the starting point for geomechanical simulations. Numerical predictions of the soil erosion, located beneath the river bed and dikes, developed after repeated episodes of floods, allowed us to explain the distribution of leaks, sand-boils, sinkholes along the protected plain and to characterize situations which may question the safety of the hydraulic facility.

Table des matières

General introduction

My research focuses on the physical modeling of extreme events involving particles-laden flows induced by the erosion of fine particles and resulting in the formation of sedimentary deposits. Through the different investigations presented in this manuscript, we seek to understand how these deposits form, in particular how particles transported in natural flows sediment, and later in their course, over a broader time and space scale, how these sedimentary reservoirs rearrange when exposed to erosion processes induced by the circulation of seepage flows during floods. The hazardous nature of these phenomena may often limit their direct observation through video footages, which hinders their understanding and description, while many models of the literature proposed in the framework of geophysical applications include a large number of variables, which do not allow the identification of the key parameters controling the sedimentation and erosion processes. The implementation of indirect observation methods, as well as the reproduction of natural processes in laboratory experiments performed under controlled conditions, thus becomes inescapable to gain insight into the physics of natural flows and to overcome the persistent locks of the literature, in the aim of developing in the near future large-scale simulations for land-use-planning and risk mitigation.

I started working on this topic during my PhD which was devoted to the exploration of small-volume pyroclastic flows induced by the collapse of lava-domes, during which I dedicated a part of this work to the development of a novel experimental device allowing the reproduction of hot suspensions made with fine particles in air. Through three post-doctoral projects, I expanded my scientific perspectives using different approaches (experimental, numerical, theoretical, and naturalist) and interacted with researchers from different disciplines (geosciences, geomechanics, solid and fluid mechanics, physics, applied mathematics, archeology) in various organizations (joint research units, industrial and commercial establishments, public scientific and technological establishments, geological surveys), where I developed national and international collaborations. My research path was then built by following this guideline. Spending my last postdoctoral project in a fluid dynamics laboratory allowed me to broaden my research horizons through a more general

project from which I intended to describe a larger range of geophysical mass flows, then including lahars and submarine avalanches formed in a wider range of situations. In doing so, I started to set up an experimental room upon my arrival at the GéHCO laboratory, through research projects, including a novel dam-break flume equipped with high-speed video cameras, image processing softwares, and a rheometer. The experimental implementation, devoted to the exploration of suspension flows ensuring the sediments transfer along the Earth-Sea transition, required the reproduction of liquid-solid mixtures of well-controlled properties to carefully study the sedimentation processes. The conduction of experiments allowed the acquisition of a unique database gathering together fluidization and sedimentation processes as well as gas-solid and liquid-solid systems, often dealt with separately in the literature, through a physical analysis which allowed their description according to a single, universal law. Once having described in detail the properties of the suspensions, we explored their flowing behavior and surprisingly noticed that the law determined from static systems may remain valid in the flowing regime with a relatively low agitation. From these considerations, we proposed a physical model capable of predicting the suspensions runout and deposits geometry, particularly the deposits slope, that we then implemented in a well suited, simplified shallow-water model including relevant sink terms to simulate experiments. The in-depth validation of this approach requires however the careful exploration of the complete dataset as well as the integration of ongoing measurements of both velocity profiles and sedimentation velocities in the flows.

Once accumulated in the river deltaic floodplain, in the form of a sedimentary reservoir, the future of these deposits may be confronted to reworking during successive episodes of floods and thus to be affected by erosion processes through internal seepage flows which can ultimately appear at the surface and give rise to signatures down the banks of a diked river, in a quite significant manner to question the safety of the facilities. In the aim of describing the origin and distribution of such erosion signatures, I left my area of research expertise to deploy geophysical observations, performed at different scales, in order to draw a general overview of the river environment. These field obser-

vations allowed us to define the geomechanical context, while understanding the origin of such hazardous phenomena, in order to propose a preliminary model capable of reproducing scenarii of successive flooding events during which the geometry of the river bed, affected by the erosion of its fine matrice, may control the distribution of the surface signatures.

The storyline of the manuscript presents the following structure :

· Chapter 1 presents a novel description of the fluidization and sedimentation velocity of homogeneous particulate suspensions made with different types of materials and fluids, in the Stokes flow regime, and describes the transition towards the unstable regime.

· Chapter 2 proposes a novel physical description of suspension flows, performed with different types of materials and fluids, able to predict their runouts and deposits shape, and presents numerical simulations based on a shallow-water approach.

· Chapter 3 presents a novel description of internal erosion signatures, guided by geophysical observations performed around a diked river, and proposes numerical simulations of the erosion of its paleo-environment during repeated episodes of floods.

· Chapter 4 presents my career path and the research activities developed from my PhD and describes the main students supervision I made since my arrival as associate professor at the University of Tours.

· Chapter 5 presents a brief summary of the research findings and associated perspectives.

· Appendice 1 presents the french summary of the manuscript.

Chapitre 1

Fluidization and sedimentation of homogeneous suspensions

This chapter concerns the following works :

• Sedimentation of gas-fluidized particles with random shape and size (2019) by L. Girolami & F. Risso, *Physical Review Fluids*, 4, 074301, doi :10.1103/PhysRevFluids.4.074301.

• On the fluidization/sedimentation velocity of a homogeneous suspension in a low-inertia fluid (2021) by A. Amin, L. Girolami, F. Risso, *Powder Technology*, 391, 1-10, doi :10.1016/j.powtec.2021.05.073.

• Fall of a large sphere in a suspension of small fluidized particles (2022) by A. Amin, L. Girolami, F. Risso, *Physical Review Fluids Letters*, 7, L082301, doi :10.1103/PhysRevFluids.7.L082301.

• Dynamics and sedimentation of liquid-solid suspensions (2022) by A. Amin, *PHD Thesis*, Université de Tours, tel-04589465.

• Propagation of concentration waves in liquid-solid fluidized beds (2025) by L. Rousseau, L. Girolami, F. Risso, M. Boussafir, *Physical Review Fluids*, in revision.

Abstract

This chapter deals with the fluidization and sedimentation of fine, non-cohesive powders into a viscous, non-confined suspending fluid. We present a fluidization/sedimentation law for the case of homogeneous mixtures which allowed us to gather the results obtained with gas-solid and liquid-solid suspensions thanks to the introduction of a relevant Stokes number which describes the effect of the particle inertia on their fall velocity. We also describe the velocity of a large sphere sinking into the suspension by considering the mixture as an equivalent fluid described by the density and effective viscosity of the suspension. The Stokes number also controls the limit of stability of the mixture, which is attributed to the development of ascending concentration waves in the suspension.

Keywords : Fluidization and sedimentation velocity, particulate suspensions, gas-solid and liquid-solid mixtures, fluidized beds, homogenous and stable regime, particle inertia, limit of stability, concentration waves.

1.1 Introduction

Natural concentrated suspensions involve different types of sediments and fluids for a wide range of particle concentrations. Some of the most common examples include basal pyroclastic flows, non-colloidal mudflows and lahars, submarine avalanches and turbidity currents. Since they are loaded with particles heavier than the suspending fluid, solid components progressively settle throughout the mixture during propagation. As the suspensions spread through a global motion, where the fluid and particles travel at the same speed, the sedimentation velocity appears to not being disturbed by the flow [Girolami *et al.* (2008); Girolami & Risso (2020)], which allows us to explore it independently. Due to its long time scale, the sedimentation process turns out to control the suspension lifespan, so that the mixture stops flowing when the two phases are separated. Describing in detail the sedimentation velocity appears thus essential to model the stopping phase of

short-lived, devastating events dominated by sedimentation.

In the literature, many efforts have been devoted to the investigation of viscous suspensions where both the fluid and particle inertia, respectively described by the Reynolds and the Stokes number, are negligible ($Re \ll 1$ and $St \ll 1$) [Koch & Hill (2001)]. In these cases, suspensions are commonly generated in narrow tubes [Richardson & Zaki (1954)], with neutrally-buoyant systems [Guazzelli (2024)], close to the dilute regime [Batchelor (1972)] or the packing state [Abrahamsen & Geldart (1980)], involving colloids [Banchio *et al.* (1999)] or cohesive powders [Castellanos *et al.* (2001)], distinguishing fluidized beds [Zhang *et al.* (2023)] from particulate suspensions [Davis (1993)], and more commonly separating gas-solid systems [Fan & Zhu (1999)] from liquid-solid ones [Guazzelli & Pouliquen (2018)]. The effect of the Stokes number has thus not been really explored in the literature. To decouple its influence to that of the Reynolds number (*i.e.* the particle inertia from that of the fluid) on the particle settling velocity, the investigation of gas-solid suspensions becomes unavoidable, due to their low Re and their large density ratio between the two components $\frac{\rho_s+1/2\rho_f}{\rho_f}$, which implies a range of conditions for which the Stokes number remains important ($St \geq \mathcal{O}(1)$) [Koch & Hill (2001)]. To preserve the possibility of describing homogeneous suspensions, particles involved in the mixture must be fine, but non cohesive, to extend the limit of the bed stability. Moreover, exploring a broader range of the Stokes number requires the investigation of liquid-solid suspensions for which the density ratio $\frac{\rho_s+1/2\rho_f}{\rho_f}$ implies smaller St ($St \ll 1, St \simeq \mathcal{O}(1)$), which is necessary for a complete description of the sedimentation velocity U_{sed} in the low Reynolds-number regime.

In this chapter, we focus on the case of viscous suspensions made with fine, non-cohesive, rigid, inertial powders that sediment in the Stokes regime ($Re < 1$, $10^{-2} < St < 10^3$) into a Newtonian fluid. Suspensions are prepared in aid of fluidization techniques, which allows us to generate homogeneous mixtures of controlled density and solid concentration, and to measure the fluidization velocity U_f in addition to that of sedimentation U_{sed}. The reservoir is taken large enough compared to the particle diameter ($\frac{d_p}{x_0} \ll 1$)

to consider the boundary effects as negligible and get a symmetric problem in which $U_f \simeq U_{sed}$ through a change of reference frame. Then, from simple measurements of U_f, of the bed dilatation ($E = \frac{h_s}{h_p} = \frac{\Phi_{pack}}{\Phi_s}$), and of the solid volume fraction at packing Φ_{pack}, we can infer the solid volume fraction of the suspension Φ_s, the mixture density ρ_m and the sedimentation velocity U_{sed} in homogeneous cases. Using fine particles makes however the suspension opaque which limits its visualization through techniques of adjustment of optical indices, thus requiring alternative methods to investigate the motion of a macroscopic object immersed into the suspension. The observation of the free-surface can also provide informations on the bed height fluctuations.

The motivation of this work was guided by the determination of a sedimentation law as universal as possible, at low Reynolds number, for homogeneous suspensions involving different types of solid particles (of different shape, size, density) and fluids (gas and liquid), covering a wide range of solid concentrations, and not affected by any boundary effect. The description of the suspension dynamics also allows to understand and predict how a large object moves within the mixture, as well as why and when the bed destabilizes.

1.2 Fluidization and sedimentation processes

One of the specificities of this work is to generate particulate suspensions in aid of fluidization techniques. This method allows us to obtain well calibrated mixtures, whose solid volume fraction Φ_s is carefully deduced from the measurements of both the mixture expansion and the solid volume fraction of the bed at packing Φ_{pack}. The principle of experiments consists in uniformly injecting a fluid at the base of a loosely packed bed made with solid particles randomly poured in a reservoir (Figure 1.1). Different fluidization regimes are observed depending on the fluid velocity U_f and the conditions of operation [Rhodes (1998); Fan & Zhu (1999)]. When U_f is weak, the vertical stream of fluid passes through the interstitial voids let by the particles without modifying the state of the bed, as in a non-deformable porous medium. In this state, the bed thickness remains static while

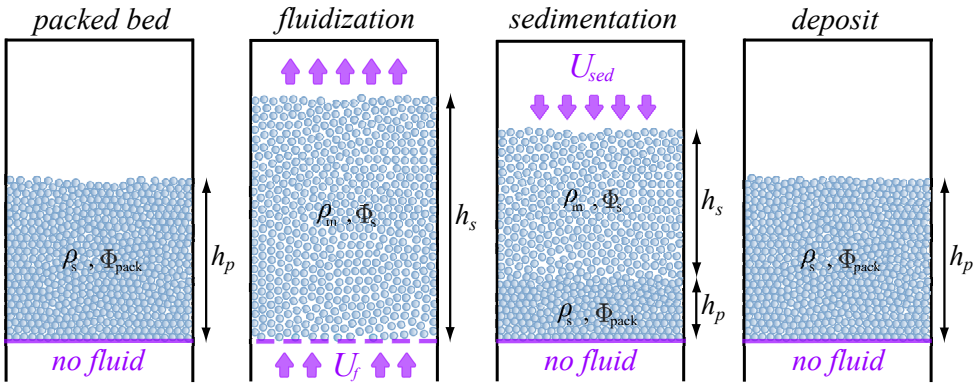

Figure 1.1

Fluidization and sedimentation processes applied to a bed of particles : the packed bed, the particulate fluidization associated with a bed expansion, the mixture sedimentation, the deposit.

the jump in fluid pressure across the bed increases linearly with the fluidization velocity since the drag force exerted on particles is dominated by viscous stresses proportional to U_f (Figure 1.2).

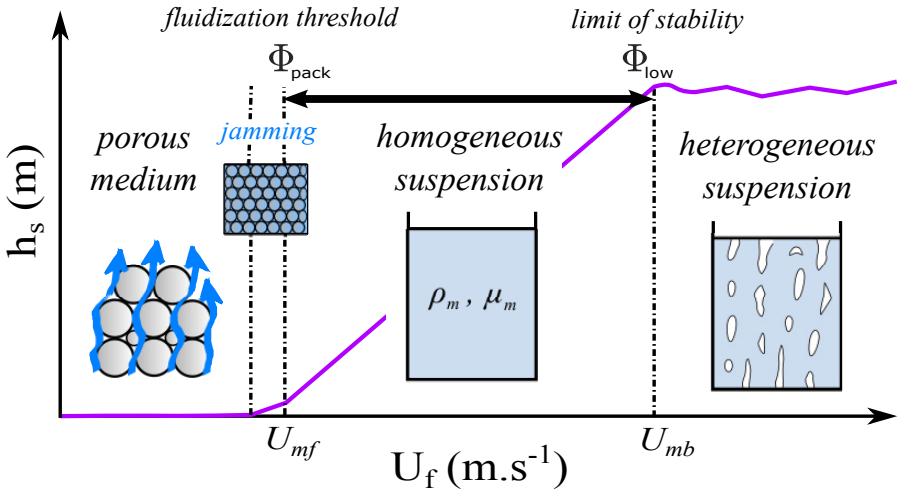

Figure 1.2

Suspension height h_s as a function of the fluidization velocity U_f pointing the limits of the homogeneous regime obtained from the point of minimum fluidization and the point of minimum bubbling ($U_{mf} < U_f < U_{mb}$).

When U_f is increased further and reaches the point of minimum fluidization U_{mf}, the drag force balances gravity, so that particles are no more in contact with each other and become suspended, as described by the viscous term of the semi-empirical equation of Ergun (1952), which corresponds to the Kozeny-Carman equation :

$$U_{mf} = \frac{g(\rho_s - \rho_f){d_p}^2}{150\mu_f} \left[\frac{(1-\Phi_{pack})^3}{\Phi_{pack}}\right], \tag{1.1}$$

Above U_{mf}, the mixture forms a dense, homogeneous suspension that uniformly expands with U_f, and whose maximum dilatation rate depends on the fluid and grains properties (Figure 1.2). In this state, the fluid velocity is commonly described by the empirical formulation of Abrahamsen & Geldart (1980) :

$$U_f = U_{mf} + \frac{g(\rho_s - \rho_f){d_p}^2}{210\mu_f} \left[\frac{(1-\Phi_s)^3}{\Phi_s} - \frac{(1-\Phi_{pack})^3}{\Phi_{pack}}\right], \tag{1.2}$$

This homogeneous regime, also termed *particulate fluidization*, is observed until the point of minimum bubbling U_{mb} above which cavities and concentration gradients, formed at the surface of the distributor plate, rise and coalesce, such as making the fluidization unstable. The minimum bubbling velocity U_{mb} is described by the empirical formulation of Abrahamsen & Geldart (1980), as :

$$U_{mb} = U_{mf}\left(\frac{\Phi_{pack}}{\Phi_{low}}\right)\left(\frac{1-\Phi_{low}}{1-\Phi_{pack}}\right)^3. \tag{1.3}$$

where Φ_{low} represents the mixture expansion at the point of minimum bubbling, which can also be used to predict the limit of stability $\frac{\Phi_{low}}{\Phi_{pack}}$ of the homogeneous regime, solely obtained with fine, light, and non-cohesive powders. Geldart (1973) determined an empirical classification to distinguish the different fluidization regimes observed with gas-solid systems according to the particle diameter d_p and the density contrast between the particles and the fluid $\rho_s - \rho_f$ (Figure 1.3). In this way, only fine, light and non-cohesive powders, belonging to the group A of the classification, can be uniformly fluidized above U_{mf} and significantly expanded above the packing state, thus forming suspensions characterized by a wide range of solid volume fractions Φ_s. Cohesive particles, belonging to

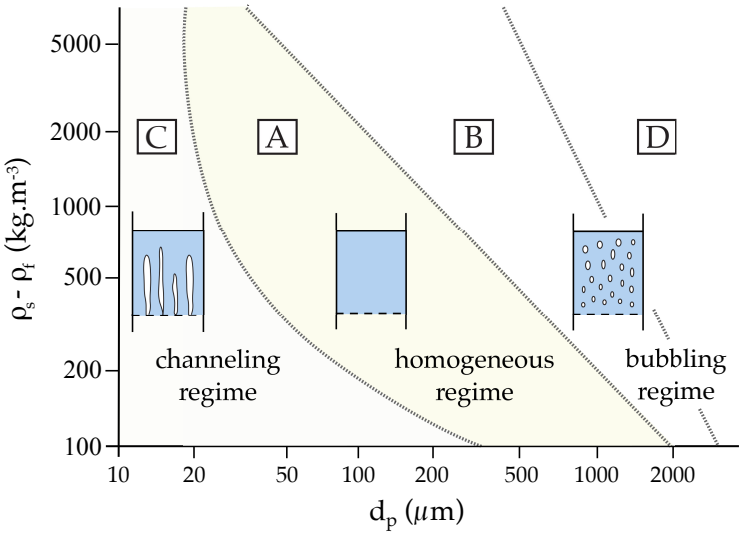

Figure 1.3

Fluidization regimes determined for gas-solid systems at room temperature [Geldart (1973)].

the group C, turn out to be not fully fluidizable at room temperature since the gas flows through channels across the most permeable regions of the bed to form fluidization chimneys. Otherwise, large and heavy particles, belonging to the groups B and D, expose a bubbling regime directly observed at the point of minimum fluidization, so that no particulate regime can develop with these materials ($U_{mf} = U_{mb}$). This chapter thus focuses on homogeneous suspensions, solely obtained with fine particles.

After fluidization, when the fluid supply is cut abruptly, the suspension surface sediments progressively at a velocity U_{sed} and forms a loose deposit that progressively aggrades from the base at a velocity U_{agg_0} (Figure 1.1). When boundary effects are negligible, the velocity U_{sed} at which the particles move through the static fluid at a given solid volume fraction Φ_s is expected to be identical to that at which the fluid moves through the static particles U_f by a Galilean transformation [Richardson & Zaki (1954); Girolami & Risso (2019)].

The terminal velocity of a single particle that falls into a viscous, infinite fluid at rest was first theoretically described by Stokes (1851) for $10^{-4} < Re = \frac{\rho_f(U_p - U_f)d_p}{\mu_f} < 0.2$ from

the balance of the reduced weight of the particle and the drag force acting on it :

$$U_0 = \frac{g(\rho_s - \rho_f){d_p}^2}{18\ \mu_f}, \tag{1.4}$$

The problem becomes however more complicated when the number of particles is sufficiently large to consider the system as a sedimenting suspension. When the bodies are evenly dispersed throughout the fluid, their sedimentation velocity decreases and it is of inescapable interest to quantitatively describe the relation between the mixture concentration and the magnitude of this decrease. Maude & Whitmore (1958) then proposed a theoretical expression of the mean sedimentation velocity at small Reynolds numbers ($Re < 10^{-1}$) for suspensions made with small, identical rigid spheres characterized by a wide range of solid volume fraction taken however reasonably far from the packing state :

$$U_{sed} = U_0 \left(1 - \Phi_s\right)^{\beta}, \tag{1.5}$$

where $\beta \simeq 5$ for $Re < 10^{-1}$, but requires some experimental adjustments for higher Reynolds numbers. Batchelor (1972) developed afterwards an analytical expression of U_{sed}, with no adjustable parameters, for dilute, homogeneous suspensions made with small, rigid, identical spheres randomly distributed in the dispersion characterized by a solid volume fraction Φ_s quite inferior to unity, that first includes appropriate combinations of two-body hydrodynamic interactions, so that :

$$U_{sed} = U_0 \left(1 - 6.55\Phi_s\right), \tag{1.6}$$

Al-Naafa & Selim (1992) validated experimentally this expression for suspensions made with small, spherical, rigid, monodisperse particles, provided that $\Phi_s < 0.03$. Reed & Anderson (1980) continued this approach by providing an approximate pairwise theory to micron size particulate suspensions that includes long range forces (*i.e.* electrostaticity and Van der Waals attractions) for more concentrated mixtures ($\Phi_s < 0.4$) that agrees remarkably well with experimental data, as :

$$U_{sed} = U_0 \left(\frac{1 - 1.83\Phi_s}{1 + 4.70\Phi_s}\right), \tag{1.7}$$

Beyond this analytical framework, theoretical predictions present however some practical limitations and can suffer from a lack of universality, especially to gather together experimental measurements made with different types of solid particles (of variable size, density and shape), different types of suspending fluids (of variable density and viscosity), and covering a reasonable range of solid volume fraction (from the dilute regime to the packing state). To overcome this issue, Richardson & Zaki (1954) developed a series of fluidization and sedimentation experiments, performed in narrow tubes, that involved different spherical particles and liquids for a wide range of Reynolds numbers and solid volume fractions, taken however reasonably far from the packing state and the dilute regime, from which they formulated a very popular expression of U_{sed}, such as :

$$U_{sed} = U_i \left(1 - \Phi_s\right)^n , \tag{1.8}$$

where U_i is supposed to be the terminal fall velocity of a single particle in a pure infinite fluid at rest, but whose value may however be affected by the ratio between the particle diameter and that of the reservoir d_p/x_0 (ranged from 5.10^{-3} to 2.10^{-1} in their experiments) or the Reynolds number, while n depends on the Reynolds number, so that $n = 4.65$ for $0.2 < Re < 1$ and $n = 2.4$ for $1 < Re < 500$. Maude & Whitmore (1958) then used this experimental data set to adjust the exponent of equation (1.5) as $2.33 < \beta < 4.65$ for $10^{-2} < Re < 10^4$. More recently, Castellanos *et al.* (2001) proposed an extension of this law (1.8) for dense gas-solid suspensions made with cohesive powders in which adhesive forces become dominant and lead to the formation of aggregates that tend to increase the settling velocity relatively to that predicted for individual particle (1.8), such as :

$$U_{sed} = \frac{N}{k} U_0 \left(1 - \Phi_{\text{eff}}\right)^n , \tag{1.9}$$

where Φ_{eff} represents the solid volume fraction occupied by the aggregates, taking $\Phi_{\text{eff}} = \left(\frac{k^3}{N}\right) \Phi_s$, N is the number of particles per aggregate, and $k = \frac{d_A}{d_p}$ represents the ratio between the mean aggregates diameter d_A and the mean particle diameter d_p.

When the effect of the fluid inertia becomes important, the terminal velocity of a single particle falling into an agitated fluid is similarly determined from the balance of the

reduced weight of the particle and the drag force acting on it, taking the drag coefficient of the Newton range which amounts to $C_D = 0.44$ for $500 < Re < 2.10^5$, and yields :

$$U_0^t = \sqrt{3\left(\frac{\rho_s - \rho_f}{\rho_f}\right) g d_p}. \tag{1.10}$$

In suspensions made with small rigid spheres, particles act as obstacles and hinder the fluid flow, thus effectively increasing the measured viscosity. The change in viscosity is commonly analyzed in shear-flow configurations, where the suspension usually placed in a cylindrical vessel is submitted to a constant shear rate induced by the rotation of an immersed spindle. Experiments consist in measuring the torque needed to a constant angular velocity and to infer the suspension rheology from the shear stress and the normal stress differences which both depend on the shear rate and the solid volume fraction.

Einstein (1906) first assumed that the first-order effective change in viscosity in dilute dispersions, in which solid spheres are scarce and sufficiently well separated ($\Phi_s < 0.03$), should only depend on the solid volume fraction and not on their distribution, thus neglecting their interactions with each other which would relegate non-Newtonian effects to higher-order corrections. In doing so, Einstein (1906, 1911) related the viscous dissipation induced macroscopically by the flow of a suspension of effective viscosity μ_m, considered as homogeneous, with that locally induced by the presence of an isolated particle into a pure shear fluid of viscosity μ_f, such as :

$$\frac{\mu_m}{\mu_f} = 1 + 2.5\Phi_s + \mathcal{O}(\Phi), \tag{1.11}$$

The popular theoretical relation (1.11) states that a dilute suspension behaves to a first-order as a Newtonian equivalent fluid of viscosity greater than that of the suspending fluid. The increase in solid volume fraction acts in narrowing the streamlines near the particles, giving rise to an increase in energy dissipation and thus in viscosity. Batchelor & Green (1972) introduced a second-order correction to account for the pairwise hydrodynamic interactions that become dominant in more concentrated dispersions ($\Phi_s < 0.1$), such as :

$$\frac{\mu_m}{\mu_f} = 1 + 2.5\Phi_s + 7.6\Phi_s^2 + \mathcal{O}(\Phi^2), \tag{1.12}$$

When the solid volume fraction increases further ($\Phi_s \geq 0.2$), the distance between particles become smaller than their radius, making the description of the macroscopic behavior much more complex. In this framework, many empirical formulations have been proposed over the last decades to describe the suspension viscosity relatively to that of the fluid. Among them, the most popular expressions include that of Maron & Pierce (1956), which writes :

$$\frac{\mu_m}{\mu_f} = \left(1 - \frac{\Phi_s}{\Phi_{pack}}\right)^{-2}, \tag{1.13}$$

or that of Krieger & Dougherty (1959) in which the power exponent depends on the packing state of the involved material, such as :

$$\frac{\mu_m}{\mu_f} = \left(1 - \frac{\Phi_s}{\Phi_{pack}}\right)^{-B\Phi_{pack}}, \tag{1.14}$$

where $B = 2.5$ is the Einstein's coefficient. Frankel & Acrivos (1967) then used an asymptotic technique to derive the functional dependence of μ_m with the solid volume fraction for suspensions of uniform, rigid spheres in the limit of the packing regime. Their expression, devoted to dilute dispersions, does not involve ajustable parameters, such as :

$$\frac{\mu_m}{\mu_f} = \frac{9}{8}\left[\frac{\left(\frac{\Phi_s}{\Phi_{pack}}\right)^{\frac{1}{3}}}{1 - \left(\frac{\Phi_s}{\Phi_{pack}}\right)^{\frac{1}{3}}}\right]. \tag{1.15}$$

Good agreements were found between the asymptotic solution (1.15) and experimental data, provided that Φ_{pack} is determined in each experiment. However, to date no expression exists to reliably describe the fluidization or sedimentation velocity, as well as the effective viscosity, for a wide range of particles sizes, densities and shapes, for different types of fluids, and for a wide range of particle concentrations.

1.3 Dimensional analysis

The description of the fluidization and sedimentation processes, that involve fine solid particles of variable size, density and shape homogeneously suspended into a fluid, involves

7 independent physical parameters, listed as follows : the mean particle diameter d_p, the solid density including the added mass of fluid displaced with the particle (here considered as spherical) $\rho_s + \frac{1}{2}\rho_f$, the reduced weight of the particle $g(\rho_s - \rho_f)$, the fluid density ρ_f, the fluid viscosity μ_f, the solid volume fraction of the suspension Φ_s, the maximum solid volume fraction of the material at packing Φ_{pack} (here measured from a loose deposit). These parameters involve three dimensions ($[L]$, $[T]$, $[M]$) that lead us to build $7 - 3 = 4$ non-dimensional groups to describe the system, such as :

(1) the solid volume fraction Φ_s that describes the mixture concentration ;

(2) the solid volume fraction normalized by its value at packing $\frac{\Phi_s}{\Phi_{pack}}$ that ranges from 0 to 1 and corresponds to the inverse of the expansion rate $\frac{h_s}{h_p}$, which characterizes the microstructure of the interstices within the suspension and ranges from 0 to 1 ;

(3) the Reynolds number $Re = \frac{\rho_f d_p U}{\mu_f}$, based on the mean particles diameter d_p and the fluidization or sedimentation velocity U, that accounts for the role of the fluid inertia relatively to the viscous stresses ;

(4) the Stokes number $St = \frac{(\rho_s + \frac{1}{2}\rho_f) d_p U}{\mu_f}$, also based on the mean particles diameter d_p and the fluidization or sedimentation velocity U, that characterizes the particle inertia relatively to the fluid viscous forces.

Particles involved in the present gas-solid experiments are however characterized by a mean diameter of around $65\mu m - 80\mu m$, thus belonging to the group C of the Geldart's classification [Geldart (1973)], which highlights the necessity of considering also cohesive powders in the present analysis. Their fluidization and sedimentation behavior is then disturbed by adhesion/repelling forces F_c (such as van der Waals, electrostatic, capillary forces) and the formation of aggregates, which leads to a more complex, possibly heterogeneous, problem defined by two additional independent non-dimensional groups, such as :

(5) the aggregates size ratio $k = \frac{d_A}{d_p}$ which compares the mean aggregates diameter to the mean particle diameter ;

(6) the granular Bond number $Bo_g = \frac{F_{ad}}{W_p}$ which compares the adhesion/repelling

force to the particle weight $W_p = \rho_s \frac{\pi}{6} d_p^3 g$ [Giraud *et al.* (2020)]. Here, van der Waals forces are expressed by $F_{vdW} = \frac{H_A}{24 z_0^2} \overline{d}_p$, where the Hamaker constant $H_A = 1.5.10^{-19} J$, $\overline{d}_p = \frac{2 d_{p_1} d_{p_2}}{d_{p_1} + d_{p_2}} = d_p$ for monodisperse powders, the minimum contact distance between two particles $z_0 = 0.2 \mu m$ is given by the typical size of their asperities [Massimilla & Donsì (1976); Castellanos *et al.* (2001)] ; capillary forces are given by $F_c = \sigma \pi r_i \left(\frac{r_i}{r_o} + 1 \right)$, where σ is the surface tension, r_o : the outer radius of the liquid bridge, and r_i : the neck radius of the liquid bridge [Pu *et al.* (2021)] ; and electrostatic forces which express as $F_E = k_e \frac{q^2}{z_0^2}$, where q represents the mean electrical charge of the particles and $k_e = 9.10^9 N.m^2.C^{-2}$ [Coulomb (1785)] ;

as well as,

(7) the solid volume fraction $\phi_{\text{eff}} = \left(\frac{k^3}{N} \right) \Phi_s$ modified by the formation of aggregates.

Since particles used in these experiments were uncharged electrically, electrostatic forces can be considered as negligible. The finest particles ($d_p = 65 \mu m$), fluidized by air, experience van der Waals forces $F_{vdW} = 10^{-11} N$ much smaller than their weight $W_p = 2.10^{-9} N$, giving rise to a characteristic granular Bond number $Bo_g = 5.10^{-3}$ quite inferior to unity, highlighting the negligible effect of interparticle forces. The same materials expose however capillary forces $F_c = 5.10^{-6} N$ much greater than their weight, giving rise to a granular Bond number $Bo_g = 2.10^3$ upper than unity, highlighting the dominant effect of capillary bridges between particles. To vanish these adhesion effects in gas-solid suspensions, particles were carefully dried at high temperature (180^{o}C) during 24h before experiments, while the fluidizing air and reservoir walls were both heated at the same temperature to ensure a homogeneous fluidization during experiments. In this way, even the finest particles behaved as fine, non-cohesive powders that uniformly and significantly expand above loose packing (similarly to the group A of the Geldart's classification), such as fluidization and sedimentation processes can be described by the four relevant non-dimensional groups : Φ_s, $\frac{\Phi_s}{\Phi_{pack}}$, Re, and St.

The use of different types of solid particles and fluids in experiments allowed us to

vary the solid concentration over a wide range of values ($0.05 \leq \Phi_s/\Phi_{pack} \leq 0.97$) from the dense regime to the dilute one. Figure 1.4 exposes the order of magnitude of both the Reynolds number and the Stokes number characteristic of these experiments. We can observe that Re remains small, from 5.10^{-3} to 5, with most of the values less than 0.5, while approaching unity for some experiments performed with the largest glass beads and water. Otherwise, St varies over a broader range of values, from 2.10^{-2} to 50, while approaching 0.5 10^2 for experiments made with volcanic ash and air, with most of the values greater than 5. These observations suggest that the effects related to the fluid

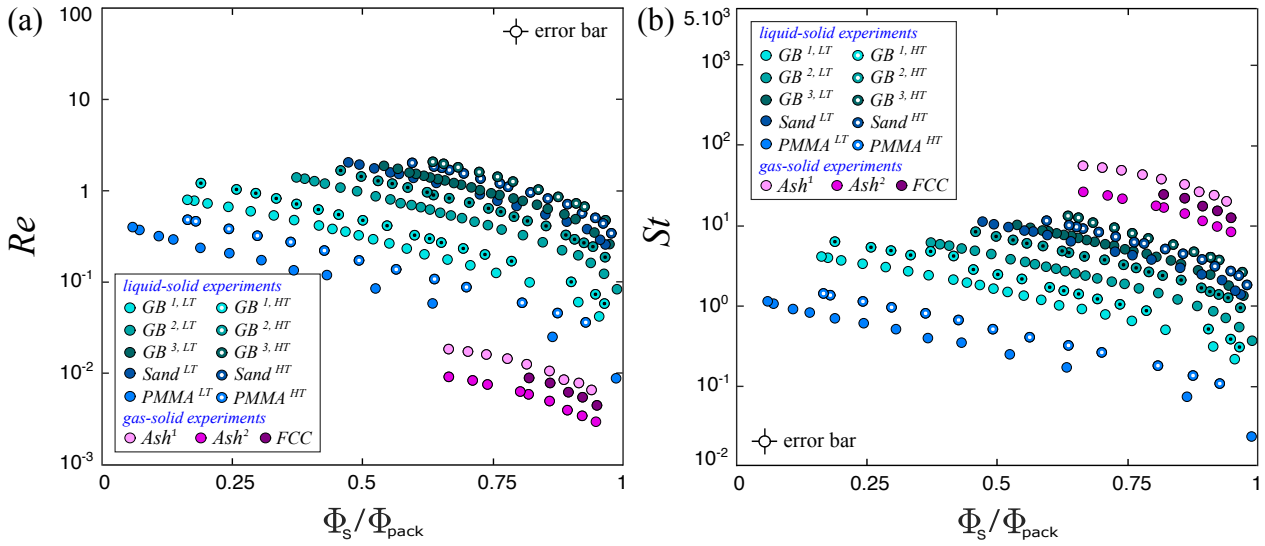

Figure 1.4

(a) Particles Reynolds number $\mathcal{R}e$ and (b) Stokes number $\mathcal{S}t$ as a function of Φ_s/Φ_{pack}.

inertia may be negligible compared to those related to the particle inertia on both the fluidization and sedimentation velocities and allow us to discard from Re in the follow of this analysis, thus reducing the description of U_f, U_{sed} as a function of Φ_s, $\frac{\Phi_s}{\Phi_{pack}}$, and St.

Moreover, taking the theoretical Stokes velocity $U_0 = \frac{g(\rho_s-\rho_f)d_p^2}{18\ \mu_f}$ as characteristic velocity comes down to writing the Stokes number, henceforth termed St_0, as $St_0 = \frac{g(\rho_s+\frac{1}{2}\rho_f)(\rho_s-\rho_f)d_p^3}{18\ \mu_f^2}$ that only depends on the grains and fluid properties, which avoids to involve adjusting parameters. We can also notice that $St_0 = \left(\frac{\rho_s+\frac{1}{2}\rho_f}{\rho_f}\right) Ar$, where Ar, the

Archimede number, compares the inertia of gravity-induced motions to viscous forces. In this way, the description of both fluidization and sedimentation processes lies on the three relevant non-dimensional groups : Φ_s, $\frac{\Phi_s}{\Phi_{pack}}$, St_0.

Beyond the Geldart's classification which separates gas-solid from liquid-solid suspensions, as in most of the studies of the literature, through a dimensional repartition of different mixture behaviors, the presentation of particulate suspensions may be first lied on the solid concentration $\frac{\Phi_s}{\Phi_{pack}}$ that will distinguish dilute dispersions from concentrated suspensions ; then the granular Bond number Bo_g that will distinguish heterogeneous mixtures of aggregates built from cohesive powders from homogeneous suspensions of fine, non-cohesive particles ; thus the Reynolds number Re_0 (based on U_0 which also corresponds to the Archimede number Ar) that will distinguish viscous suspensions to inertial ones (involving larger particles such as those of groups B and D of the Geldart's classification and water) ; and finally the Stokes number St_0 that will distinguish suspensions made with inertialess particles (as passive tracers) from those made with highly agitated inertial particles. All of these non-dimensional parameters allow the description of the particle motion into a fluid, when disturbed by these effects, relatively to the idealized case of a single particle that moves into a pure, viscous, infinite fluid at rest, described by the Stokes velocity U_0.

1.4 Homogeneous fluid-solid suspensions

In experiments, we used different types of solid particles, taken here much finer (from a few dozens to a few hundreds of microns) than those commonly employed in experiments of fluidized beds devoted to physical, engineering or industrial applications, as well as different types of suspending fluids (air and water) which require some technical constraints in each case. Gas-solid suspensions, made with synthetical or natural powders ranged from 65 μm to 80 μm, require an operation temperature greater than 150^oC to vanish cohesive forces attributed to the air moisture [Girolami (2008)]. Therefore, particles were

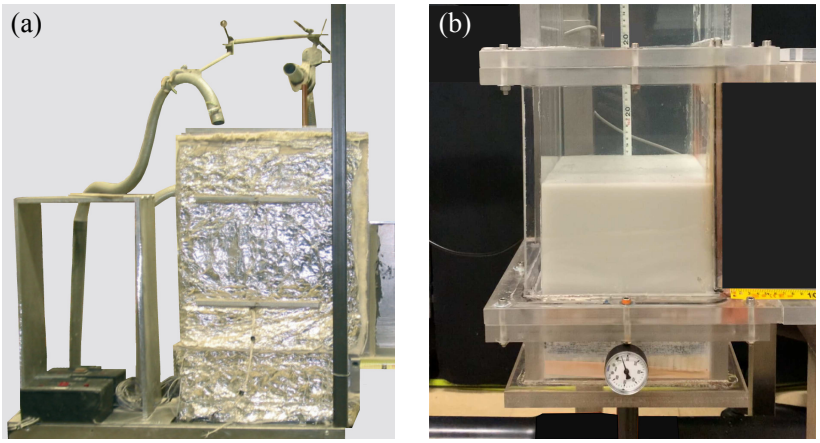

Figure 1.5

Picture of the fluidization rig used in (a) gas-solid suspensions and (b) liquid-solid suspensions.

dried during 24h at 200^oC before experiments, then introduced into a reservoir with walls heated at 180^oC and fluidized by air also heated at 180^oC (Figure 1.5a). In doing so, fine, angular or spherical particles were homogeneously fluidized and significantly expanded above loose packing. On the other hand, liquid-solid suspensions made with synthetical or natural particles, ranged from 160 μm to 335 μm and performed at room temperature (from 15^oC and 35^oC), require a closed-loop operation system as well as a well-calibrated porous medium beneath the reservoir to ensure a homogeneous fluidization (Figure 1.5b) [Amin (2022)].

In experiments, the mean particle diameter d_p, determined from the grain size distribution reported on Figure 1.6, varied by a factor 5 from the finest particles to the largest ones. The solid density ρ_s varied by a factor 2 from the lighter particles to the heaviest ones, while the particle shape varied from a spherical geometry to an angular one (Figure 1.6). As we used both air and water in experiments, the fluid density varied over three orders of magnitude, while its viscosity varied over 2 orders of magnitude. The choice of such materials and fluids allowed us to vary the mixture concentration $\frac{\Phi_s}{\Phi_{pack}}$ from 0.05 to 0.97, such as covering as well the dense regime as the dilute one. The physical properties of the particles, fluids and suspensions are summarized in Table 1.1. Measurements

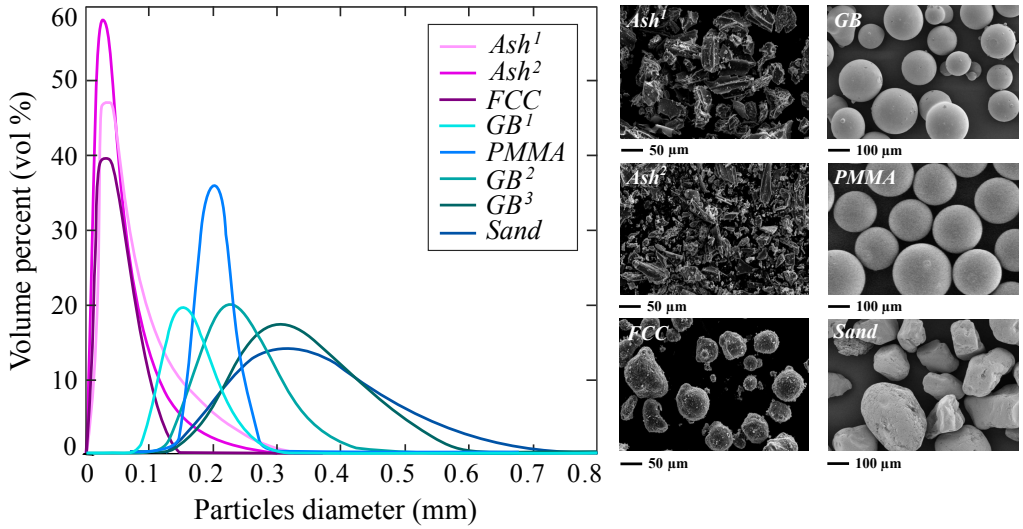

Figure 1.6

Particle size distribution and pictures of the microscopic materials used in the experiments.

Parameters	FCC-A	Ash^1-A	Ash^2-A	PMMA-W	GB^1-W	GB^2-W	GB^3-W	Sand-W
d_p [μm]	70	80	65	200	160	240	335	320
ρ_s [kg.m^{-3}]	1420	1600	1490	1200	2500	2500	2500	2650
ρ_f [kg.m^{-3}]	0.80	0.80	0.80	10^3	10^3	10^3	10^3	10^3
μ_f [Pa.s]	10^{-5}	10^{-5}	10^{-5}	10^{-3}	10^{-3}	10^{-3}	10^{-3}	10^{-3}
Φ_s	0.47-0.55	0.40-0.53	0.42-0.55	0.03-0.63	0.09-0.57	0.22-0.58	0.31-0.57	0.26-0.56
$\frac{\Phi_s}{\Phi_{pack}}$	0.82-0.95	0.70-0.92	0.71-0.92	0.05-0.92	0.16-0.95	0.37-0.96	0.54-0.95	0.47-0.96
$\frac{\rho_s+1/2\rho_f}{\rho_f}$	1775	2000	1860	1.7	3	3	3	3.15
St_0	650	1200	550	1.2	10	35	95	85

Table 1.1

Experimental parameters of gas-solid suspensions made with chemical catalysts (FCC) or volcanic ash (Ash^1 ; Ash^2) with air (A) both heated at 180^{o}C ; and of liquid-solid suspensions made with PMMA, glass beads (GB^1 ; GB^2 ; GB^3), or sand with water (W) taken at 15^{o}C and 35^{o}C.

of both the suspension and the deposit heights as a function of time were first made in liquid-solid suspensions composed of GB[1] and water taken at 20^oC, at a solid concentration $\frac{\Phi_s}{\Phi_{pack}} = 0.67$ and shows that the suspension surface progressively sediments at constant velocity U_{sed}, leaving a loose deposit of solid volume fraction Φ_{pack} at the base that progressively thickens at constant velocity U_{agg_0} (Figure 1.7), which means that both sedimentation and aggradation processes can be described by the mean velocity of the upper and lower interface respectively that merge at the end of experiment. Measurements

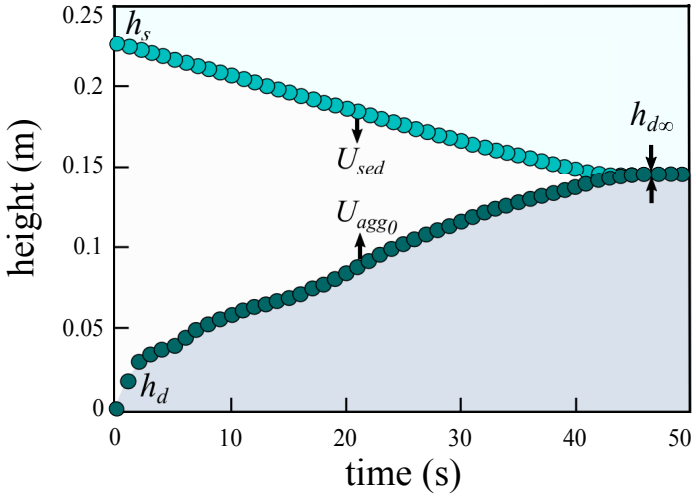

Figure 1.7

Suspension height h_s and deposit thickness h_d as a function of time t during the sedimentation of a liquid-solid suspension made with GB^1 and water W at a solid concentration $\frac{\Phi_s}{\Phi_{pack}} = 0.67$.

of the mean fluidization and sedimentation velocities, performed with gas-solid suspensions involving FCC or volcanic ash (Ash^1 ; Ash^2) with air both heated at 180^oC and with liquid-solid suspensions involving PMMA, glass beads (GB^1 ; GB^2 ; GB^3), or sand with water taken at 15^oC or 35^oC are plotted with the solid concentration normalized by its maximum value at packing $\frac{\Phi_s}{\Phi_{pack}}$ (Figure 1.8). As observed in Figure 1.8, the velocity U_f at which the fluid passes through a bed of static particles is equal to the velocity U_{sed} at which particles fall through a static fluid, which is expected and reveals that wall effects do not play a significant role in these experiments, where the particle diameter d_p was

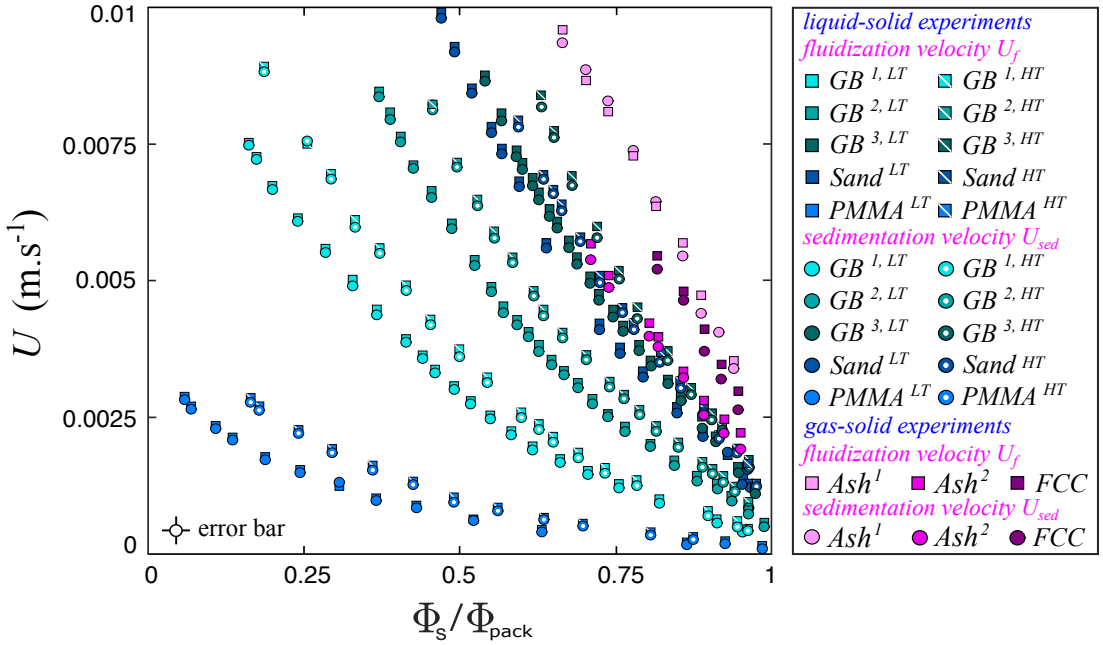

Figure 1.8

Fluidization velocity U_f and sedimentation velocity U_{sed} represented as a function of the normalized solid volume fraction $\frac{\Phi_s}{\Phi_{pack}}$ for both gas-solid and liquid-solid suspensions.

chosen much smaller than the reservoir length x_0, such as $\frac{d_p}{x_0} = \mathcal{O}(10^{-4}\text{-}10^{-3})$. These mean velocities are also observed to decrease with increasing $\frac{\Phi_s}{\Phi_{pack}}$, when both the density and the effective viscosity of the mixture increase. One of the aim of the work of Ahmad Amin during his PhD, that I supervised, under the direction of Florentina Moatar (DR. INRAe, RiverLy, Lyon) then consisted in defining a general law to predict these mean velocities U for different types of particles, fluids, and for a wide range of solid concentrations of the mixture $\frac{\Phi_s}{\Phi_{pack}}$, from the dense regime to the dilute one, in the low Reynolds-number regime.

1.5 Predicting U with popular empirical laws

In this way, we first tested the famous relation (1.2) proposed by Abrahamsen & Geldart (1980) in our experimental data. This law emerges from experimental measure-

ments of U_f in fluidized beds and aims at extending the semi-empirical expression (1.1) of Ergun (1952) that describes the fluidization threshold in saturated porous media to gas-solid suspensions, then taking into account the role of the solid volume fraction Φ_s on U_f. Expression (1.2) involves an adjustable parameter U_{mf}, which has to be determined experimentally, and for which we employed our measurements so that predictions necessarily match with our data when $\Phi_s \to \Phi_{pack}$. Figure 1.9 exposes predictions of equation (1.2) for both gas-solid and liquid-solid suspensions, presented in the manner of Abrahamsen & Geldart (1980). First, we can observe that predictions follow satisfactorily well the trend

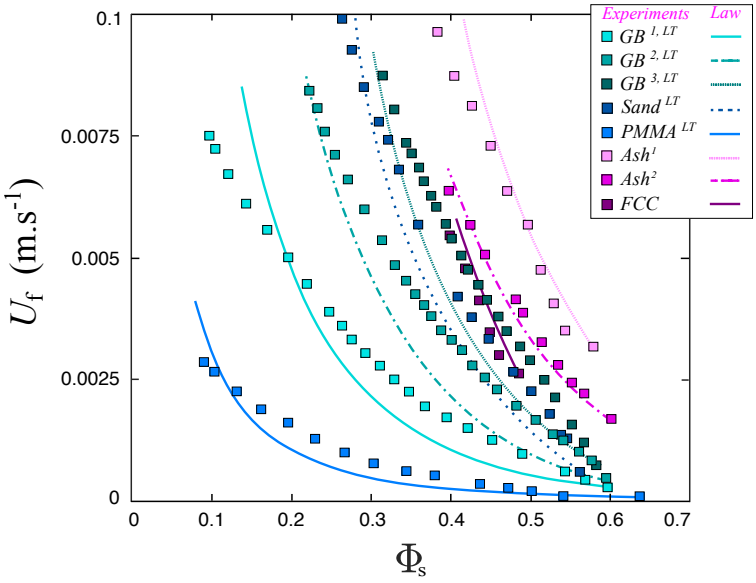

Figure 1.9

Fluidization velocity U_f as a function of the solid volume fraction Φ_s. Plain lines represent the prediction of Abrahamsen & Geldart (1980) (equation (1.2)) for both gas-solid and liquid-solid suspensions.

of U_f for gas-solid suspensions, represented by pink tones in this figure, *i.e.* close to the packing state. However, predictions fail to reproduce the trend for liquid-solids suspensions, represented by blue-green tones, *i.e.* far from the packing state, when $\frac{\Phi_s}{\Phi_{pack}} \leq 0.75$. This law, that involves an adjustable parameter U_{mf}, turns out to be reasonable close to

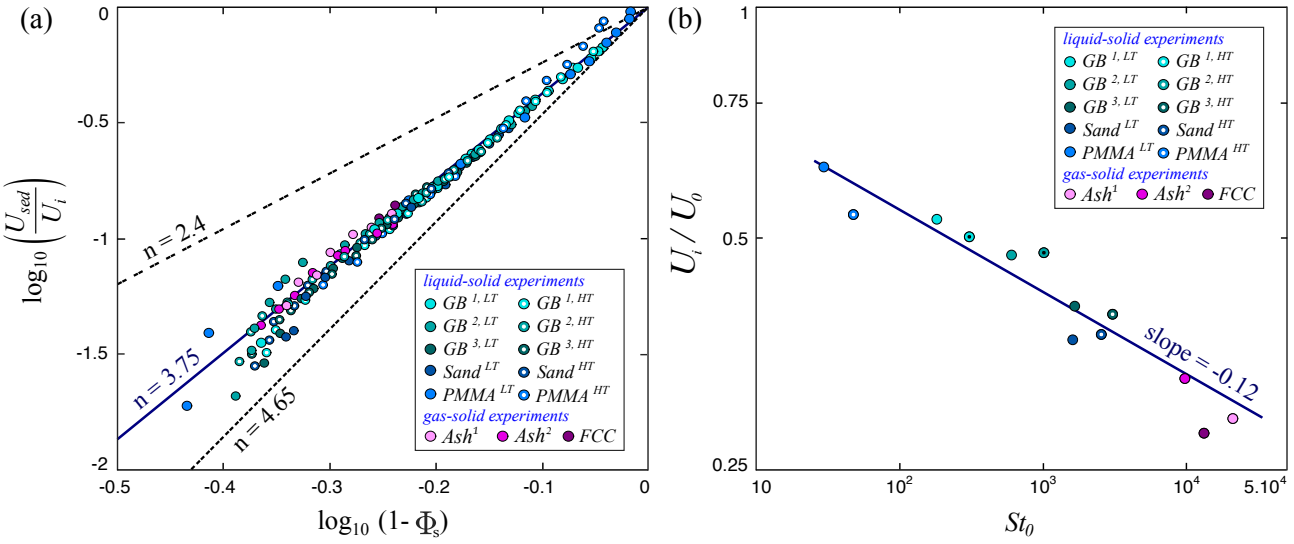

Figure 1.10

(a) Decimal logarithm of U_{sed} normalized by U_i as a function of the decimal logarithm of the bed porosity ; (b) Velocity U_i normalized by U_0 as a function of the Stokes number $\mathcal{S}t_0$.

the packing state but can not predict U_f for a wide range of particle concentration.

Testing now the very popular approach of Richardson & Zaki (1954) in our data. Their empirical relation (1.8) emerges from experimental measurements of U_{sed} in liquid-solid suspensions made with different types of spherical powders at different flow regimes (the viscous regime : $0.2 < Re < 1$ and the agitated one : $1 < Re < 500$). The proposed law (1.8) aims at extending the terminal fall velocity of a single particle to liquid-solid suspensions, then taking into account the role of the solid volume fraction Φ_s on the mean particle velocity U_{sed}. The law thus depends on two adjustable parameters : U_i and the exponent n which depends on Re and $\frac{d_p}{x_0}$ ranged from 5.10^{-3} to 2.10^{-2} in their experiments. Figure 1.10a exposes predictions of equation (1.8) for both gas-solid and liquid-solid suspensions, presented in the manner of Richardson & Zaki (1954) in their reference work. The value of U_i was chosen such as ensuring that $U_{sed} \to U_i$ when $\Phi_s \to 0$ (*i.e.* $\log_{10}\left(\frac{U_{sed}}{U_i}\right) \to 0$ when $\log_{10}(1-\Phi_s) \to 0$). In this way, our experimental measurements roughly gather on a master line characterized by a slope of 3.75, which does not correspond to that mentioned

by Richardson & Zaki (1954), where $n = 4.65$ for $Re < 1$ and approaches $n = 2.4$ for $Re > 1$ (see dashed lines of slopes 2.4 and 4.65 on Figure 1.10a), which is not so surprising when considering the large number of exponents that have been reported in the literature [Kramer *et al.* (2019)]. We can also observe that both the dense regime, here defined by $0.97 \leq \frac{\Phi_s}{\Phi_{pack}} \leq 0.78$ (*i.e.* by $-0.44 \leq \log_{10}(1-\Phi_s) \leq -0.30$) and the dilute regime, here defined by $\frac{\Phi_s}{\Phi_{pack}} \leq 0.1$ (*i.e.* by $\log_{10}(1-\Phi_s) \leq -0.08$) are not satisfactorily predicted, contrary to moderate concentrations, provided that the slope n is correctly adjusted with the data. More importantly, U_i was observed to not correspond to the theoretical Stokes velocity U_0. Plotting U_i normalized by U_0 highlights that this ratio is not equal to unity, while depending on the third non-dimensional group St_0 as pointed by the Figure 1.10b, which lacks from their analysis in which ρ_s does not appear among the list of parameters. To conclude, the Richardson-Zaki's approach allows the modeling of the data, provided that n and U_i −which depend on St_0− are suitably adjusted to our data, and that we renounce to describe the evolution of U_{sed} at small or large concentrations.

1.6 A more universal approach

As the most famous laws of the literature are not able to reliably predict the mean fluidization and sedimentation velocity, termed U in the follow of this chapter, for a wide range of solid concentrations as well as taking into account the effect of the particle inertia described by St_0 on U, we seek gathering our experimental data, which unusually bring together gas-solid and liquid-solid suspensions, according to a general law which depends on Φ_s, $\frac{\Phi_s}{\Phi_{pack}}$, St_0, valid in the homogeneous regime for a low inertia fluid.

In doing so, let's consider the case of a single particle that sediments into a homogeneous, equivalent fluid doted with the same properties than those of the suspension, namely in term of the mixture density $\rho_m = \Phi_s\rho_s + (1-\Phi_s)\rho_f$ and effective viscosity μ_m. This comes down to rewriting the Stokes velocity (1.4) as :

$$U = \frac{g(\rho_s - \rho_m){d_p}^2}{18\ \mu_m}, \tag{1.16}$$

Taking first into account the mixture density ρ_m in our analysis amounts at multiplying U_0 (1.4) by the decreasing function $(1-\Phi_s)$ which involves the first non-dimensional group, such as :

$$U_{ref} = U_0(1-\Phi_s) = \frac{g(\rho_s-\rho_m){d_p}^2}{18\ \mu_f}, \tag{1.17}$$

since $(\rho_s-\rho_f)(1-\Phi_s) = \rho_s-\rho_m$. Plotting the ratio $\frac{U}{U_{ref}}$, which also corresponds to $\frac{\mu_f}{\mu_m}$: the viscosity of the fluid normalized by that of the mixture increased by the solid concentration and the particle agitation, as a function of $\frac{\Phi_s}{\Phi_{pack}}$ exposes that the curves are affine (Figure 1.11a), thus following the same trend, so that they can collapse when multiplying each of them by a constant which depends on St_0. This means that the larger the particles or the denser relatively to the suspending fluid, the greater their inertia and their agitation, the more energy they dissipate, the less will be their settling velocity relatively to that of inertialess particles. This effect is described by the decreasing function $\mathcal{F}_2(St_0)$ (Figure 1.11b), which involves the third non-dimensional group, meaning that $\frac{U}{U_{ref}} = \mathcal{F}_1\left(\frac{\Phi_s}{\Phi_{pack}}\right)\mathcal{F}_2(St_0)$ [Amin *et al.* (2021)]. Now taking into account this effect in our non-dimensionalization, which amounts at dividing $\frac{U}{U_{ref}}$ by $\mathcal{F}_2(St_0)$, allows us to gather together all the measurements of U on a master curve which henceforth exposes the effect of the solid concentration $\frac{\Phi_s}{\Phi_{pack}}$ on U through the decreasing function $\mathcal{F}_1\left(\frac{\Phi_s}{\Phi_{pack}}\right)$. This leads to the following general expression :

$$U = U_0 \underbrace{(1-\Phi_s)}_{\text{mixture density}} \underbrace{\mathcal{F}_1\left(\frac{\Phi_s}{\Phi_{pack}}\right)\mathcal{F}_2(St_0)}_{\text{mixture effective viscosity}}, \tag{1.18}$$

$$\mathcal{F}_1\left(\frac{\phi_s}{\phi_{pack}}\right) = \frac{1}{\exp\left(1.9\frac{\Phi_S}{\Phi_{pack}}\right) + 0.85\left(\frac{\Phi_S}{\Phi_{pack}}\right)^2\left(1-\frac{\Phi_S}{\Phi_{pack}}\right)^{-2/3}}, \tag{1.19}$$

$$\mathcal{F}_2(St_0) = \frac{\frac{St_0}{45}+1}{\frac{3St_0}{45}+1}. \tag{1.20}$$

So, considering that the homogeneous suspension behaves as an equivalent fluid of density ρ_m and effective viscosity μ_m, we can describe the mean fluidization and sedimentation velocities U from that of a single particle U_0 to which we have to include the effect of

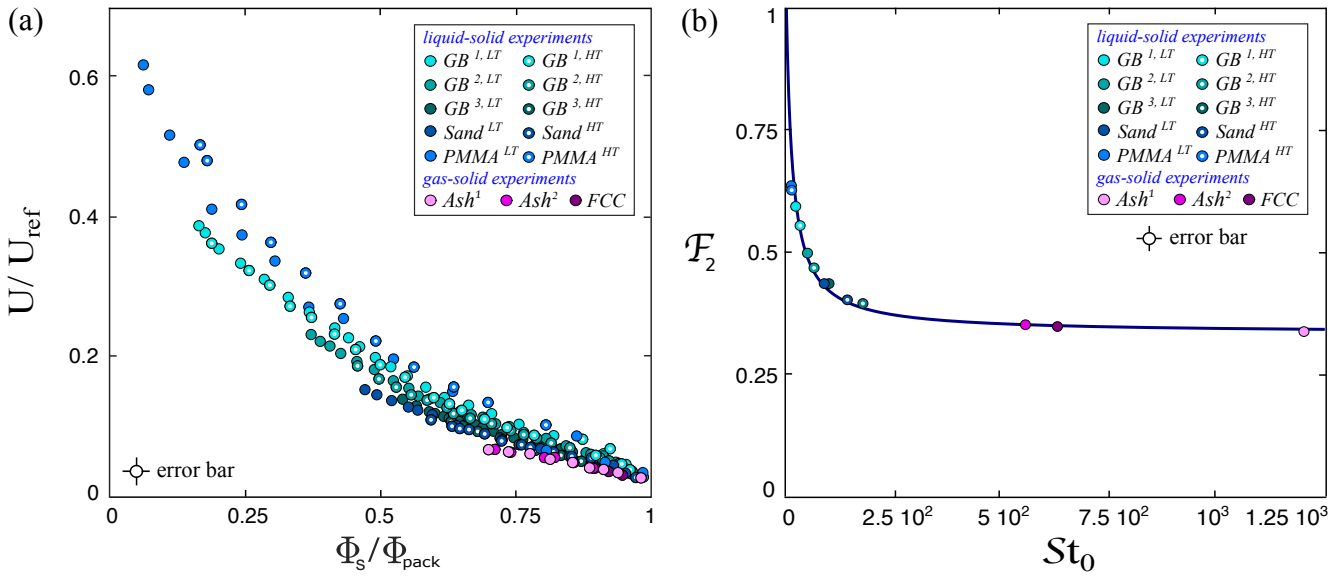

Figure 1.11

(a) Mean velocity U normalized by $U_{ref} = U_0(1-\Phi_s)$ as a function of $\frac{\Phi_s}{\Phi_{pack}}$. (b) $\mathcal{F}_2\,(St_0)$ describes the effect of the particle inertia on U_{sed}.

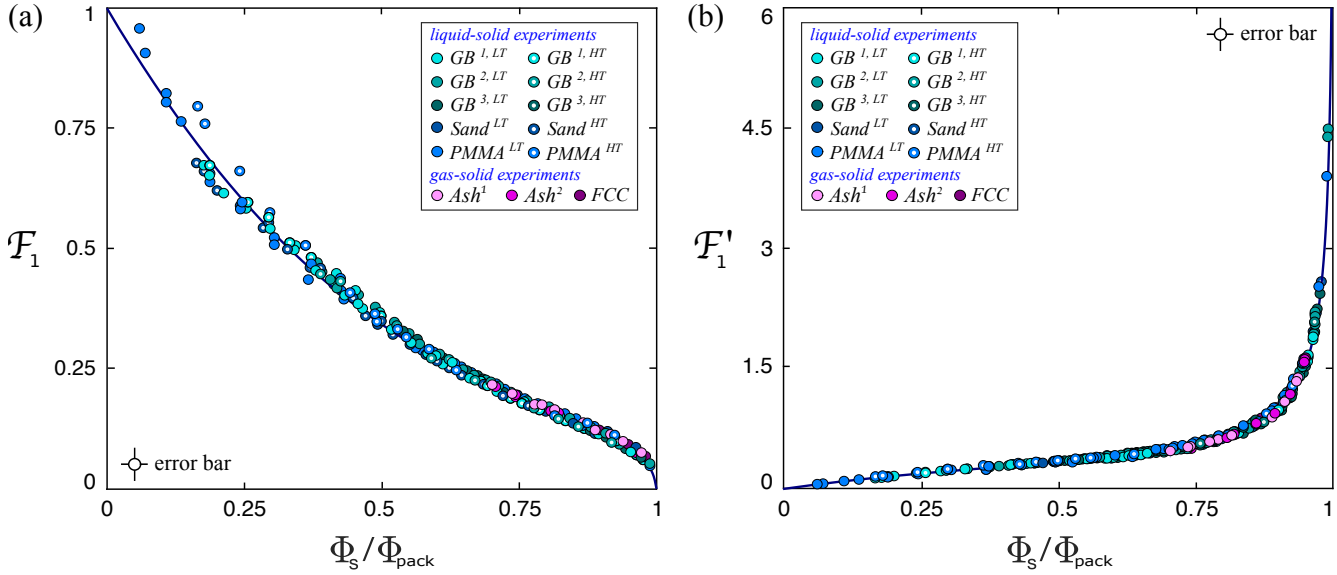

Figure 1.12

(a) $\mathcal{F}_1\left(\frac{\Phi_s}{\Phi_{pack}}\right) = \frac{U}{U_{ref}\mathcal{F}_2(St_0)}$ describes the effect of the mixture concentration on U_{sed}. (b) $\mathcal{F}_1' = \frac{\mathcal{F}_1}{\left(\frac{\Phi_{pack}}{\Phi_s}-1\right)}$ as a function of $\frac{\Phi_s}{\Phi_{pack}}$.

the mixture density ρ_m that affects the buoyancy force acting on each particle and which is described by the decreasing function $(1-\Phi_s)$ which involves the first non-dimensional group, as well as the effect of the mixture effective viscosity μ_m that affects the drag force acting on each particle which both includes the effect of the particle concentration, described by the decreasing function $\mathcal{F}_1\left(\frac{\Phi_s}{\Phi_{pack}}\right)$ that involves the second non-dimensional group, and the effect of the particle inertia, described by the decreasing function $\mathcal{F}_2\left(St_0\right)$ which involves the third non-dimensional group. Each effect are described by independent functions that both act in decreasing U relatively to the idealized case of a single particle. This law also admits two limits. For inertialess particles, the mean velocity reduces to $U = U_0\ (1-\Phi_s)\ \mathcal{F}_1\left(\frac{\Phi_s}{\Phi_{pack}}\right)$, so that when $\Phi_s \to 0 : U = U_0$, imposing that $\mathcal{F}_1\left(0\right) = 1$; while when $\Phi_s \to \Phi_{pack} : U = 0$, implying that $\mathcal{F}_1\left(1\right) = 0$. Note that $\mathcal{F}_1\left(\frac{\Phi_s}{\Phi_{pack}}\right)$ is described by an exponential law at low Φ_s followed by a usual divergent power law at high Φ_s commonly employed in the literature [Richardson & Zaki (1954)]. In between, the term proportional to $\left(\frac{\Phi_s}{\Phi_{pack}}\right)^2$ allows the asymptotic matching, such as remaining weak close to the dilute regime while tending towards unity at the packing state (Figure 1.12a). As particle inertia can not be neglected in these experiments (where $\frac{\rho_s+1/2\rho_f}{\rho_f} \gg 1$, see Table 1.1), equation (1.18) includes the effect of the particle agitation through $\mathcal{F}_2\left(St_0\right)$, which requires taking $\mathcal{F}_2\left(0\right) = 1$ to respect the Stokes velocity, while $\mathcal{F}_2\left(\infty\right) \to \frac{1}{3}$, which highlights a saturation effect at high Stokes numbers (Figure 1.11b).

The mean deposit aggradation velocity U_{agg_0} can be expressed from U through the mass conservation under the assumption of a constant Φ_s with time and space, such as :

$$U_{agg_0} = \frac{U}{\left(\frac{\Phi_{pack}}{\Phi_s} - 1\right)}, \tag{1.21}$$

In this way, Figure 1.12b expose the mean values of U_{agg_0}, deduced from (1.21), similarly gathered on a master curve, expressed by :

$$U_{agg_0} = U_0\ (1-\Phi_s)\ \mathcal{F}_1'\left(\frac{\Phi_s}{\Phi_{pack}}\right)\mathcal{F}_2\left(St_0\right), \tag{1.22}$$

$$\mathcal{F}_1'\left(\frac{\Phi_s}{\Phi_{pack}}\right) = \frac{\mathcal{F}_1\left(\frac{\Phi_s}{\Phi_{pack}}\right)}{\left(\frac{\Phi_{pack}}{\Phi_s} - 1\right)}. \tag{1.23}$$

Now dividing (1.17) by (1.16) leads to $\frac{U_{ref}}{U} = \frac{\mu_m}{\mu_f}$ which allows us to determine the mixture effective viscosity μ_m, here considered as an equivalent fluid. As exposed in (1.18), the increase in viscosity relatively to that of the suspending fluid μ_f depends on $\mathcal{F}_1\left(\frac{\Phi_s}{\Phi_{pack}}\right)$ and $\mathcal{F}_2\left(St_0\right)$, such as :

$$\mu_m = \frac{\mu_f}{\mathcal{F}_1\left(\frac{\Phi_s}{\Phi_{pack}}\right)\mathcal{F}_2\left(St_0\right)}. \tag{1.24}$$

In the same way, first plotting the ratio $\frac{\mu_m}{\mu_f}$ as a function of $\frac{\Phi_s}{\Phi_{pack}}$ expose that the curves are affine, following the same trend (Figure 1.13a), so that they can collapse when multiplying each of them by a constant which depends on St_0 (Figure 1.11b). Now including $\mathcal{F}_2\left(St_0\right)$ in our non-dimensionalization, thus plotting $\left(\frac{\mu_m}{\mu_f}\right)\mathcal{F}_2\left(St_0\right)$ as a function of $\frac{\Phi_s}{\Phi_{pack}}$ allows us to gather together measurements on a master curve which illustrates the effect of the solid concentration on the increase of viscosity. This effective viscosity μ_m, here termed viscosity of sedimentation, describes the viscous dissipation at the micro-scale associated with the shear rate of the flow in the interstices due to the particle settling by gravity, which is determined through the average drag force on particles. This viscosity must however not be confused with the effective shear viscosity related to either the relative motion between particles and defined through the mixture average shear [Useo (2024)] or a concentration gradient through the mechanism of shear-induced migration [Leighton & Acrivos (1987)]. This explains why the viscosity μ_m described by (1.24) [Amin *et al.* (2021)] can not be correctly described by models developed in shear-flow configurations (Figure 1.13b).

Then, we can reasonably wonder whether μ_m, which characterizes the viscous stresses at the scale of the particles, is relevant to describe the macroscopic behavior of the suspension when sheared at a scale considered as large compared to d_p [Hinch (1977); Girolami & Risso (2019)]. To answer this question, experiments consisting of releasing a macroscopic

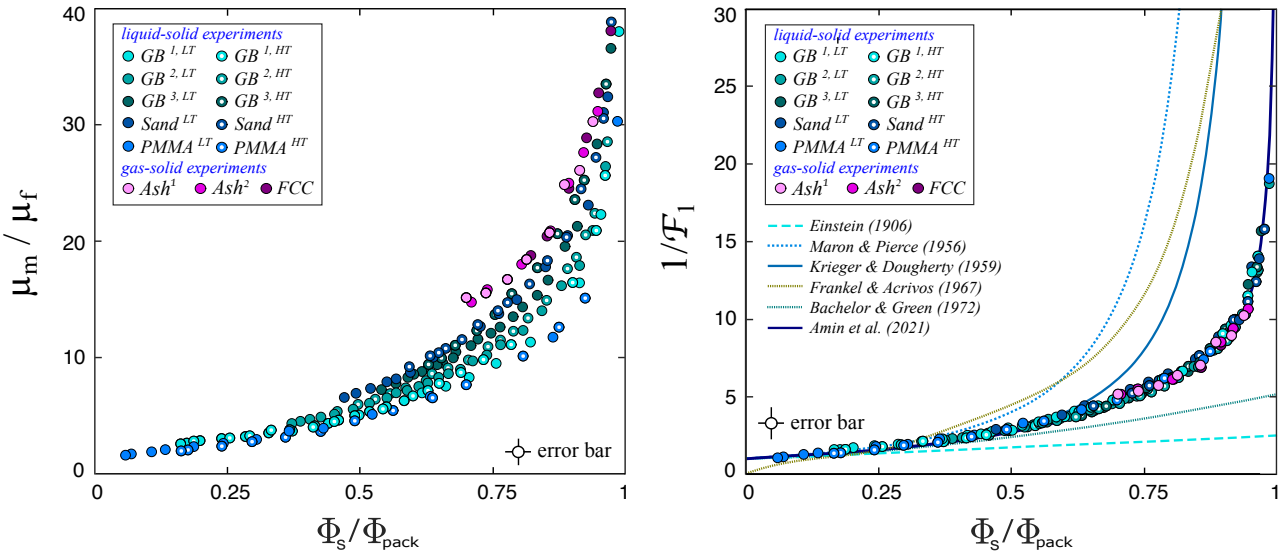

Figure 1.13

(a) $\frac{\mu_m}{\mu_f} = \frac{1}{\mathcal{F}_1\left(\frac{\Phi_s}{\Phi_{pack}}\right)\mathcal{F}_2(St_0)}$ as a function of $\frac{\Phi_s}{\Phi_{pack}}$. (b) $\frac{\mu_m}{\mu_f}\mathcal{F}_2\left(St_0\right) = \frac{1}{\mathcal{F}_1\left(\frac{\Phi_s}{\Phi_{pack}}\right)}$ as a function of $\frac{\Phi_s}{\Phi_{pack}}$. This law is compared with those of the literature.

sphere of density ρ_D and of variable diameter D (taking $7.10^{-3} \leq \frac{d_p}{D} \leq 3.10^{-2}$, see Tables 1.1 ;1.2) into the fully fluidized suspension, made with $GB^1 - W$, $GB^2 - W$, $GB^3 - W$ or $Sand - W$ (see Table 1.1), were initiated during the Spring 2021 as a part of the PhD work of Ahmad Amin (2022). Since the suspension was opaque, a thread of nylon of negligible weight was attached to the sphere, whose length was adjusted so that the sphere sinks within the suspension until the thread is taut. Experiments were recorded using a high-speed video camera calibrated at a rate of 1000 frames per second. The terminal fall

Sphere properties	S_1	S_2	S_3
Diameter D [mm]	12.2	15.7	22.4
Density ρ_d [kg m]	2640	2600	2500

Table 1.2

Physical properties of the sinking sphere.

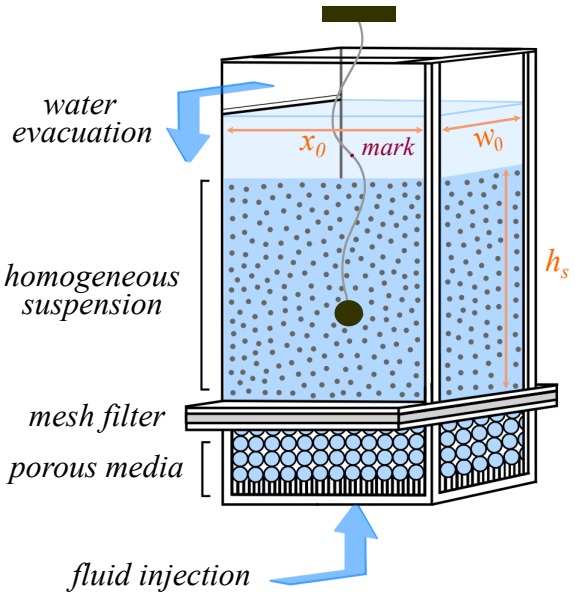

Figure 1.14

Device devoted to the investigation of the fall of a macroscopic sphere into the suspension.

velocities of the sphere U_s, determined under the assumption that the sphere experiences a phase of constant acceleration followed by a phase of constant velocity, are observed to similarly decrease with $\frac{\Phi_s}{\Phi_{pack}}$, when both the density and effective viscosity of the mixture increase (Figure 1.15a). The dimensional analysis reveals the introduction of an additional non-dimensional group to describe the system, which compares the mean diameter of the particles that compose the suspension to that of the sinking sphere $\frac{d_p}{D}$. Plotting U_s as a function of the velocity of the sphere U_{S0} falling into the equivalent fluid of density ρ_m and effective viscosity μ_m (determined from (1.24)), such as $U_{S0} = \frac{(\rho_D - \rho_m)gD^2}{18\mu_m}$ multiplied by $\alpha\frac{d_p}{D}$, where α is a constant roughly equals to $\sqrt{3}$ for the different materials (Figure 1.15b), exposes that the terminal velocity of the sphere U_s expresses as :

$$U_s = \alpha U_{S0}\frac{d_p}{D}, \tag{1.25}$$

The non-dimensionnal velocity $U_s^* = \frac{U_s}{\alpha U_{S0}\frac{d_p}{D}}$ is also exposed in insert of Figure 1.15b and approximately amounts to unity in all experiments. This expression (1.25) comes

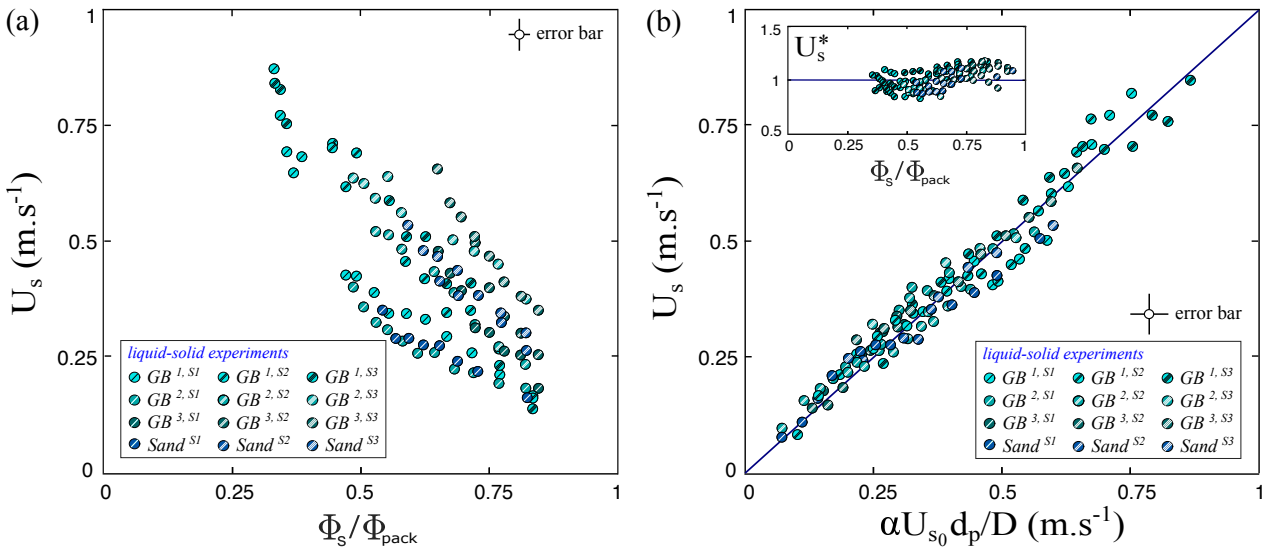

Figure 1.15

(a) Terminal velocity of the sinking sphere U_s as a function of $\frac{\Phi_s}{\Phi_{pack}}$. (b) U_s as a function of $\alpha U_{S0}\frac{d_p}{D}$, where the ratio $U_s^* = \frac{U_s}{\alpha U_{S0}\frac{d_p}{D}}$ as a function of $\frac{\Phi_s}{\Phi_{pack}}$ is exposed in insert.

down to rewriting the drag force F_D as :

$$F_D = 3\pi D\mu_m U_{S0}, \tag{1.26}$$

$$F_D = \tfrac{3\pi}{\alpha} D\mu_m U_s \tfrac{D}{d_p}, \tag{1.27}$$

The mean shear rate applied to the surface of the sphere $\tau_w = \frac{F_D}{\pi D^2}$ is thus expressed as :

$$\tau_w = \frac{3}{\alpha}\mu_m \frac{U_s}{d_p}. \tag{1.28}$$

which means that τ_w is proportional to μ_m and independent of D. One possible interpretation may suggest that the viscous dissipation acting on the falling sphere develops over a thin, highly sheared mixture layer of thickness d_p and effective viscosity μ_m, trapped between the surface of the sphere and the nearest particle. Beyond this layer, the particles of the suspension slide relatively to the sphere [Amin *et al.* (2022)].

1.7 Boundary of the homogeneous regime

The non-dimensional group St_0 turns out to also control the minimum value of the concentration $\frac{\Phi_{low}}{\Phi_{pack}}$ below which the bed becomes unstable, separating the homogeneous fluidization regime from the heterogeneous agitated one (Figure 1.16). This means that, the heavier or larger the particles, the greater their inertia, the more they are agitated and the less the homogeneous state is stable. Otherwise, the finer and lighter they are,

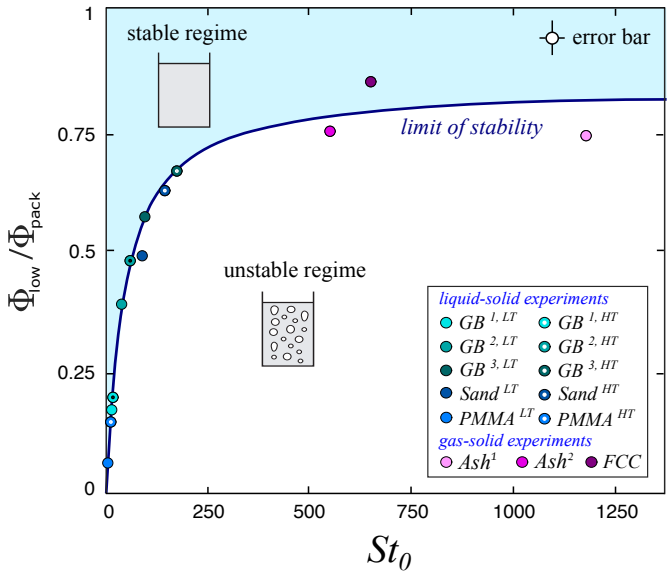

Figure 1.16

Maximum bed expansion $\frac{\Phi_{low}}{\Phi_{pack}}$ above which the mixture becomes unstable as a function of $\mathcal{S}t_0$.

the less inertia they have, the less they are agitated, and the more they can be expanded, while remaining in a homogeneous state. This explains in particular why the expansion of gas-solid systems, characterized by a high St_0 and a high density ratio $\frac{\rho_s+1/2\rho_f}{\rho_f}$ (Table 1.1), is much lower than that of liquid-solid systems, characterized by a low St_0 and a quite lower density ratio.

By modifying the boundary conditions, in particular the fluid injection at the base of the suspension, we can move this limit such as heterogeneities may appear earlier in the mixture, which allows us to study the transition towards the unstable regime and in

particular to observe the particle agitation through the bed surface oscillations, which constitutes a part of the PhD work of Loïc Rousseau that I co-supervise with Frédéric Risso (DR. CNRS, IMFT, Toulouse), under the direction of Pr. Mohammed Boussafir (PrU., GéHCO, Tours). In this new configuration, we first investigated the fluidization and sedimentation velocities in liquid-solid suspensions similarly composed of PMMA$-W$, $GB^1 - W$, $GB^3 - W$ (see Table 1.1) for different particle concentrations $\frac{\Phi_s}{\Phi_{pack}}$ (Figure 1.17a). The mean velocities U_f and U_{sed} are observed to be similar in suspensions made with PMMA$-W$, while U_f is greater than U_{sed} in suspensions composed of $GB^3 - W$, or experiences a transition with $GB^1 - W$ for which $U_f = U_{sed}$ when $\frac{\Phi_s}{\Phi_{pack}} > 0.6$ or $U_f > U_{sed}$ when $\frac{\Phi_s}{\Phi_{pack}} \leq 0.6$ (Figure 1.17a). We then explored oscillations of the bed surface to

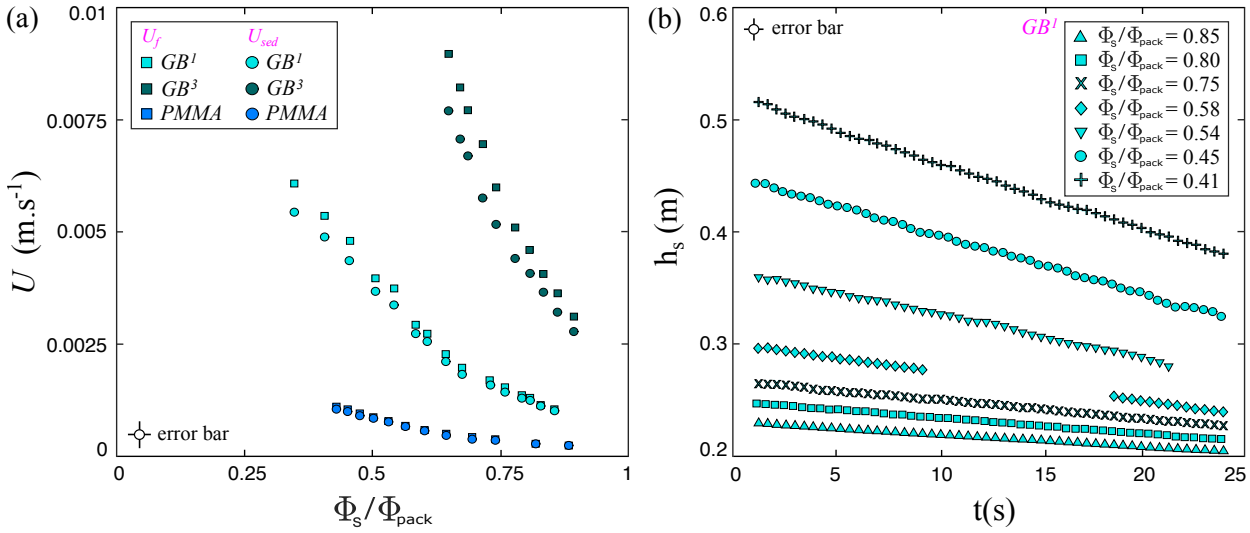

Figure 1.17

(a) Fluidization and sedimentation velocities, termed U, represented as a function of $\frac{\Phi_s}{\Phi_{pack}}$ for liquid-solid suspensions made with PMMA, GB^1, and GB^3 in the new configuration. (b) Evolution of the bed thickness h_s with time t during the sedimentation process of $GB^1 - W$ for different concentrations.

better understand this transition. In aid of a high-speed video camera, we observe that the suspension surface oscillates over time during both the fluidization and sedimentation

processes (Figure 1.17b). At high concentrations ($\frac{\Phi_s}{\Phi_{pack}} > 0.6$), the bed is observed to move vertically and uniformly, corresponding to vertical plane waves characterized by high-frequency oscillations (0.35 Hz) of low-amplitude (from -0.5mm to $+0.5$mm). At low concentrations (when $\frac{\Phi_s}{\Phi_{pack}} \leq 0.6$), the bed becomes agitated so that low-frequency oscillations (0.125 Hz) of higher amplitude (from -2mm to $+2$mm) become laterally desynchronized, indicating the formation of non planar waves.

Using the first-order equation of propagation of a concentration wave in a fluidized bed developed by Batchelor (1988), we calculated the celerity c of the kinematic planar waves that travel across the suspension to infer their wavelength $\lambda = \frac{f}{c}$ from the measured frequency f, which is observed to increase as $\frac{\Phi_s}{\Phi_{pack}}$ decreases and to diverge as $\frac{\Phi_s}{\Phi_{pack}} < 0.6$ (Figure 1.18). λ can be interpreted as a correlation length which corresponds to the size of heterogeneities and thus highlights that the bed can be considered as heterogeneous as $\frac{\Phi_s}{\Phi_{pack}} < 0.6$, *i.e.* when U_f deviates from U_{sed}, while becoming unstable when the size of heterogeneities may become of the order of that of the reservoir. These results turn out to be in good agreement with those of the literature (Figure 1.18), in particular with experiments of Ham *et al.* (1990) who observed these compression-dilatation waves in concentrated liquid-solid suspensions made with particles of mean diameter $d_p = 325\mu m$ and observed a divergence of λ close to the packing state which may correspond to the transition towards jamming in which particles are in contact with each other [Rousseau *et al.* (2025)].

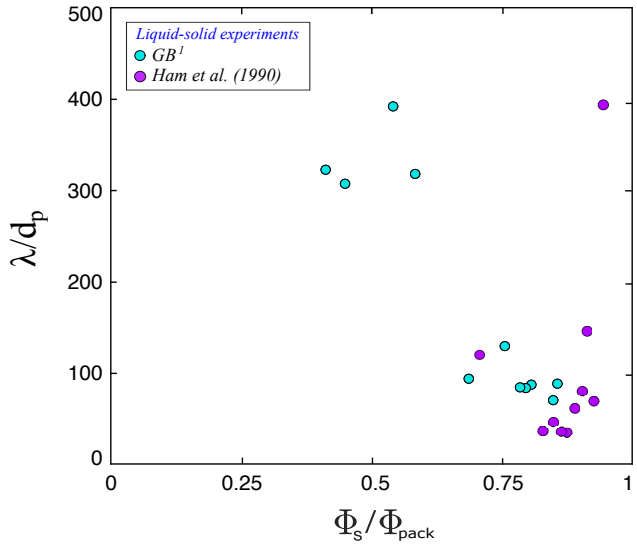

Figure 1.18

Wavelength λ of the concentration waves developed in suspensions made with $GB^1 - W$, normalized by the particle diameter d_p, as a function of $\frac{\Phi_s}{\Phi_{pack}}$ for the present experiments compared with those of Ham *et al.* (1990).

1.8 Conclusion

The fluidization and sedimentation of concentrated particulate suspensions represent an important, complex problem of physics which is the purpose of a large number of past and recent studies of the literature [Richardson & Zaki (1954); Abrahamsen & Geldart (1980); Kramer *et al.* (2019)]. In this chapter, we have chosen to investigate suspensions of non-cohesive powders, *i.e.* made with fine particles, that sediment in a homogeneous mixture, *i.e.* fully fluidized, obtained between the packing state and the unstable regime, which allows us to describe the mixture as an equivalent fluid characterized by the density and effective viscosity of the suspension. The dimensional analysis shows that the description of the problem must be based on four non-dimensional groups : ϕ_s, ϕ_s/ϕ_{pack}, $\mathcal{R}e$, $\mathcal{S}t$. When the Reynolds number is weak ($\mathcal{R}e < 1$), which is the case for the sedimentation processes developed in natural suspensions (basal pyroclastic flows, lahars) and in our experiments,

the problem solely depends on ϕ_s, ϕ_s/ϕ_{pack}, and $\mathcal{S}t$. By conducting experiments involving different types of materials and fluids, we varied these non-dimensional groups over a wide range of values in order to obtain the most universal fluidization/sedimentation law as possible, involving these parameters through three independent functions. In particular, we highlighted that, even though the inertia of the fluid is negligible in this context, that of the particles plays a major role which must be taken into account in the description of the fall velocity through a relevant Stokes number $\mathcal{S}t_0$ which solely depends on the fluid and grains properties. In this way, we are able to gather all the experimental data obtained with gas-solid and liquid-solid suspensions. The results analysis indicates that this law can be obtained from the theoretical velocity of an isolated particle settling in a pure, infinite fluid at rest to which we must apply a correction in density and viscosity, which amounts at describing the particle motion into an equivalent fluid with properties similar to those of the suspension. As long as the mixture remains homogeneous, we can describe the velocity of a macroscopic sphere (*i.e.* much larger than the particles) falling into the suspension, considering the equivalent fluid and the size ratio between the particles and the sphere. The Stokes number, which characterizes the particle inertia, also controls the limit of stability of the mixture. The more inertia the particles have, the more rapidly the system can destabilize, the less the mixture can expand. To describe this mechanism, we investigated the fluctuations of the bed surface and observed that the bed moves uniformly, through a bulk motion, at high concentration, while starting sloshing at low concentration, due to the propagation of concentration waves traveling from the base to the surface. Their wavelength increases with the mixture dilatation, so that the system becomes heterogeneous for large values of λ and can be considered as unstable when the typical size of heterogeneities reaches that of the reservoir.

Chapitre 2

Dynamics of short-lived sedimenting suspensions

This chapter concerns the following works :

• Physical modeling of the dam-break flow of sedimenting suspensions (2020) by L. Girolami & F. Risso, *Physical Review Fluids*, 5, 084306, doi :10.1103/PhysRevFluids.5.084306.

• Sedimentation of short-lived fluid-solid suspensions (2024) by L. Girolami, F. Risso, A. Amin, L. Rousseau, A. Bondesan, S. Bonelli, *Physics of Fluids*, 36, 113308.

• A three-layer model for particulate suspension flows driven by sedimentation (2025) by A. Bondesan, L. Girolami, F. James, L. Rousseau, *PoF*, 37, doi :10.1063/5.0261889.

• Dynamics and sedimentation of laboratory ash flows (2008) by L. Girolami, *PHD Thesis*, Université Blaise Pascal.

• Dynamics and sedimentation of liquid-solid suspensions (2022) by A. Amin, *PHD Thesis*, Université de Tours, tel-04589465.

Abstract

After having described in detail the properties of static suspensions generated in the reservoir, we now explore the transport and sedimentation of gas-solid and liquid-solid mixtures once released down a horizontal and impermeable flume. During propagation, the homogeneous mixture progressively defluidizes and sediments by developing an internal flow structure with overlying layers. They can be described as low-viscosity quasi-parallel flows which move and loose mass at constant velocity, then leaving a deposit of constant slope. In this study, we highlight that the particle aggradation velocity, that can be predicted from the mean flow velocity and the deposit slope, turns out to be roughly similar to that measured from static suspensions of same concentration, provided that the mixture agitation does not disturb the deposition. Numerical simulations highlight that kinematic and deposit profiles can be satisfyingly reproduced with a simple description.

Keywords : Geophysical mass flows, dam-break experiments, sedimenting suspensions, runouts prediction, kinematics, deposit morphology, physical modeling, scaling laws, numerical simulations, shallow-water description.

2.1 Introduction

The fluidization of non-cohesive powders can drive to the formation of dense homogeneous suspensions that deflate and settle progressively once the fluid supply is exhausted. Their ability to travel large distances down gentle slopes, mostly observed during the final course of some catastrophic events when the flow runout is controlled by sedimentation, is mainly attributed to the reduction of interparticle friction. Such fluidized mixtures represent thereby one of the most important hazards encountered in natural sciences [Rampino & Self (1992); Thouret *et al.* (2020); Girolami & Risso (2020)]. They are therefore difficult to observe [Hoblitt (1986); Levine & Kieffer (1991); Loughlin *et al.* (2002)], so that their description has become a major issue guided by the need of predicting their

runouts and deposits shape, which are usually carefully studied in the field to infer the flow dynamics [Sparks (1976); Druitt & Kokelaar (2002); Branney & Kokelaar (2002); Vallance & Iverson (2015); Thouret *et al.* (2020)]. An important purpose lies in completing such field analyses and resulting conceptual models with laboratory experiments that can serve as a guide to identify the key parameters which control their emplacement as well as to describe in detail the processes involved in the flows [Lajeunesse *et al.* (2005); Lube *et al.* (2005); Girolami *et al.* (2008)]. The determination of relevant scaling laws lies in the description of the two phases separation, as the mixture progressively stratifies to form overlying layers of contrasted concentrations, before running out of mass when all particles have settled and that fluid is mostly expelled from the deposit. Many studies of the literature first distinguished the dense or dilute regime in which the dynamics is principally dominated by particle interactions or the fluid turbulence [Denlinger & Iverson (2001); Esposti Ongaro *et al.* (2011)]. More recent scientific efforts were devoted to the development of multi-layer approaches, based on shallow-water equations, to explore the internal stratification or detachment processes [Doyle *et al.* (2008); Shimizu *et al.* (2019, 2021); Pudasaini (2012)]. However, none of these models have proposed a satisfying formulation of the sink terms in the conservation equations, while introducing an artificial solid friction to force the flow to stop over a reasonable time or length. Therefore, no preliminary studies have proposed yet a universal description of sedimenting suspensions able to predict the shape of their deposits. This chapter is devoted to the investigation of particle-laden flows composed of non-cohesive powders as micrometer volcanic ash suspended into a hot gas [Freundt (2003)] or micrometer fluvial sediments suspended into a moderately hot water [Pierson *et al.* (1996)] to describe the emplacement dynamics of basal pyroclastic flows and lahars. In particular, we investigate cases where the solid concentration does not approach too much the packing state dominated by the excess of pore pressure [Roche (2012); Dufek (2016); Valentine (2020)] or the dilute regime dominated by vorticity [Andrews & Manga (2012); Ongaro *et al.* (2016); Brosch & Lube (2020)]. In doing so, the fully-fluidized concentrated mixture can be described as an equivalent

fluid in which particles and fluid move at large speed through a general motion, while powders progressively settle throughout the suspension at low velocity, in the Stokes flow regime, without being disturbed by the flow [Girolami & Risso (2020)]. This allows us to incorporate the detailed description of settling processes into that of the flow in order to numerically predict the dam-break flow experiments [Girolami *et al.* (2024); Bondesan *et al.* (2025)]. As the sedimentation was explored in static suspensions, we can reasonably wonder whether the law, presented in the previous chapter, is relevant to describe the behavior of the flowing suspensions. This study first presents observations and quantitative measurements of the flows made with different particles and fluids, bringing together experimental data acquired during the PhD of Ahmad Amin and those acquired during my PhD, then develops a multi-layer approach based on a physical analysis to infer the flow kinematics and deposits geometry through a simple description, which is ultimately confronted to experiments.

2.2 Dam-break flow configurations

After having carefully prepared the suspension into the reservoir by fixing the dilatation rate to control the mixture solid concentration $\frac{\Phi_s}{\Phi_{pack}}$ and density ρ_m, the reproduction of dam-break suspension flows requires some technical constraints specific to each system : gas-solid and liquid-solid mixures. For liquid-solid suspensions, the reservoir $-$of length $x_0 = 0.10m$ and width $w_0 = 0.30m-$ is endowed with a spillway located at the rear to instantaneously expel the column of water formed at the surface of the suspension during fluidization and ensure the release of a free-surface column down the smooth, horizontal and impermeable flume. This set-up thus imposes to fix the suspension thickness $h_s = 0.27m$ before release in each experiment. The dilatation rate is then varied from one experiment to another by decreasing the particle height h_p from $0.27m$ to $0.19m$, allowing a study range of $\frac{\Phi_s}{\Phi_{pack}}$ from 0.95 to 0.70. In all experiments, the operation temperature, which can slightly modify the mixture viscosity, is fixed at 25^oC. For gas-solid

suspensions, the reservoir −of length $x_0 = 0.3m$ and width $w_0 = 0.15m$− does not require neither spillway nor conducting experiments through a closed-loop system since the gas instantaneously escapes into the room. Since the flows last less than $2s$, only the reservoir is brought up to temperature of around 180^oC with heating tapes. The set-up is however entirely designed in aluminum since the suspension spreads at the same temperature, while a transparent side wall in pyrex allows the flow visualization. In a first series of experiments, the suspension thickness h_s is fixed at $0.25m$, while the particle height h_p varied from $0.25m$ to $0.16m$, as in liquid-solid suspensions. In a second series of experiments, h_s varies from $0.16m$ and $0.25m$, while h_p remains fixed at $0.16m$, allowing a study range of $\frac{\Phi_s}{\Phi_{pack}}$ from 0.65 to 0.95. In both configurations, the channel length was fixed at $3m$ to ensure the reproduction of relatively thick, elongated flows.

2.3 Presentation of experiments

When released, the suspension spreads down the flume at a velocity of around $2m.s^{-1}$. During propagation, the homogeneous mixture progressively defluidizes and sediments by developing overlying layers : a basal deposit that thickens progressively during travel ; a flowing homogeneous suspension that thins progressively by loosing particles downwards and fluid upwards ; an upper pure fluid layer for the case of liquid-solid suspensions that moves at the surface of the suspension. As commonly observed in classical dam-break flows, the time evolution of the flow front exposes three phases : a brief gravitational collapse ; a dominant phase of constant velocity where both deposition and fluid expel occur ; a short decelerating phase [Girolami *et al.* (2008); Bondesan *et al.* (2025)]. During the dominant phase of transport, the suspension layer follows a global motion in which the two phases move at the same velocity (Figure 2.1), which allows us to describe the suspension features as those of an equivalent fluid, while particles progressively settle throughout the suspension, at low speed (in the Stokes flow regime), without being disturbed by the flow [Girolami *et al.* (2008); Girolami & Risso (2020)]. This allows us to integrate the work

of Amin *et al.* (2021), through the law defined in (1.18), to describe the sedimentation processes.

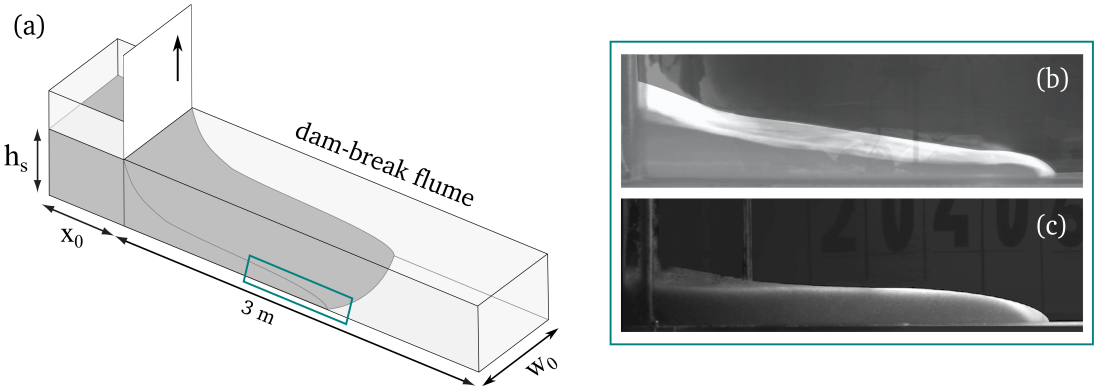

Figure 2.1

(a) Scheme of the dam-break suspension flows made with gas-solid and liquid-solid systems. Picture of the frontal region of (b) a gas-solid suspension ; (c) a liquid-solid suspension.

Despite their expected complexity, dam-break suspension flows are observed to expose a simple and systematic behavior with the solid concentration, whose runouts are mainly controlled by sedimentation [Girolami *et al.* (2024)]. The general description first requires simple measurements of the traveled distance L_∞, runout duration T_∞, mean and frontal velocities U and $U_\mathcal{F}$, deposit height h_d that reaches its maximum value h_{d_∞} at the lock gate, and deposit slope S. The flow runouts (duration and traveled distance), measured in both gas-solid and liquid-solid experiments, were first observed to be of the same order of magnitude in the two different systems (Figure 2.2), while slightly greater in liquid-solid suspensions where the settling velocity develops more slowly. Both the runout duration T_∞, the traveled distance L_∞, and the frontal velocity $U_\mathcal{F}$ measured during the dominant phase of transport and scaling with $U_\mathcal{F} \propto \sqrt{\left(\frac{\rho_s - \rho_f}{\rho_s}\right) 2gh_s}$, decrease with increasing particle concentration $\frac{\Phi_s}{\Phi_{pack}}$ (Figure 2.2).

At the end of the flow, particles come at rest and form a deposit, overlaid by a fluid layer in the case of liquid-solid suspensions. The deposits shape depends on the solid concentration. The more concentrated the suspensions, the less they flow, the thicker the

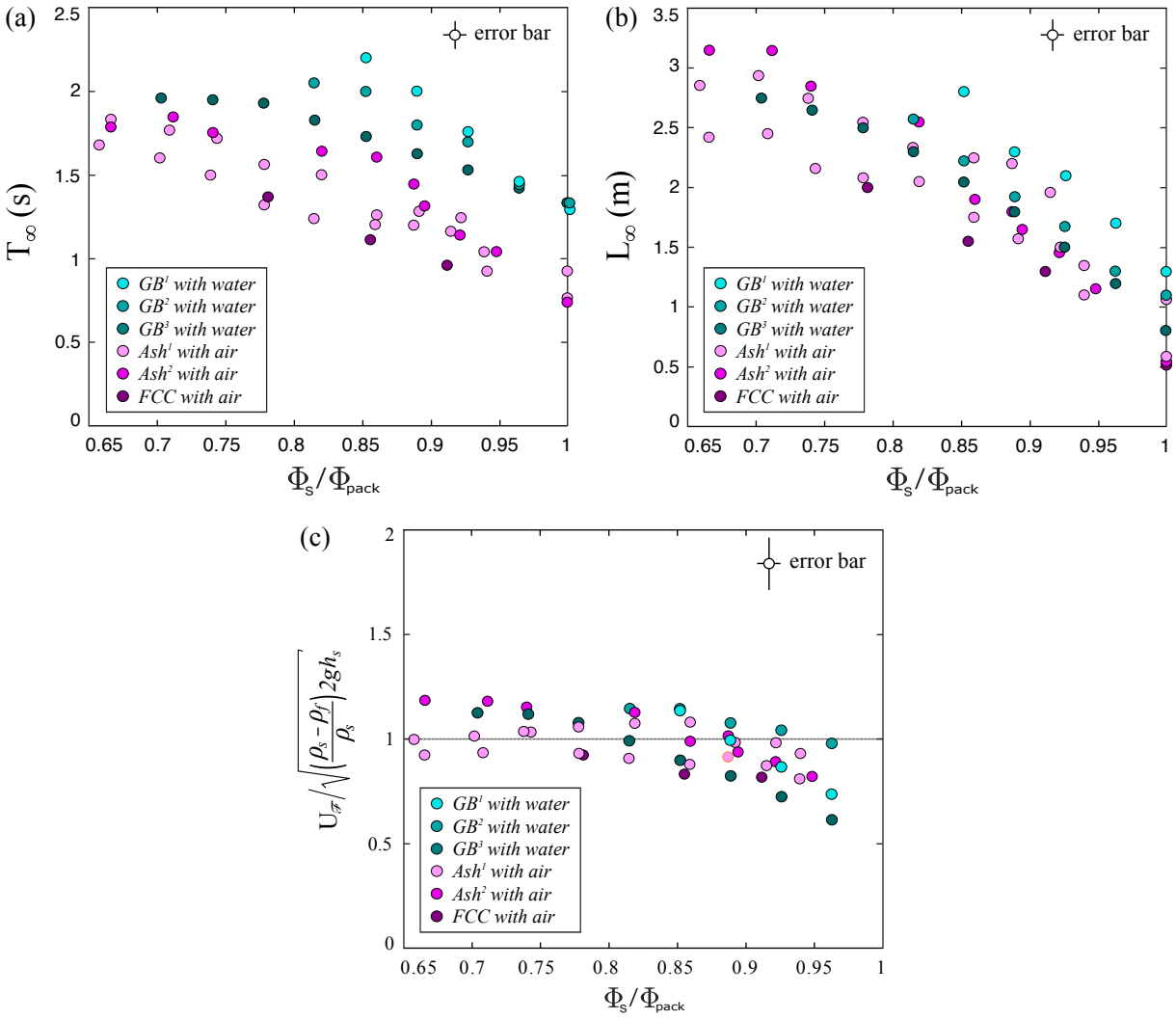

Figure 2.2

(a) Flow duration T_∞ ; (b) traveled distance L_∞ ; (c) frontal velocity $U_\mathcal{F}$ normalized by $\sqrt{\left(\frac{\rho_s-\rho_f}{\rho_s}\right)2gh_s}$ as a function of the particle concentration $\frac{\Phi_s}{\Phi_{pack}}$.

deposits and the sharper the slope. The velocity at which the basal deposit thickens, termed U_{agg}, is observed to be constant in time and space [Girolami *et al.* (2010, 2024)], *i.e.* during the flow that spreads at constant velocity, thus forming a deposit of constant slope S [Girolami & Risso (2020)]. This implies that simple measurements of the deposit slope S and frontal velocity $U_{\mathcal{F}}$ are sufficient to infer the aggradation velocity U_{agg} from flowing suspensions, since $h_d(x,t) = \int_{T_0=\frac{(x-x_c)}{U_{\mathcal{F}}}}^{T_\infty} U_{agg} dt = U_{agg}\left[T_\infty - \frac{(x-x_c)}{U_{\mathcal{F}}}\right]$, the deposit slope is given by $S = \frac{\partial h_d(x,t)}{\partial x} = -\frac{U_{agg}}{U_{\mathcal{F}}}$.

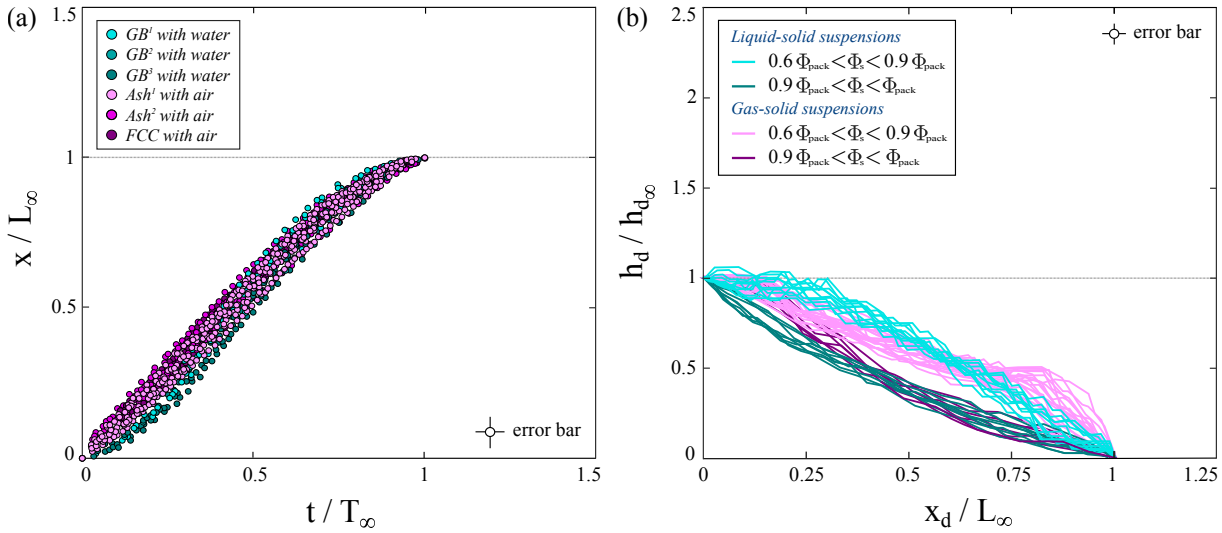

Figure 2.3

(a) Frontal position x normalized by the runout distance L_∞ as a function of time t normalized by the runout duration T_∞. (b) Deposit height h_d normalized by the runout thickness at the lock gate h_{d_∞} as a function of the deposit length x_d normalized by the runout distance L_∞.

The flow kinematics, explored through the evolution of the flow front position x, normalized by the final distance L_∞, with time t, normalized by the total duration T_∞, highlights a similar behavior in the two different systems, pointing again a similar frontal velocity $U_{\mathcal{F}}$ (Figure 2.3a). The deposit geometry, explored through the evolution of the deposit height h_d normalized by the maximum thickness h_{d_∞} as a function of the deposit length x_d normalized by the runout distance L_∞, allows us to distinguish two types of

profiles (Figure 2.3b). Triangular deposits of constant slope, represented by dark colors in Figure 2.3, are formed by highly concentrated flows ($0.9 \leq \frac{\Phi_s}{\Phi_{pack}} \leq 1$) in which sedimentation is initiated at the beginning of the longest phase of transport, when the flow is being established. Trapezoidal deposits composed of a plateau and a constant slope, represented by light colors in Figure 2.3, are formed from slightly loaded flows ($0.65 \leq \frac{\Phi_s}{\Phi_{pack}} \leq 0.9$) in which sedimentation is initiated after a critical time t_c at a critical length x_c, which may correspond to the phase of gravitational collapse.

The sedimentation processes developed in flowing suspensions were first explored by investigating the evolution of the deposit thickness h_d with the time taken after the passage of the flow $t - t_{\mathcal{F}}$ in aid of a high-speed video camera calibrated at 1200 frames per second in proximal areas ($x = 0.30 - 0.60m$) where h_d is thickest (Figure 2.4a). The measured aggradation velocity V_{agg} is observed to be roughly constant with time (Figure 2.4a) which allows us to infer its mean value from S and $U_{\mathcal{F}}$, while assuming that $U_{\mathcal{F}} = \frac{L_{sed}}{T_{sed}}$ which amounts to neglecting the short, deceleration phase. Comparing then predictions of $U_{agg} = -SU_{\mathcal{F}}$ with measurements of V_{agg} performed in proximal areas of flowing suspensions (*i.e.* over the first 0.60m) taken at different $\frac{\Phi_s}{\Phi_{pack}}$, exposes a satisfying correlation of results gathered along the line $U_{agg} = V_{agg}$ (Figure 2.4b).

Comparing now values of U_{agg} with those of U_{agg_0} measured in static suspensions, as a function of the mixture concentration $\frac{\Phi_s}{\Phi_{pack}}$, exposes a roughly constant ratio, close to unity, in all suspensions involving small and light particles (*i.e.* $d_p \leq 300\mu m$, $\rho_s \leq 2500kg.m^{-3}$; Figure 2.5a). Otherwise, for suspensions involving large and dense particles with water, U_{agg} becomes significantly reduced compared to its reference value U_{agg_0}, which may be explained by the mixture agitation during propagation. Plotting this ratio $\frac{U_{agg_0}}{U_{agg}}$ with the Reynolds number, based on the particle diameter d_p and the mean flow velocity $U = \frac{L_\infty}{T_\infty}$, highlights a threshold Reynolds number ($Re \geq 250$), above which the particle aggradation velocity U_{agg} is affected by the mixture agitation and can not be predicted by U_{agg_0} (1.22) (Figure 2.5b). This result means that, as long as $Re \leq 250$, particles settle vertically throughout the flowing suspension without being significantly

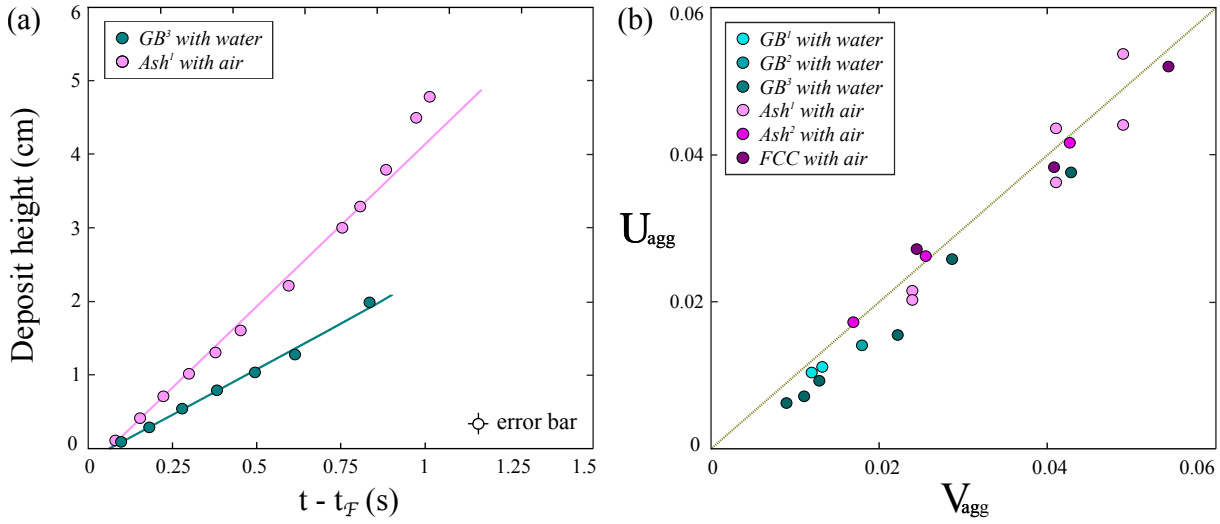

Figure 2.4

(a) Evolution of the deposit height h_d with time taken after the passage of the flow front $t-t_{\mathcal{F}}$ for a gas-solid and a liquid-solid suspension taken at $\frac{\Phi_s}{\Phi_{pack}} = 0.855$. (b) Prediction of $U_{agg} = -SU_{\mathcal{F}}$ against measurements of V_{agg} in flowing suspensions performed at different concentrations $\frac{\Phi_s}{\Phi_{pack}}$.

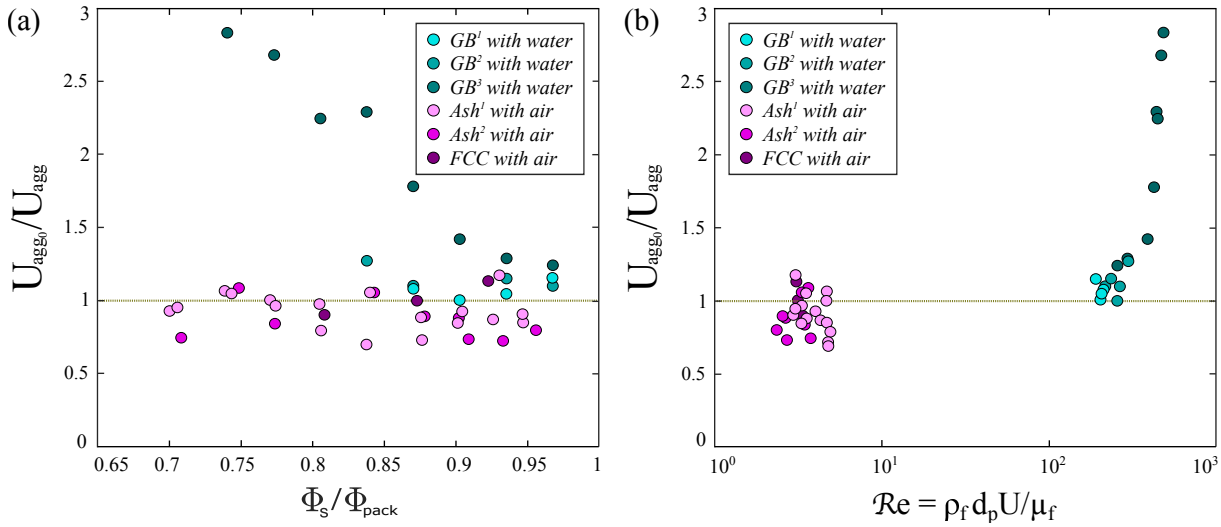

Figure 2.5

(a) $\frac{U_{agg_0}}{U_{agg}}$ as a function of $\frac{\Phi_s}{\Phi_{pack}}$. (b) $\frac{U_{agg_0}}{U_{agg}}$ as a function of the Reynolds number Re which compares the fluid inertia to the viscous stress at the scale of the particle.

affected by the mixture agitation, so that the flow can be described as a low-viscosity quasi-parallel flow, with no vertical velocity fluctuations capable of altering the particles motion [Girolami & Risso (2020); Girolami *et al.* (2024)]. In this case, the description of the sedimentation processes can be decoupled from that of the flow and be based on the detailed study made in static suspensions. Above the threshold value of Re, the fluid inertia becomes important enough to develop fluctuating eddies, at the scale of the particle, which may significantly disturb and delay their sedimentation. In that case, the deposition processes can not be decoupled from the global flow. A detailed study is required to understand how the mean velocity gradient and fluctuations can impact U_{sed} and U_{agg_0}.

2.4 A simplified description

The detailed observation of experiments allows us to draw up some assumptions that will constitute the base of a physical model able to describe and predict the general flow behavior and the shape of the resulting deposits [Girolami & Risso (2020)]. The three main assumptions are listed as follows,

A_1- As soon as the suspension is released down the flume, the homogeneous mixture defluidizes by progressively separating the two different phases through overlying layers :
· a homogeneous deposit, of concentration Φ_{pack}, that thickens at constant speed U_{agg} ;
· a homogeneous suspension flow, of concentration Φ_s, that thins at constant speed U_{sed} ;
· a homogeneous fluid layer, that thickens or dissipates at constant speed $U_f = U_{sed}$.

A_2- At the beginning of the dominant phase of transport, the flow is being established such as the suspension behaves as a plug flow with a flat velocity profile and settles over a distance $L_{sed} = L_\infty - x_c$ and a period $T_{sed} = T_\infty - \frac{x_c}{U_\mathcal{F}}$, in the Stokes flow regime, without being disturbed by the flow.

A_3- After the gravitational collapse, the frontal region travels at constant speed $U_\mathcal{F} \propto \sqrt{\left(\frac{\rho_s - \rho_f}{\rho_s}\right) 2gh_s}$.

Assumptions A_2 and A_3 allows us to define the deposit slope S, as :

$$S = -\frac{U_{agg}}{U_{\mathcal{F}}}. \tag{2.1}$$

Assuming that $U_{\mathcal{F}} = \frac{L_{sed}}{T_{sed}}$ allows us to draw an expression for T_{sed}, the sedimentation time and L_{sed}, the sedimentation length, as :

$$T_{sed} = \frac{h_{d_\infty}}{U_{agg}}, \tag{2.2}$$

$$L_{sed} = \frac{h_{d_\infty}}{S}. \tag{2.3}$$

The prediction of each layer thickness $h_d(x,t)$, $h_s(x,t)$, $h_f(x,t)$ and averaged velocity $\bar{u}(x,t)$, $\bar{u_f}(x,t)$ requires the computation of the mass and momentum conservation equations [Bondesan *et al.* (2025)], which was the main objective of the post-doctoral project of Andrea Bondesan that I have co-supervised with François James (PrU., Institut Denis Poisson, Orléans). When fully established, the suspension behaves as a thin, elongated, horizontal flow which can be described through shallow-water approximations. As the two phases are separating during transport, the mixture becomes vertically stratified, forming three overlying layers for the most complex case of liquid-solid suspensions delimited by three dynamic interfaces (Figure 2.6). The first one allows to distinguish the static deposit

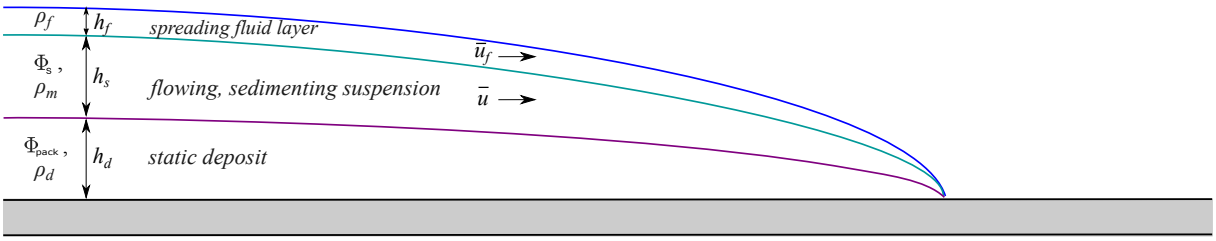

Figure 2.6

Vertical stratification due to sedimentation leading to the formation of three overlying layers for the case of liquid-solid suspensions.

of height h_d and density $\rho_d = \phi_{pack}\rho_s + (1 - \phi_{pack})\rho_f$ from the flowing suspension ; the second one allows us to distinguish the sedimenting suspension of height h_s and density

$\rho_m = \phi_s\rho_s + (1-\phi_s)\rho_f$ from the spreading fluid layer ; and the third one allows us to distinguish the pure fluid layer of height h_f and density ρ_f from the environment, in liquid-solid suspensions (Figure 2.6). By properly defining the mass transfer between the three layers, through assumptions A_1 to A_3, and using a non-penetration condition between the suspension and the surrounding layers, the mass conservation equation allows to predict the kinematics of each interface. By defining the momentum transfer within the two upper spreading layers, through long-wave assumptions taking $\varepsilon = \frac{h_s}{L_\infty} \ll 1$ and $\frac{U_\mathcal{F}}{\sqrt{2gh_s}} = \mathcal{O}(1)$, the Saint-Venant equations allow to predict their dynamics under the action of gravity. As T_{sed} is controlled by the time taken by the particles to settle, the sink terms of the momentum conservation equation for the suspension (2.6) describe the momentum loss due to sedimentation and the gravity work induced by the deposit geometry.

· The mass conservation of the static deposit is given by :

$$\frac{\partial h_d}{\partial t} = \left(\frac{\rho_s}{\rho_s - \rho_f}\right) U_{agg}, \tag{2.4}$$

where the second end-member represents the mass flux of particles that deposit.

· The mass and momentum conservation of the flowing suspension are given by :

$$\frac{\partial h_s}{\partial t} + \frac{\partial (h_s \bar{u})}{\partial x} = -\left(\frac{\Phi_{pack}}{\Phi_{pack} - \Phi_s}\right)\left(\frac{\rho_s}{\rho_s - \rho_f}\right) U_{sed}, \tag{2.5}$$

where $\bar{u} = \frac{1}{h_s}\int_{h_d}^{h_f} u dz$ represents the suspension velocity averaged over its thickness $h_s(x,t)$. The second end-member, given by the product of the settling velocity U_{sed} with the solid volume fraction ratio $\frac{\Phi_{pack}}{\Phi_{pack}-\Phi_s}$ and the density ratio between the two components $\frac{\rho_s}{\rho_s-\rho_f}$, is responsible for the suspension thinning due to the continuous particle deposition.

$$\frac{\partial (h_s \bar{u})}{\partial t} + \frac{\partial (h_s \bar{u}^2)}{\partial x} = -\left[\left(\frac{\Phi_{pack}}{\Phi_{pack} - \Phi_s}\right)\left(\frac{\rho_s}{\rho_s - \rho_f}\right) U_{sed}\right] \bar{u} - g h_s \left(\frac{\partial (h_s + h_d + \frac{\rho_f}{\rho_m} h_f)}{\partial x}\right) \tag{2.6}$$

where the mixture concentration ϕ_s and density ρ_m are supposed to remain constant throughout the flowing layer and equal to ϕ_{pack} and ρ_d within the deposit. The second end-member describes the momentum loss of the moving layer which is mainly due to the

momentum loss of the particles that deposit, passing from a velocity $\bar{u}$ to rest, and by the work of gravity induced by the deposit geometry. The first term may represent a basal friction applied to the flowing suspension.

· The mass and momentum conservation of the pure fluid layer are given by :

$$\frac{\partial h_f}{\partial t} + \frac{\partial (h_f \bar{u_f})}{\partial x} = \left(\frac{\rho_s}{\rho_s - \rho_f} \right) U_f, \tag{2.7}$$

where $\bar{u_f} = \frac{1}{h_f} \int_{h_s}^{h_f} u_f dz$ represents the velocity of the fluid layer averaged over its thickness $h_f(x,t)$.

$$\frac{\partial (h_f \bar{u_f})}{\partial t} + \frac{\partial (h_f \bar{u_f}^2)}{\partial x} = \left[\left(\frac{\rho_s}{\rho_s - \rho_f} \right) U_f \right] \bar{u_f} - g h_f \left(\frac{\partial (h_s + h_d + h_f)}{\partial x} \right). \tag{2.8}$$

where the sink terms represent the momentum lost by defluidization.

2.5 Simulations of sedimenting suspension flows

The coupling of mass and momentum equations is then computed using a finite volume scheme based on a splitting method [Berthon *et al.* (2015)] which allows us to successfully simulate each layer separately, in combination with a HLL-solver to deal with the resulting numerical fluxes. The mass and momentum loss due to sedimentation and defluidization are uniformly implemented over the flow length using an explicit discretization of the velocity. As the slumping phase can not be simply described due to the column aspect ratio $\varepsilon > 1$, which does not respect the shallow-water assumptions, we model a free fall of grains into a moving flow of small aspect ratio $\varepsilon \ll 1$ as relevantly proposed by Larrieu *et al.* (2006). This alternative method allows us to capture the correct frontal velocity $U_{\mathcal{F}}$ at the beginning of the dominant phase of transport. This simplified model is well suited to describe the flow of fully established gas-solid and liquid-solid suspensions subjected to sedimentation. The description of gas-solid suspensions can however be reduced to a two-layer approach, taking $\frac{\rho_s}{\rho_s - \rho_f} = 1$ in equations (2.4) and (2.5) and $\frac{\rho_f}{\rho_m} h_f = 0$ in equation (2.6) [Girolami & Risso (2020)]. A complementary model, including a solid

basal friction κ, introduced in the momentum equation (2.6) at the interface between the suspension and the deposit, was also tested and compared to the frictionless model and experiments. The basal friction κ was chosen proportional to the sedimentation rate, such as $\kappa = -\frac{1}{2}\left(\frac{\Phi_{pack}}{\Phi_{pack}-\Phi_s}\right)\left(\frac{\rho_s}{\rho_s-\rho_f}\right)U_{sed}$, meaning that the mass loss due to sedimentation leads to an enhanced decrease in momentum, inspired from the erosion-induced momentum production observed in natural and experimental landslides [Pudasaini & Krautblatter (2021)]. This term amounts at including a coefficient $\frac{3}{2}$ in the sink term of equation (2.6), as $-\frac{3}{2}\left[\left(\frac{\Phi_{pack}}{\Phi_{pack}-\Phi_s}\right)\left(\frac{\rho_s}{\rho_s-\rho_f}\right)U_{sed}\right]\bar{u}$.

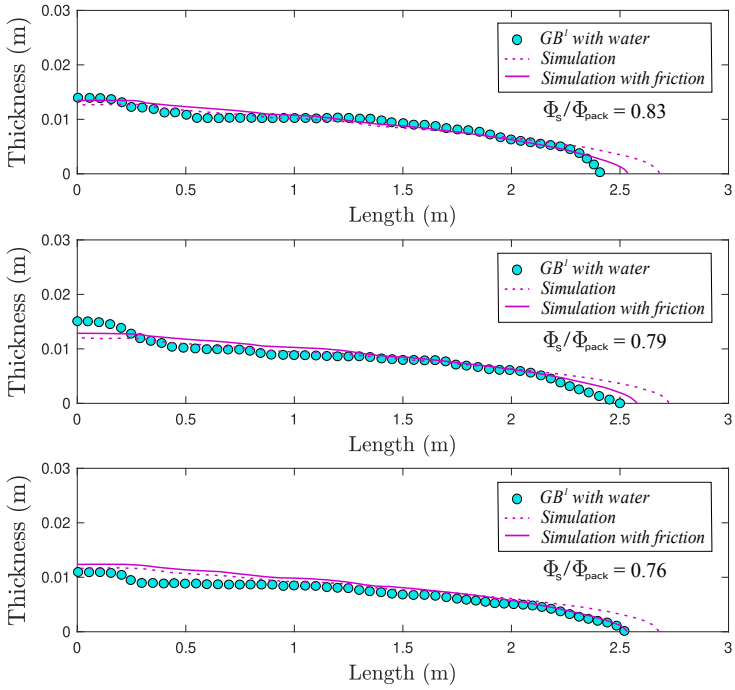

Figure 2.7

Deposits morphology let by the flows of GB^1 and water at the end of experiment, compared with the predictions made by the model including, or not, the additional basal friction.

Figures 2.7 and 2.8 compare the deposit geometry and the kinematic profile of dam-break flow experiments, made with GB^1 and water at three different concentrations ($\frac{\Phi_s}{\Phi_{pack}} = 0.76, 0.79, 0.83$), with analog numerical predictions based on the sedimentation

law (1.18) determined in static suspensions. The deposit shape is observed to be satisfyingly reproduced by the model for the different concentrations, highlighting that the particle settling is not disturbed by the flow, while the introduction of κ allows a reliable prediction of the traveled distance (Figure 2.7). The position of the flow front is also satisfyingly reproduced by the model, while κ, which can be assimilated to a shape factor correction to the velocity profile, equal to $\frac{3}{2}$, tends to capture the correct frontal velocity that is otherwise slightly over-estimated (Figure 2.8).

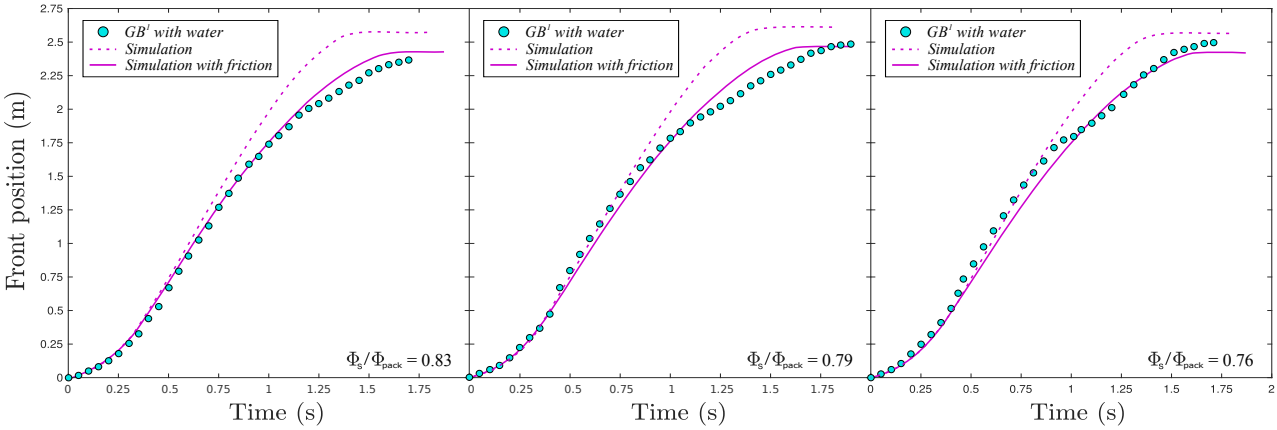

Figure 2.8

Kinematics profiles of the flows of GB^1 and water, compared with the predictions made by the model including, or not, the additional basal friction.

A more detailed investigation, comparing experiments made with GB^3 and water at different concentrations with simulations, was subsequently conducted and highlights that the model is similarly able to predict the deposit morphology (Figure 2.9), especially at moderate concentrations ($\frac{\Phi_s}{\Phi_{pack}} < 0.75$), as well as the traveled distance (Figure 2.10) which is more reliably determined from the kinematic data. The discrepancy observed between the traveled distance L_∞, measured from the final deposit (Figure 2.9), and that determined from the flow front position (Figure 2.10), more pronounced in the most concentrated flows ($0.89 < \frac{\Phi_s}{\Phi_{pack}} < 0.78$), lies in the compaction-induced self-fluidization of the deposit, located at the rear of the reservoir, which gives rise to a small-volume

secondary wave traveling at the surface of the principal flow, such as ultimately increasing its runout duration and traveled distance. This process is not yet described by the model and may explain the systematic under-estimation of L_∞ and frontal thickness h_d in the deposit simulations, especially at high concentrations where the secondary wave seems similarly more concentrated than that developed from the least concentrated flows for which the deposits appear more slightly affected. The flow kinematics is again reliably

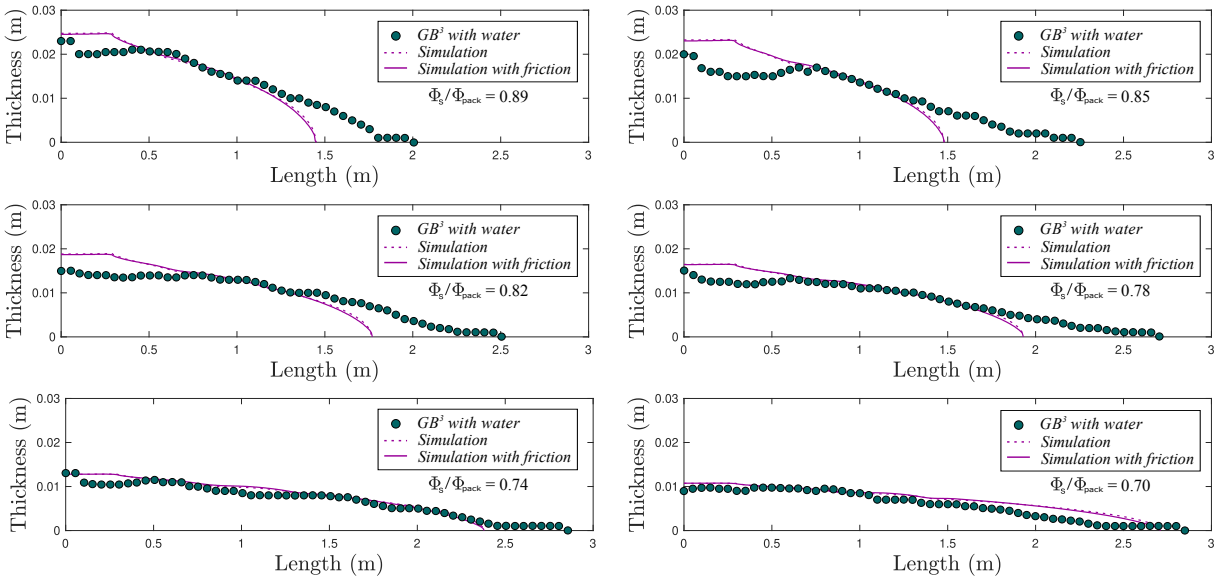

Figure 2.9

Deposits morphology let by the flows of GB^3 and water, compared with the numerical predictions including, or not, the additional basal friction.

predicted by the model (Figure 2.10), provided that the suspension is fully fluidized and does not approach the transitional regime towards the packing state ($\frac{\Phi_s}{\Phi_{pack}} < 0.89$), while κ provides again the correct frontal velocity. As observed in these experiments (GB^3-W), the mixture agitation appears to significantly disturb the particle deposition which can not be described anymore by U_{agg_0} (1.22) [Amin *et al.* (2021); Girolami *et al.* (2024)], thus requiring a correction that depends on the Reynolds number (Figure 2.5b) [Girolami *et al.* (2024); Bondesan *et al.* (2025)].

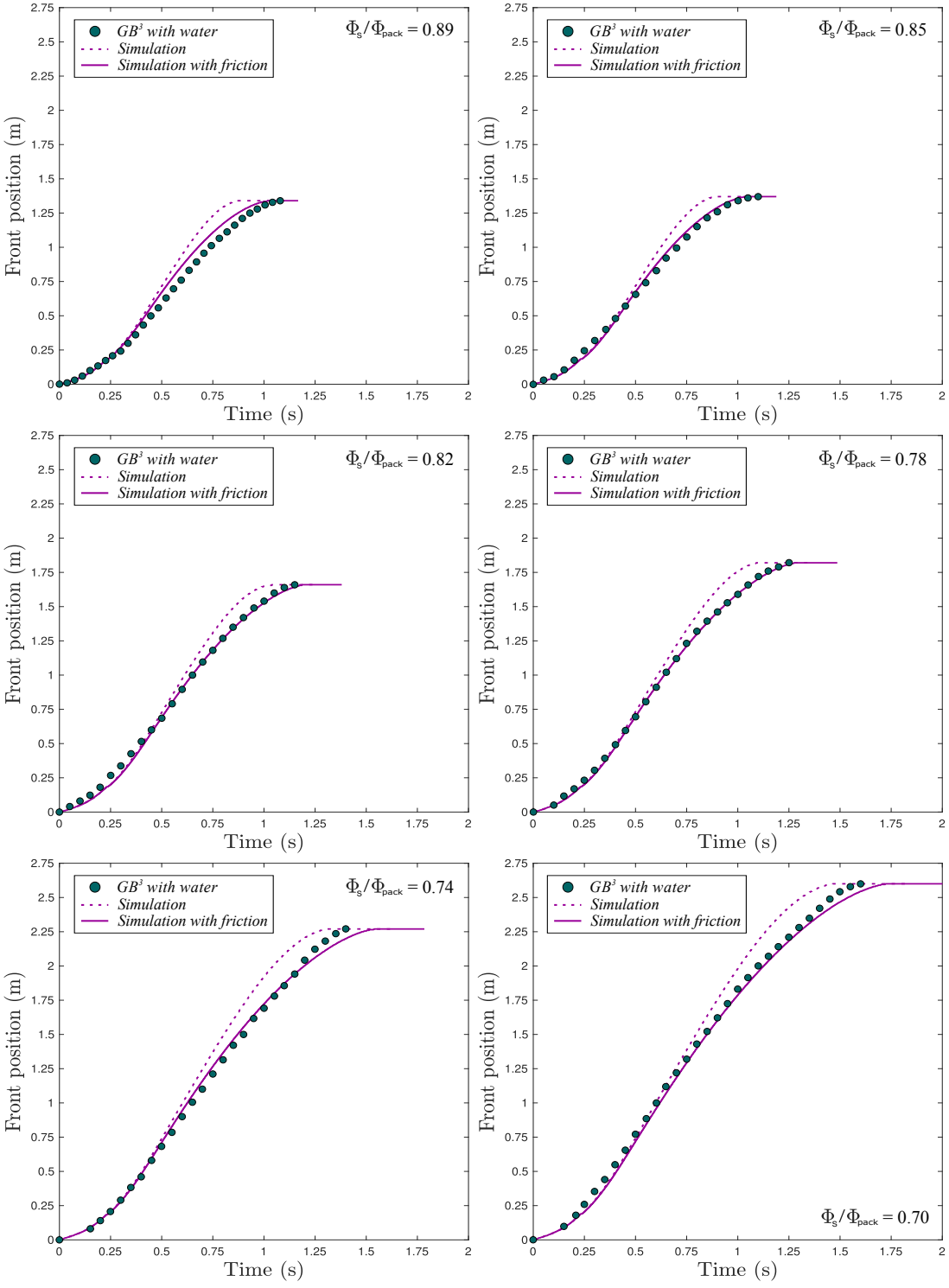

Figure 2.10

Kinematics profiles of the flows of GB^3 and water, compared with the numerical predictions including, or not, the additional basal friction.

The next step of this study will consist in first carefully testing the model with experiments of gas-solid and liquid-solid suspensions made with Ash^{1-2}, FCC, GB^{1-2} and fluids (A and W) taking the reference model of sedimentation [Amin *et al.* (2021)], while slightly modifying the velocity profile, which constitutes a part of the PhD work of Ibrahim Hmamou, that I am co-supervising with Carine Lucas (MC.U, Institut Denis Poisson, Orléans) and Olivier Delestre (MC.U, Laboratoire Jean Alexandre Dieudonné, Nice), in collaboration with Andrea Bondesan (Marie-Curie Fellow at the Department of Mathematical, Physical and Computer Sciences at the University of Parma, Italy) and François James, through a target project entitled "Complex Flows" in the Maths-VivES PEPR framework. It may also be considered to discard from the assumption of a constant concentration Φ_s during the flow, if necessary. In the meantime, this simplified model allows the description of the final stage of particulate suspensions, far from the source, when the established flow, loaded with fine particles and traveling down gentle slopes, is exposed to sedimentation. In cases where the mixture can be approximated as roughly homogeneous, this simplified model is able to provide the sedimentation rate from parameters that can be easily measured on the field or from video footages : the deposit slope S and the flow front velocity $U_{\mathcal{F}}$. Moreover, from the estimation of the solid volume fraction of the natural deposits Φ_{pack}, the model may infer in return the physical properties of natural mixtures, such as the volume expansion $\frac{\Phi_{pack}}{\Phi_s}$ of the mixture and its solid concentration Φ_s during its final phase of transport.

2.6 Conclusion

After having described in detail the properties of static suspensions generated in the reservoir, we have explored the transport and sedimentation of gas-solid and liquid-solid mixtures once released down a horizontal and impermeable flume. The spreading suspension forms a fast-moving, short-lived flow that travels at high Reynolds number and progressively settles in the Stokes flow regime during the dominant phase of transport.

Such experiment can be described as a low-viscosity quasi-parallel flow which moves and looses mass at constant velocity, then leaving a deposit of constant slope. In this study, we highlighted that the particle aggradation velocity can be predicted from the product of the mean flow velocity and the deposit slope and turns out to be roughly similar to that measured in static suspensions of same concentration, provided that the flow Reynolds number, based on the mean flow velocity, the fluid properties and the particles size, remains inferior to a few hundred, so that the mixture agitation can not disturb the sedimentation processes. Preliminary results of numerical simulations exposed that both the kinematics and deposits shape gained with liquid-solid experiments can be satisfyingly captured by the model, provided that the sedimentation velocity includes a correction factor to account for the mixture agitation when necessary. A thorough comparison with relevant experiments of gas-solid and liquid-solid suspensions, characterized by low Reynolds numbers, is then required before considering improving this simplified approach.

Chapitre 3

Soil erosion in the floodplain of a diked river

This chapter concerns the following works :

• On the origin and distribution of internal erosion signatures in the floodplain protected by river dikes (2025) by L. Girolami, S. Bonelli, J.M. Carozza, E. Fogueng-Wafo, J. Burgat, N. Chaouch, R. Valois, *Journal of Flood Risk Management*, doi :10.1111/jfr3.70104.

• Correlation between paleo-environments and dike erosion : impact on the flood risk (2024-2027) by E. Fogueng-Wafo, *on-going PhD of Aix-Marseille University.*

• Internal erosion of sandy gravel and occurrence of open-framework gravels in the subsoil of a river dike (2025) by S. Bonelli, L. Girolami, *Geomechanics for Energy and Environment*, 100690, doi :10.1016/j.gete.2025.100690.

• Large-scale numerical simulations of soil suffusion to map erosion signatures around river dikes (2025) by Z. deng, L. Girolami, N. Benahmed, P. Philippe, S. Bonelli, G. Wang, *Water Resources Research*, submitted.

Abstract

After having explored the sedimentation of powders in particulate suspensions, we now explore their erosion in a saturated porous media after repeated episodes of flood occurred in a diked river. This investigation has been initiated in the framework of a research delegation that I am carrying out at RECOVER (INRAe, Le Tholonet). Geophysical investigations, conducted in areas mainly affected by these processes, reveal the presence of a large paleo-valley filled with fluvial permeable deposits, located beneath the river bed and dikes, which may explain the origin of erosion signatures observed near the dike toes after flooding events. Numerical simulations of fines erosion in the subsoil of the embankment system, induced by underlying seepage flows in different situations, point that their distribution may depend on the valley geometry and its lateral and in-depth position regarding the dike toes. These preliminary results would deserve to be enriched by a spatio-temporal monitoring of the hydromorphodynamic processes in the sedimentary reservoir after repeated episodes of flood gained by the instrumentation of this area.

Keywords : Soil erosion, diked river, paleo-valley, paleo-channels, sedimentary reservoir, geophysical observations, surface signatures, leaks, sand-boils, sinkholes, floodplain, numerical simulations.

3.1 Introduction

On a broader space- and time-scale, particle-laden flows formed at the head of watersheds after an intense erosion of sediments, due to a dam failure or a flash flood, become usually dominated by sedimentation when approaching the coastal area where they travel down gentle slopes and settle to form a deposit that progressively fills the valley and −over millennia− may define a sedimentary basin that may extend from the low-lying deltaic plain to the deep-sea environment. The dimensions of such a sedimentary reservoir depend on the size of the fluvial system, while being usually more expanded at the vicinity

of the delta, where the river is composed of multiple channels. When the river is diked, the flood wave can overflow and submerge the protected plain or −whether the sub-soil is permeable enough− generate underlying seepage flows, traveling from the river to the protected plain, while progressively eroding the saturated soil which may lead afterwards to the appearance of surface signatures, such as leaks, sand-boils and sinkholes down the protected plain [Semmens & Zhou (2019); Marchi *et al.* (2021); Girolami *et al.* (2023)]. Leaks are observed to appear under artesian conditions, near the dike toes, while sand-boils imply the erosion of the sandy substrate to form a conical deposit [Holzer & Clark (1993)]. In this context, sinkholes are mainly attributed to the collapse of underlying decompacted layers due to the erosion of the fine matrice and intend to occur after the peak flooding [Garner & Fannin (2010); Nguyen *et al.* (2014)]. Despite their occurence around many rivers (*i.e.* Mississpi and Ohio rivers, USA [Morton & Olson (2015); Li *et al.* (1996)] ; Po river, Italy [Marchi *et al.* (2021)] ; Waal and IJssel, Netherlands [Semmens & Zhou (2019)]), the occurrence of surface signatures around dikes is not well understood and reliably described in the literature. Most of scientific efforts, mostly devoted to backward erosion piping, are mainly based on a set of conceptual models which allowed the emergence of experiments performed under controlled conditions [Van Beek *et al.* (2011) ; Robbins *et al.* (2015, 2018)] as well as on physical modeling and numerical simulations [Takahashi *et al.* (2017); Liang *et al.* (2017); Robbins & Griffiths (2021); Wewer *et al.* (2021)], but still lack of in-situ observations capable of tracking the spatio-temporal evolution of the different processes involved at different scales, leaving unanswered the question of their origin and distribution that yet becomes a priority [Bonelli (2012, 2013); Girolami *et al.* (2023)]. The main reasons of this gap lie both in the random frequency of flash floods which limits the organization of relevant conventional monitoring systems as those implemented for continuously loaded facilities as dams [Mériaux *et al.* (2012)] and in the focused exploration of the hydraulic facility rather than the fluvial environment, including the fluvial system with water table and protected plains. This chapter aims at proposing imaging of the sub-soil located beneath a diked river and its protected flood

plain to identify the origin of internal erosion signatures and infer scenarii of flooding events to overcome the persistent locks of the literature. Observations are made around Agly river dikes which frequently encounter problems of internal erosion. This site represents a real natural laboratory on which two cases of breach failures have been already recorded in 1999 and 2013 [Van *et al.* (2022); Tourment *et al.* (2018)]. Despite many expert appraisals made on this area [Tourment *et al.* (2018)], these phenomena remain still misunderstood.

3.2 Hazardous erosion signatures along a diked river

Agly is a medium-sized river characterized by a low average flow rate able to increase by more than one order of magnitude during periods of high water levels. The river drains the Northern part of a sedimentary basin that laterally spreads out from the deltaic plain to the Mediteranean Sea. Along this coastal alluvial fan delta, the river is diked since 1970s to protect the proximal population from flooding events. From 1977 to 2020, the embankment system was exposed to 11 floods during which signatures of internal erosion, such as leaks, sand-boils and sinkholes (Figure 3.1a,b,c) repeatedly appear down the floodplain, at the vicinity of the dike toes where hydromorphodynamics phenomena can develop and lead to the formation of decompacted layers. The episode of November, 1999 caused a breach into the Northern bank resulting in 35 victims, while that of March, 2013 caused a breach into the Southern bank which leads to the flooding of the protected plain (Figure 3.1d). Most frequently, the upstream part of the diked area, located from Rivesaltes to Claira (Figure 3.2a), is observed to be significantly affected by the soil erosion during periods of high water levels. The spatial distribution of the signatures observed down the Northern bank after the major flooding event of March, 6^{th} 2013 is reported on Figure 3.2b, where leaks are represented by green circles, sand-boils by blue circles, and sinkholes by red circles. At a first glance, we can observe that all signatures have a bordering position, located at up to around 80 meters from the dike toe, with a specific

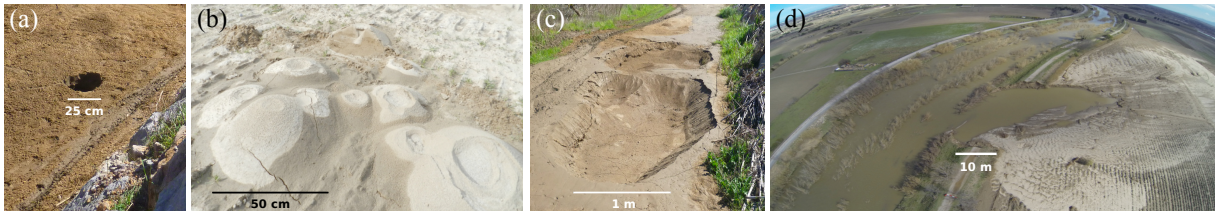

Figure 3.1

Erosion signatures observed at the vicinity of the dike toes after a major flooding event of Agly : (a) leakage ; (b) sand-boils ; (c) sinkholes ; (d) breach-induced flooding (Source : INRAe).

distribution that alternates between leakages, sand-boils, and sinkholes potentially guided by the field morphology and topography. The repeated occurrence of these signatures after each flooding event may suggest the possible presence of superficial, highly permeable materials beneath this area. Location of leaks are evidenced by the presence of small holes of a few tens of centimeters in diameter, while sand-boils let conical-shape deposits of around 20 to 60-cm-wide and 10-cm-height, composed of fine sand, commonly observed after floods at the vicinity of leakholes. Collapse-induced sinkholes may occur after the peak flooding, above decompated layers, and expose an approximately ellipsoidal shape with a flat basement of $\simeq$ 0.5 to 3-m-long (Figure 3.1c).

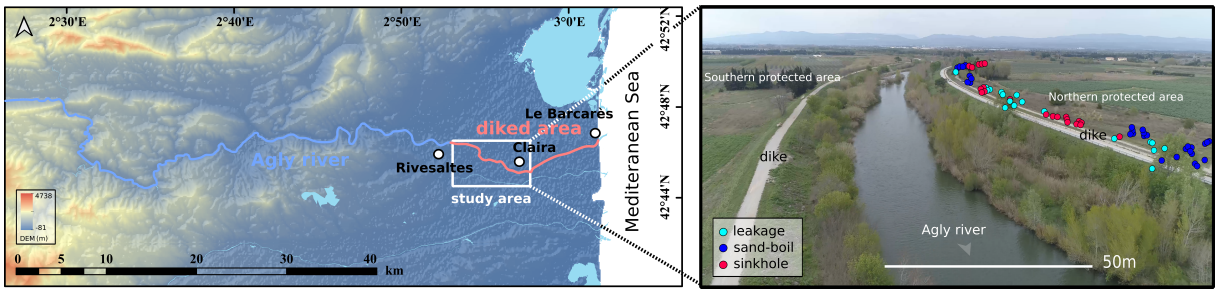

Figure 3.2

(a) Agly river located in the french Pyrénées-Orientales whose diked area is evidenced in red ; (b) Picture of the study area, located in the upstream part of the embankment system, where erosion signatures observed in March, 2013 have been reported in the Northern plain.

Despite the frequent appearance of erosion processes along the river dikes, the scientific community still lacks of an overview of the natural system that would benefit from observations driven at different scales. At large scale (*i.e* at the scale of the embankment system and at the scale of the millenium), historical records, sedimentary boreholes and large-scale field observations may allow to reconstruct the paleo-morphology of the river, including its alluvial deposits and bordered terraces which may contain paleo-channels, down the protected plains which represent areas of preferential erosion. At medium scale (*i.e* at the scale of the dike section and at the scale of the flood), field observations and modeling allow to identify processes of internal hydromorphodynamics in areas mainly affected during floods. At small scale (*i.e* at the scale of the erosion signature and at the scale of the grain erosion), laboratory experiments performed under controlled conditions may allow providing a relevant description of the mechanisms involved and required to develop reliable numerical simulations. The present chapter focuses on large and medium scale analyses of the river morphology and protected plains which turn out to be the first exploring step necessary to get a general overview of the phenomenon, namely to describe the origin and distribution of internal erosion signatures. This investigation represents the project developed during my research delegation at RECOVER (INRAe, Le Tholonet), initiated from September 1st, 2022, in collaboration with Stéphane Bonelli (DR. INRAe, RECOVER, Le Tholonet). Geophysical observations were thus deployed in the study area, known as the most affected during floods. The surface mapping was made in collaboration with Rémi Valois (MC.U, EMMAH, Avignon), using a slingram electromagnetic method EMI (*i.e* a Geonics EM31 equipment), which turns out to be relevant to capture lateral variations of the soil apparent electrical conductivity averaged over the first 6 meters, with a maximum sensitivity at 1.8-m-deep. The survey was made along parallel profiles on a 2.5 x 2.5 m grid. The principle of this method consists in generating a primary magnetic field of known frequency in a transmitter loop which induces electric currents in the soil that generate in turn a secondary magnetic field of identical frequency. The sum of these fields is measured in the receptor loop and allows to deduce the soil conductivity

(in S/m). The cross-section mapping was made in collaboration with DRIM (Geophysical Society, Avignon) using a classical method of electrical tomography ERT (*i.e* a SYSCAL Pro equipment), which turns out to be relevant to map vertical variations of the soil apparent resistivity. The survey was made using a Wenner-Schlumberger configuration along profiles of 475-m-long, transverse to the river bed, including 96 electrodes spaced from 5 meters which allowed us to map vertical sections of 45-m-deep. The principle of this method consists in injecting an electric current of known intensity between two electrodes and to measure the potential drop between two other electrodes in order to deduce the soil apparent resistivity and to calculate its real resistivity through an inversion model. To delineate the in-depth position of interfaces which separate contrasted materials (*i.e* of potentially contrasted permeability), we used a complementary slingram electromagnetic method termed TDEM, in collaboration with Christian Camerlynck (MC.U, METIS Laboratory, Paris). The principle consists in generating a primary decreasing magnetic field with time from an abruptly cut electric current of known intensity passing through a transmitter loop. This magnetic field induces eddy currents in the soil and a secondary magnetic field that creates an electric current whose voltage is measurable in a receptor loop. This voltage directly depends on the soil resistivity and allows us to accurately capture its local value over large depths at a given position. In addition, 10 sedimentary boreholes were sampled near the dike toes (see examples reported on Figure 3.3), in the area of interest, taking a sampling depth ranged from 5 m to 15-m-deep, which allowed us to properly interpret the surface/section maps of conductivity/resistivity from the geophysical measurements, in collaboration with Jean-Michel Carozza (PR.U, LIENSs, La Rochelle).

3.3 Observation of the soil beneath a diked river

The surface mapping of electric conductivity, averaged over the first 6 meters beneath the surface, covers an area of around 1-km-long and 1-km-wide (Figure 3.3), except in

vineyard fields where no measurements have been made due to the presence of 1m x 1m grid of metal stakes. Areas of lowest conductivity ($\simeq 10^{-2}$ S.m^{-1}), represented in yellow in Figure 3.3, may correspond to the coarsest and more permeable materials, while areas of highest conductivity ($\simeq 2.5\ 10^{-2}$ S.m^{-1}), represented in dark blue, may correspond to the finest and more cohesive materials (Figure 3.3). At a first glance, it appears that the river dikes seem bordered by large permeable areas of up to 400-m-wide and at least of 6-m-thick all along the section explored. In the Southern plain, these layers are delineated by fine and more cohesive materials, while the Northern plain seems dominated by materials of intermediate granulometry, represented in green, where the soil is probably more heterogeneous over the first 6 meters (Figure 3.3). The position of erosion signatures have been reported on Figure 3.3 and coincides with the presence of permeable layers, beyond which a sharp impermeable barrier seems impede their occurence farer down the protected plain. Examination of sediment cores, sampled near the dike toes along the study area, reveals that the most permeable materials are mostly made with a sandy matrice, from fine to coarse, with few silts, lots of gravels and pebbles, which may thicken over more than 15-m-deep beneath the surface (see S_2 on Figure 3.3). The finest weakly permeable materials are made of sandy marls and may constitute an impermeable substrate located at 12.20-m-deep at the position of S_1 in Figure 3.3, or more than 15-m-deep at the position of S_2 (Figure 3.3), while rising the surface farer from the dikes. In between, layers represented in green are mostly made with sandy silts to silty sands (see the top of samples which may correspond to the first 3-4 meters of the sedimentary boreholes). Complementary cross-section mapping of electrical resistivity allowed us to capture the lateral geometry and depth of this permeable reservoir beneath the surface. Profiles were performed at different positions along the upstream part of the embankment system, every 700 meters over 5-km-long from Rivesaltes to Claira, and across the river and dikes, which was made possible since the river was drought at the time of measurements. This represents a part of the PhD work of Edouardo Fogueng-Wafo that I co-supervised with Corinne Curt (IR. INRAe, RECOVER, Le Tholonet) and Stéphane Bonelli. We

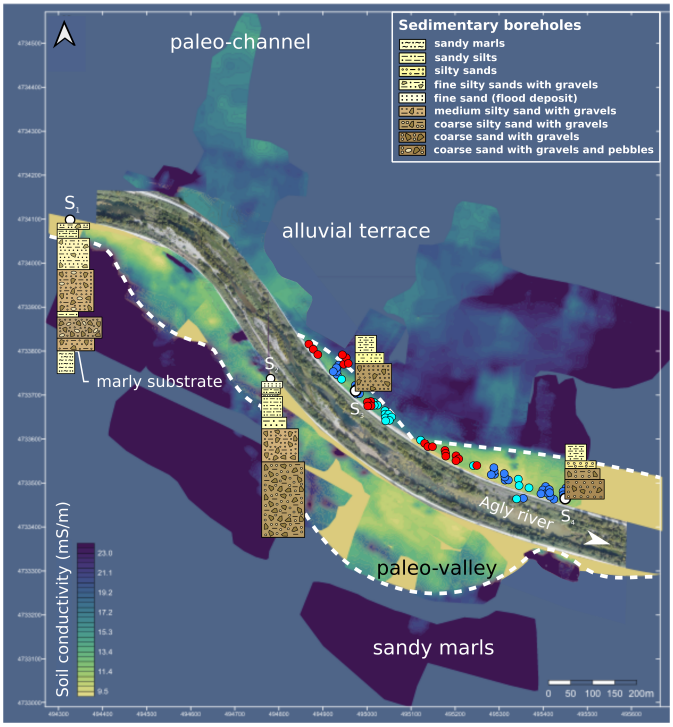

Figure 3.3

Surface mapping (EMI) of the soil conductivity performed in the study area using electromagnetic methods. The paleo-valley filled with fluvial deposits is delineated by dashed lines. Erosion signatures after the flooding event of March, 2013 have been reported. Sedimentary boreholes sampled in the Southern bank are 15-m-deep while those sampled in the Northern bank are 5-m-deep. The marly substrate evidenced by S_1 is located at 12.20m in depth.

roughly obtained three specific configurations exposed on Figure 3.4. The first one may correspond to a paleo-valley of around 350-m-wide and 20-m-deep, incised into a marly substrate, and filled with old highly permeable alluvial sediments mostly composed of gravelly-sands (Figure 3.4a). The second one may correspond to the paleo-valley whose center is located in the Southern protected plain, thus shifted from the present river bed, while its Northern edge arises at the vicinity of the dike toe (Figure 3.4b) which may potentially promote erosion processes in this area. The third one corresponds to the Northern edge of this valley, whose center is shifted in the Southern part relatively to

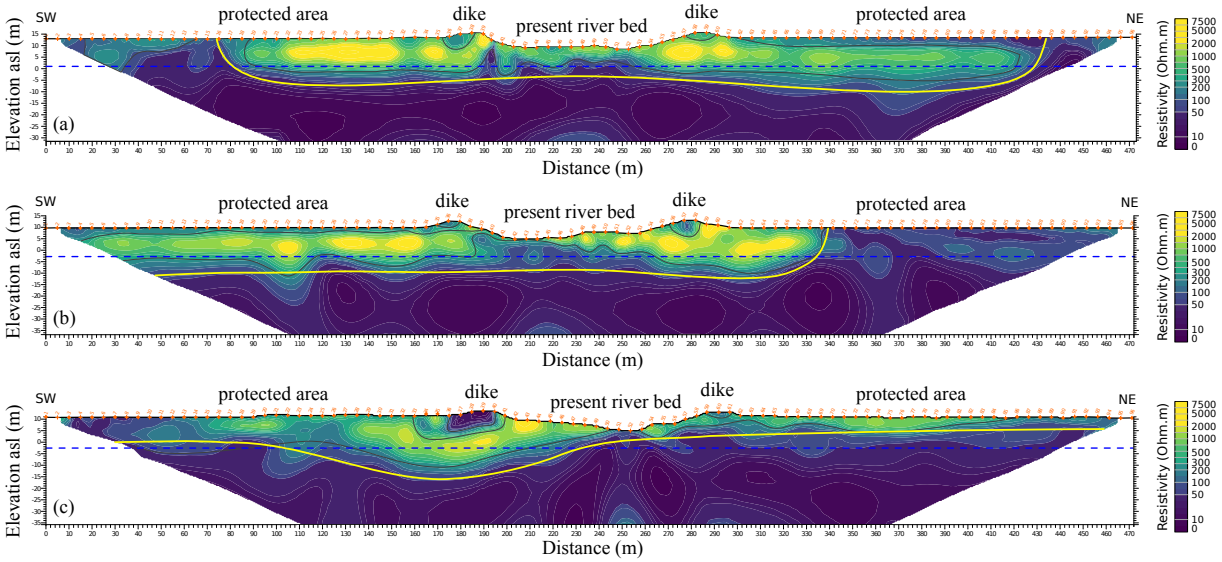

Figure 3.4

Three characteristic configurations observed from the section mapping of the soil electrical resistivity : (a) paleo-valley located beneath the present river bed ; (b) paleo-valley displaced to the South of the current river bed ; (c) Northern edge of the paleo-valley extended by a paleo-channel located beneath the Northern protected area.

the present river bed, which is extended by a thin and superficial paleo-channel located in the Northern alluvial plain (Figure 3.4c). Following the position of the paleo-valley along the study area (Figure 3.5) indicates that the valley is sometimes located beneath the present river bed, although quite larger, sometimes mostly located in the Southern protected area, while superficial paleo-channels of few meters thick are mostly located in the Northern alluvial plain. A specific mapping of these paleo-channels of around 2-m-thick, exposed in Figure 3.5, has been performed by Bastien Chareix during its Master 2 internship principally supervised by Jules Fleury (IR. CNRS, CEREGE, Aix-en-Provence) and Claude Vella (MC.U, CEREGE, Aix-en-Provence) and may explain the presence of heterogeneous soils over the first 6 meters in the Northern plain. Additional measurements of TDEM were performed along the electrical profiles to reliably capture the in-depth position of the sandy marls-gravelly sands interface (namely the base of the paleo-valley),

which may lack in most of the sedimentary boreholes.

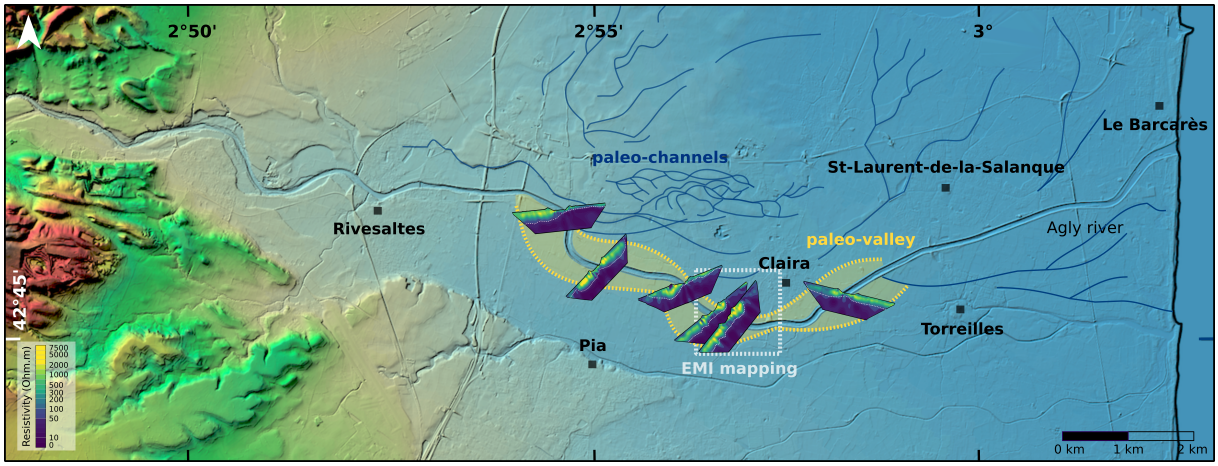

Figure 3.5

Schematic delimitation of the paleo-valley along the upstream embankment system inferred from the cross-section electric mapping ERT. The position of paleo-channels has been reported on the MNT (Source : https ://geoservices.ign.fr/rgealti).

The geomorphological interpretation of these tomograms thus requires the reconstruction of the river story. Agly is an ancient meandering/braided river, recently diked, that incised a valley down the sandy-marly subtrate during the last glaciation period (namely 18,000 years ago). The valley was then progressively filled with fluvial sediments (pebbles and gravels) and alluvial plain facies (sands and silts) during the last 12,000 years [Duvail (2008); Labaune *et al.* (2010)]. The geometry of the incurved permeable valley beneath the surface promotes the circulation of internal flows towards the protected plain during floods and thus erosion processes at the vicinity of the dikes. Near the edge of the valley, the bordering marly substrate forms an impermeable barrier that impedes internal flows to progress farer down the protected plain while promoting their ascent towards the surface. The presence of a thin superficial silty layer above a thick sandy layer promotes the formation of fluidization chimneys through the more permeable regions and may explain the occurence of leaks and sand-boils at the surface (Figure 3.3).

The presence of a paleo-channel in the extension of the edge of the valley gives way to a section thinning, from a 15-m-thick permeable reservoir to a 2-m-thick superficial channel, which may induce a significant increase in the internal flows velocity during floods and the development of fines erosion at the junction of the paleo-channel, able to explain the presence of sinkholes at the surface (Figure 3.3). Moreover, the accumulation of coarse sandy-gravelly deposits beside the river bed leads to the shaping of natural levees, which makes Agly a river perched at few meters above its alluvial plain. This morphological feature also represents an important factor of vulnerability which promotes the flooding of the alluvial plain through overflows, defluviations, or dike breaches during episodes of high water levels.

3.4 Erosion processes during repeated floods

The delineation of the permeable reservoir beneath the present river bed, inferred from the cross-section mapping, thus represents the starting point of geomechanical simulations in which scenarii of underlying seepage flows beneath a diked river may promote the soil erosion during flooding events. This investigation represents a part of the work of Bonelli & Girolami (2024) as well as that of Zezhi Deng (Chongqing University, China), invited during one year at INRAe during the final step of his PhD to pursue this research investigation, also driven in collaboration with Nadia Benahmed (CR. at RECOVER, Le Tholonet), Pierre Philippe (DR. at RECOVER, Le Tholonet) and Gang Wang (Pr.U at LNTCCMA, Chongqing University), while extending the numerical development to three dimensional large-scale simulations. First, two-dimensional numerical simulations, based on the finite element method, were initially developed on simplified geometries inferred from the geophysical results analysis to investigate the evolution of the solid volume fraction of fine particles in the foundation soil for different shapes of the paleo-valley or different positions of the paleo-channel regarding the dike toe, and this after repeated episodes of floods (up to 20, Figure 3.6). The model is based on mass and momentum

equations stated for Stokes flows in a porous media mostly composed of coarse gravels incorporated into a sandy matrice and overlying a sandy-marly substrate where each layer is described by a proper permeability [Bonelli & Girolami (2024)], and coupled through the internal flow velocity u_f to a simplified erosion law which describes the loss of fine particles from the sandy matrice during floods, such as progressively decreasing the rate of the solid volume fraction with time $\dot{\phi_s} = \frac{\partial \phi_s}{\partial t}$ into the paleo-reservoir, thus forming ultimately layers of open-framework gravels when $\phi_s = 0$ which may give rise to an erosion channel after repeated floods [Girolami *et al.* (2025)].

· The mass and momentum conservation of seepage flows are respectively given by :

$$\begin{aligned} \nabla \cdot \mathbf{u_f} &= 0 \\ \mathbf{u_f} &= -\tfrac{\kappa}{\mu_f} \left(\nabla p_p + \rho_f \mathbf{g} \right) \end{aligned} \tag{3.1}$$

where $\mathbf{u_f}$ represents the velocity vector of the seepage water flows, κ : the permeability of the sandy-gravelly sediments, and p_p : the pore pressure.

· The rate of the solid volume fraction of fine particles $\dot{\phi_s}$ eroded from the matrice of the sandy-gravelly reservoir during a flood is given by :

$$\begin{cases} \dot{\phi_s} = -\lambda_e \left(u_f - u_{f_c} \right) \phi_s \quad \text{when} \quad u_f > u_{f_c}\,, \\ \dot{\phi_s} = 0 \quad \text{when} \quad u_f \leq u_{f_c}\,. \end{cases} \tag{3.2}$$

where u_f represents the norm of $\mathbf{u_f}$, ϕ_s varies from ϕ_{pack} to 0 where ϕ_{pack} is the maximum volume fraction of the sandy packed matrice, λ_e is the erosion parameter (m^{-1}), and u_{f_c} : the threshold fluid velocity above which erosion is initiated.

The computational domain represents a study area of 430-m-large and 100-m-deep, including a part of the river bed and dike as well as the Northern protected plain, while taking a refined mesh into the paleo-valley of around 15-m-deep, 30-m-wide, and into the paleo-channel of around 3-m-thick and 60-m-large. Boundary conditions impose a high water level in the river during floods (at the crest level located at up to 6 m above the bed), with no leakage (*i.e.* $u_f = 0$, $p_p < p_{atm}$) at the dike crest, while considering water outflows ($p_p = p_{atm}$, $u_f \geq 0$) along the downstream part of the dike and at the surface

of the protected plain. The flood hydrography is modeled in a simplified way, taking a triangular evolution over a duration of 45 h similarly to those of historical floods recorded at Agly and a maximum water level at the dike crest. Four configurations of the paleo-reservoir were investigated. Configuration C_1 is almost tabular, while C_2, C_3, and C_4 incorporate a thinning of the permeable layer thickness, from 10 m to 2 m, where the edge of the valley is extended by a paleo-channel located at different positions from the dike toe, from 25 m to 2 m, while a low permeability topsoil covers the permeable region. Repetition of 20 scenarii of identical floods have been simulated. In between, the water table is assumed to be located at 4.5-m-deep in the floodplain, as measured on the field except during the drought periods. Simulation results expose that erosion of fine particles, represented in red (*i.e.* when $\frac{\phi_{pack}-\phi_s}{\phi_{pack}} \rightarrow 1$, as $\phi_s \rightarrow 0$) on Figure 3.6, first appears at the dike toe on the river side (water inlet), then at the dike toe on the protected plain (water outlet), thus beneath the dike, and along the edge of the valley where the thickness of the permeable layer thins, in all different geometries. Erosion is observed to essentially

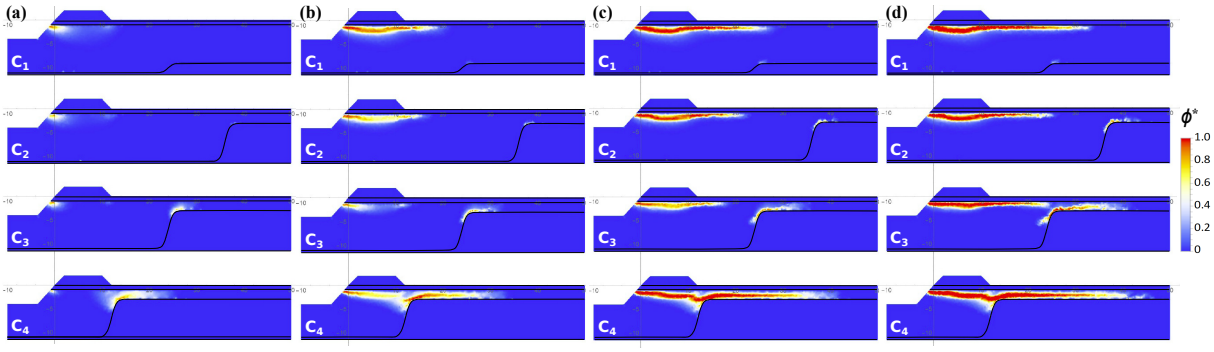

Figure 3.6

Numerical simulations of fines erosion represented by the ratio $\phi^* = \frac{\phi_{pack}-\phi_s}{\phi_{pack}}$ in the sandy-gravelly reservoir after (a) 1 flood; (b) 5 floods; (c) 10 floods; (d) 20 floods, for different geometries of the paleo-valley ($C_1 - C_4$). Eroded areas are represented in red ($\phi^* \rightarrow 1$).

develop progressively from the river to the protected floodplain, and to a lesser extent regressively from the protected floodplain to the river. Artesian conditions are reached

when the piezometric level h_e rises the surface, while the uplift of the topsoil occurs when the pore pressure p_p at the surface of the permeable reservoir exceeds that induced by the weight of the saturated surface layer. In the absence of topsoil, the increase of h_e may lead to the slow flooding of the protected area as the water table rises the surface through the permeable reservoir. In the presence of a low-permeability topsoil, the increase of h_e may lead to an increase of p_p at the base of the topsoil. The presence of defects in the surface layer represents a triggering factor of leaks and sand-boils, while fines erosion may lead to the formation of open-framework gravels as well as the occurrence of sinkholes at the surface [Bonelli & Girolami (2024); Deng *et al.* (2025)]. The repetition of floods

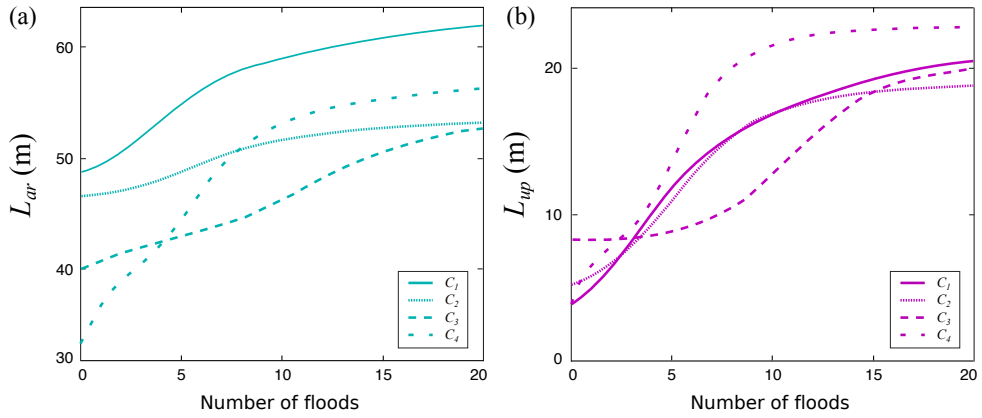

Figure 3.7

(a) Evolution of L_{ar} with the number of floods for different geometries of the paleo-reservoir ($C_1 - C_4$). (b) Evolution of L_{up} with the number of floods for C_1 to C_4.

(above 5) may promote the connexion of erosion layers and channeling when the edge of the valley is located at the vicinity of the dike toe (Figure 3.6). At the surface, the number of floods tends to extent the distance on which artesian flows L_{ar} and uplifts L_{up} may develop from the dike toe in the protected plain whatever the configuration (Figure 3.7). The geometry and position of the valley may also increase L_{ar} and L_{up}. The larger and deeper the paleo-valley (C_1), the more extended the region of artesian flows L_{ar} (Figure 3.7). The larger the paleo-channel (C_4), the more extended the region of uplifts

L_{up} (Figure 3.7). Despite the simplified description of erosion processes, the model turns out to provide relevant orders of magnitude of L_{ar} and L_{up}, in good agreement with field observations. These preliminary results will be pursued through the on-going PhD work of Edouardo Fogueng-Wafo from which a physical analysis and the determination of relevant non-dimensional groups will allow to predict the occurence of erosion signatures down the protected plains for a wide range of situations. Parallely, three-dimensional numerical

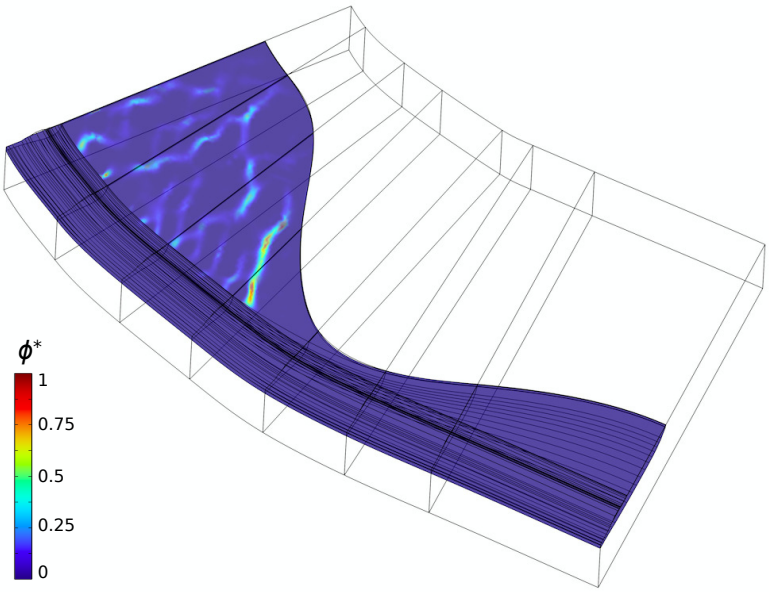

Figure 3.8

Illustration of fines erosion channels inferred from three-dimensional numerical simulations which consider a longitudinal meandering geometry for the permeable reservoir. Eroded areas are similarly represented in red ($\phi^* = \frac{\phi_{pack}-\phi_s}{\phi_{pack}} \rightarrow 1$).

simulations have been preliminarily developed to explore situations where longitudinal seepage flows, parallel to the river, may develop and impact the distribution of in-depth erosion channeling or surface signatures along the meandering valley (Figure 3.8) [Deng *et al.* (2025)]. The description of fines erosion would deserve to be enriched in the near future with laboratory experiments which may consist in reproducing a suspension of fine particles, through fluidization techniques, within a non-deformable porous media made

with coarse particles in the aim of determining a more general erosion law.

3.5 Monitoring the paleoenvironment of a diked river

Geophysical investigations and numerical results allow to propose a framework in which specific situations may explain the distribution of internal erosion signatures in the protected plain of a diked river during flooding events. In the case where an incurved paleo-valley, located beneath a diked river and filled with gravelly-sands, rises the surface of the protected plain, the piezometric level is intended to reach the surface during the event, causing the flooding of the plain by groundwater. In this situation, simulations expose the progression of an erosion channel after repeated floods, from the river to the dike toe, with a possible localized fluidization near the dike toe, also known as a heave or a sandy blowout, which may possibly lead to the formation of sinkholes after the peak flooding. Many examples of sinkholes evidenced near the dike toes have been recorded after the major flooding events of Agly (1999 ; 2013 ; 2014 ; 2018 ; 2020). The presence of a paleo-channel in the extension of the edge of the valley may lengthen the flooding area.

In the case where the incurved paleo-valley, filled with gravelly-sands, is covered by a cohesive topsoil, the excess of pore pressure located at the surface of the saturated reservoir will promote the development of leaks and sand-boils through the most permeable regions or defects, especially at the vicinity of the dike toes and above the edge of the valley. In this situation, simulations expose local open-framework gravels beneath sand-boils areas which can lead to the collapse of the overlying layers and the occurence of sinkholes after the peak flooding. Examples of leaks, sand-boils, and conical sinkholes evidenced at the vicinity of the dikes have been recorded after major flooding events. In the case where the cohesive topsoil is locally roughly homogeneous, thus longitudinal effects may become significant and require a three-dimensional modeling. The presence of a paleo-channel in the extension of the edge of the valley may preferentially extent the uplift area or rather the artesian region, regarding to its position from the dike. Simulations expose

the progression of an erosion channel, after repeated episodes of floods, beneath the dike and along the paleo-channel. Examples of roughly ellipsoidal sinkholes with a flat bottom have been recorded above the entrance of the paleo-channel after a major flooding event of Agly. These preliminary findings may deserve a more detailed description enriched by the observation of the spatio-temporal evolution of the subsoil during a flood. The installation of piezometers and pressure sensors over 20 m in depth will enable us to instrument a 4-km-long and 1-km-wide study area, located from Rivesaltes to Claira, to explore in detail the water table dynamics and its interactions with the river, as well as the formation of potential erosion channels and their surface manifestation during successive flooding episodes. This work constitutes a part of the PhD work of Edouardo Fogueng-Wafo and that of Jules Burgat (PhD candidate to an on-going CIFRE project with DRIM).

3.6 Conclusion

After having explored in detail the sedimentation processes in small-scale concentrated flows, we now explored the erosion of saturated porous media in large-scale situations, such as the floodplain protected by river dikes. These processes turn out to appear at the vicinity of the embankment system during floods or periods of high water level. Surface and cross-section geophysical observations enriched by sedimentary boreholes performed in areas, known as the most affected by such processes during floods, reveal the presence of an incurved paleo-valley, filled with gravelly-sands, which explains the origin of internal erosion signatures (leaks, sand-boils, sinkholes) observed at the vicinity of the dike toes after major flooding events of Agly river (Pyrénées-Orientales). Imaging the paleo-valley along the embankment system indicates that the permeable reservoir is not always located beneath the present river bed and mainly extents beneath the Southern floodplain. Numerical simulations of the sandy matrice erosion of the saturated reservoir, induced by underlying seepage flows during floods, allows us to explain the distribution of the surface signatures which may depend on the geometry and position of the valley from the dike

toe, as well as on the presence of a thin superficial cohesive topsoil. These preliminary observations should be enriched by a dimensional analysis for the development of a more general description applied to a wide range of situations, as well as on the spatio-temporal monitoring of the subsoil erosion during repeated episodes of flood through the instrumentation of the study area to explore the water table dynamics as well as the progression of erosion processes in depth and at the surface, that will help improving the physical description to be implemented in three-dimensional numerical simulations.

Chapitre 4

Brief synthesis of the research work

4.1 Summary of the career path

Academic Positions

· **Since 2022** : Invited Researcher at **RECOVER**, INRAe−AMU, Aix-en-Provence.

· **Since 2014** : Associate Professor at **GéHCO**, University of Tours.

· **Collaborations :** IMFT ; INRAe ; IDP ; LIENSs ; ISTO ; METIS ; CEREGE.

· **Teaching :** $\simeq$ 210 hours/year.

· **BSc. Degree :** Earth Interior, Volcanology, Hydrodynamics, Natural Hazards.

· **MSc. Degree :** Flooding events, Dikes erosion and Dam breaks.

· **Responsability :** Manager of the first year of the BSc. (2015-2019).

· **Supervising** & **Co-supervising** : - Postdoc : A. Bondesan (2020-2021).

- PhD : I. Hmamou (2024-2027) ; E. Fogueng-Wafo (2024-2027) ; N. Chaouch (2023-2026) ; L. Rousseau (2021-2024) ; A. Amin (2018-2022).

- Research Engineer : F. Godet (2017-2018) ; R. Morini (2016).

- MSc. 2 : E. Fogueng-Wafo (2024) ; B. Chareix (2024) ; J. Burgat (2023) ; L. Rousseau (2021) ; C. Talbot (2021) ; K. Conan (2020) ; M. Gschwend (2020) ; P-F. Vittoz (2020) ; H. Guery (2019) ; T. Tessier (2018) ; M. Bergeot (2018) ; B. Lezoul (2018).

- MSc. 1 : H. Giraud (2021) ; K. Coffi (2021) ; K. Conan (2019).
- BSc. 3 : B. Perret (2024) ; M. Moumeni (2021) ; T. Pereira (2020) ; G. Osorio (2018) ; K. Conan (2018).
- BSc. 2 : K. Conan (2017).
- TPE : Paul Louis Courier High School (2016-2017).

Research Experiences

· **2012−2014 :** Postdoctoral position (Fluid Dynamics) at Institut de Mécanique des Fluides de Toulouse (**IMFT**) with Pr. François Charru & Pr. John D. Sherwood (DAMTP, University of Cambridge, UK). Title : Theoretical study of the sediment transport in a pipe.

· **2011−2012 :** Postdoctoral position (Volcanology) at Geological Survey of Japan (**AIST**) and Center for GeoHazard Study (**SUNY**, Buffalo, USA) with Dr. Shinji Takarada (AIST, Japon) & Pr. Eliza Calder (SUNY, Buffalo, USA).Title : Segregation processes during granular collapses.

· **2010−2011 :** ATER (Geosciences) at Geosciences & Environment Lab. (**GEC**).

· **2009−2010 :** Postdoctoral position (Solid Mechanics) at Institut Français du Pétrole (**IFP-EN**), with Pr. Anthony Wachs (UBC, Canada) & Dr. Guillaume Vinay (IFP-EN). Title : Discrete modeling of the collapse of granular flows.

· **2008 :** Editor (Volcanology), UNESCO project at General Council of Puy de Dôme.

Educational Background

· **2004−2008 :** PhD Thesis (Volcanology) at Laboratoire Magmas et Volcans (**LMV**), under the direction of Pr. Tim H. Druitt (LMV). Title : Dynamics and sedimentation of small-scale pyroclastic flows.

· **2003−2004 :** Master (Internal Geophysics) at Institut de Physique du Globe de Paris (**IPGP**), under the direction of Pr. Claude Jaupart (IPGP). Title : Growth and destabilisation of lava domes and spines.

Research Projects

· **2024−2029 :** Member of the target project "Complex Flows", PEPR Maths-VivES.

· **2024−2026 :** Scientific leader of AQUA Geoφ (2), Funding Institut CARNOT.

· **2024−2026 :** PI of AQUA Geoφ, with A. Mesgouez, Funding Région Sud.

· **2023−2024 :** Co-Investigator of PALÉRO, with R. Valois, Funding ECCOREV.

· **2022−2024 :** Co-Investigator of DIG-OBS, with S. Bonelli, Funding INRAe.

· **2021−2022 :** Co-Investigator of GÉO-MOD, with M. Gralepois, Funding UT.

· **2020−2024 :** Co-Investigator of RhéFlEXes, with F. James, Funding Région CVL.

· **2016−2019 :** Principal Investigator (PI) of MAGIC, Funding Région CVL.

· **2015−2016 :** Principal Investigator (PI) of PRÉDIRE, Funding FEDER-AELB.

· **2012−2014 :** CNRS-JSPS Fellowship, 2 years (AIST, Tsukuba, Japan), declined.

· **2011−2012 :** JSPS Fellowship, 1 year (AIST, Tsukuba, Japan).

Collective acts

· **Organization :** Member of the scientific committee of the 1^{st} International Symposium on Mechanics (Aberdeen, UK, July 2018).

· **Dissemination :** Workshops at "Fête de la Sciences" (2014−2024) : "The physics of the sand heap", "Walking on the water surface".

- Production of an educational movie on "Rheology of complex fluids" (2018−2019) : https://inwicast.univ-tours.fr/videos/?video=MEDIA191008123524678 with Guillaume Osorio, Agnès Montibert, Nataliya Sandier.

· **Evaluation :** $\simeq$ 3−5 publications / year for journals : Nature Geosciences, Nature Review of Earth Sciences and Environment, Physics of Fluids, Journal of Fluid Mechanics, International Journal of Multiphase Flows, Applied Mathematical Modelling, Fluids, Energies, Journal of Marine Science and Engineering, Journal of Mountain Sciences, Applied Sciences.

· **Scientific expertise :** Review of a regional project : AAP-ESR Région Nouvelle-Aquitaine (2021) ; Review of an international project : Ministry of Infrastructure and

Water State (Netherlands, 2023).

· **Responsabilites :** Member of the Cultural Council of UT (2016−2022) ;

- GéHCO Correspondent for the CaSciMoDOT federation (2022−*present*) ;

- MC. U Selection committees (IUSTI, 2024 ; GéoAzur, 2023 ; Institut P', 2022 ; GéHCO, 2016) ;

- President of "High School Diploma" juries (July 2021, July 2016).

4.2 Experiences of supervision

· **Supervision of PhD students**

· **Ahmad Amin (2018-2022)**, GéHCO Lab., EMSTU, defended on 27.06.2022.

· PhD Advisor : Florentina Moatar, RIVERLY, INRAe.

· Co-supervisor : Laurence Girolami, GéHCO Lab., University of Tours.

· Title : Sedimentation and dynamics of liquid-solid suspensions.

· Funding : Region Centre Val-de-Loire, from 20/10/2018 to 27/06/2022.

· Publications :

[1] A. Amin, L. Girolami, F. Risso (2021) On the fluidization/sedimentation velocity of a homogeneous suspension in a low-inertia fluid, *Powder Technology*, 391.

[2] A. Amin, L. Girolami, F. Risso (2022) Fall of a large sphere in a suspension of small fluidized particles, *Physical Review Fluids Letters*, 7, L082301.

[3] L. Girolami, F. Risso, A. Amin, L. Rousseau, A. Bondesan, S. Bonelli (2024) Sedimentation of short-lived fluid-solid suspensions, *Physics of Fluids*, 36, 113308.

· Present position : Developer-consultant at Salesforce (Paris).

· **Loïc Rousseau (2021-2025)**, GéHCO Lab., EMSTU, to be defended.

· PhD Advisor : Mohammed Boussafir, GéHCO Laboratory.

· Co-supervisors : Laurence Girolami & Frédéric Risso (IMFT, Toulouse).

· Title : Properties of inhomogeneous liquid-solid suspensions.

· Funding : EMSTU & UT Scholarship, from 15/11/2021 to 15/11/2024.

· Publications :

[1] L. Girolami, F. Risso, A. Amin, L. Rousseau, A. Bondesan, S. Bonelli (2024) Sedimentation of short-lived fluid-solid suspensions, *Physics of Fluids*, 36, 113308.

[2] A. Bondesan, L. Girolami, F. James, L. Rousseau (2025) A three-layers model for particulate suspensions driven by sedimentation, *PoF*, doi :10.1063/5.0261889.

[3] L. Rousseau, L. Girolami, F. Risso, M. Boussafir (2025) Propagation of concentrated waves in liquid-solid fluidized beds, *Physical Review Fluids*, in revision.

· Present position : ATER (GéHCO).

· **Edouardo Fogueng-Wafo (2024-2027)**, RECOVER (INRAe), ED 251, AMU.

· PhD Advisors : Corinne Curt, RECOVER & Laurence Girolami, RECOVER.

· Co-supervisor : Stéphane Bonelli, RECOVER.

· Title : Observation of the paleo-environment of a diked river.

· Funding : AMU President Scholarship, Starting date : 05/11/2024.

· Publications :

[1] E. Fogueng-Wafo, L. Girolami, S. Bonelli, C. Camerlynck, J.-M. Carozza, C. Curt (2025) Influence of the deltaic paleo-environment of a diked river on the soil erosion in the protected flood-plain, in preparation.

[2] L. Girolami, S. Bonelli, J.-M. Carozza, E. Fogueng-Wafo, J. Burgat, N. Chaouch, R. Valois (2024) On the origin and distribution of erosion signatures around flood protection dikes, *Journal of Flood Risk Management*, doi :10.1111/jfr3.70104.

· **Ibrahim Hmamou (2024-2027)**, Institut Denis Poisson, MIPTIS, Univ. Orléans.

· PhD Advisors : Carine Lucas, IDP & Laurence Girolami, GéHCO-RECOVER.

· Co-supervisors : Olivier Delestre, LJAD.

· Title : Multi-layers description and modeling of dam-break suspension flows dominated by sedimentation.

· Funding : PEPR Maths-VivES : “Complex flows”, ANR, Starting date : 15/10/2024.

· **Naïm Chaouch (2024-2027)**, RECOVER (INRAe), ED 353, AMU.

· PhD Advisors : Stéphane Bonelli, RECOVER & Jean-François Chaix, LMA.

· Co-supervisors : Nadia Benahmed, Laurence Girolami, Pierre Philippe, RECOVER.

· Title : Contribution of seismic methods for the detection of soil heterogeneities.

· Funding : INRAe, Starting date : 01/01/2024.

· Publications :

[1] L. Girolami, S. Bonelli, R. Valois, N. Chaouch, J. Burgat (2023) On internal erosion of the pervious foundation of protection dikes, *Water*, doi : 10.3390/w15213747.

[2] L. Girolami, S. Bonelli, R. Valois, N. Chaouch, J. Burgat, F. Nicoleau (2024) Correlation between fluvial morphodynamics and processes of internal erosion around dikes, *Revue Française de Géotechnique*, 178(7).

[3] L. Girolami, S. Bonelli, J.-M. Carozza, E. Fogueng-Wafo, J. Burgat, N. Chaouch, R. Valois (2024) On the origin and distribution of erosion signatures around flood protection dikes, *Journal of Flood Risk Management*, doi :10.1111/jfr3.70104.

· Present position : Study engineer at RECOVER (INRAe).

· **Supervision of Postdocs and research engineers**

· **Andrea Bondesan (2020-2021)**, Postdoc, Institut Denis Poisson.

· Supervisors : François James, IDP & Laurence Girolami, GéHCO.

· Title : Numerical modeling of dam-break suspension flows.

· Funding : Region Centre Val-de-Loire, from 01/03/2020 to 31/03/2021.

· Publications :

[1] A. Bondesan, L. Girolami, F. James, L. Rousseau (2025) A three-layers model for particulate suspensions driven by sedimentation, *PoF*, doi :10.1063/5.0261889.

[2] L. Girolami, F. Risso, A. Amin, L. Rousseau, A. Bondesan, S. Bonelli (2024) Sedimentation of short-lived fluid-solid suspensions, *Physics of Fluids*, 36, 113308.

· Present position : Marie-Curie Fellow at the "Dipartimento di Scienze Matematiche, Fisiche e Informatiche", University of Parma.

· **Florian Godet (2017-2018)**, Research engineer, GéHCO, University of Tours.

· Advisor : Laurence Girolami, GéHCO Lab.

· Title : Experimental tests driven on the dam-break hydraulic flume.

· Funding : Region Centre Val-de-Loire, from 15/02/2017 to 15/07/2018.

· **Romain Morini (2016-2017)**, Research engineer, GéHCO, University of Tours.

· Advisor : Laurence Girolami, GéHCO Lab.

· Title : Design of an experimental device : fluidization rig, flume, rheometer.

· Funding : FEDER-AELB, from 15/01/2016 to 15/01/2017.

· **Main supervision of Master-2 students**

· **Edouardo Fogueng Wafo (2024)**, Master-2 student at University of Grenoble.

· Advisors : Laurence Girolami and Stéphane Bonelli, RECOVER.

· Title : Geophysical observation of soils affected by internal erosion around dikes.

· **Jules Burgat (2023)**, Engineer student at Seatech Toulon.

· Advisors : Stéphane Bonelli and Laurence Girolami, RECOVER.

· Title : Inversion model of electrical measurements of subsoils around river dikes.

· **Loïc Rousseau (2022)**, Master-2 student at University of Côte d'Azur.

· Advisor : Laurence Girolami, GéHCO Lab.

· Title : Physical and numerical modeling of lahars.

· **Matthieu Gschwend (2020)**, Master-2 student at University of Montpellier.

· Advisors : François James, IDP & Laurence Girolami, GéHCO.

· Title : Numerical modeling of the dam-break flow of gas-solid suspensions.

· **Killian Conan (2020)**, Master-2 student at University of Brest.

· Advisor : Laurence Girolami, GéHCO Lab.

· Title : Role of the solid concentration on the dynamics of turbidity currents.

4.3 Research dissemination

· **List of scientific publications**

[24] Z. Deng, **L. Girolami**, N. Benahmed, P. Philippe, S. Bonelli, G. Wang (2025) Large-scale numerical insights of suffusion processes beneath river dikes : impact on erosion signatures, *Water Resources Research*, submitted.

[23] Z. Deng, N. Benahmed, **L. Girolami**, P. Philippe, S. Bonelli, G. Wang (2025) Numerical investigation of internal erosion mechanisms regarding stratigraphy : Agly dike case study, *Engineering Geology*, 353 (108118), doi :10.1016/j.enggeo.2025.108118.

[22] S. Bonelli, **L. Girolami** (2024) Internal erosion of sandy gravel and occurence of open-framework gravels in the subsoil of a river dike, *Geomechanics for Energy and Environment*, 100690, doi :10.1016/j.gete.2025.100690.

[21] **L. Girolami**, S. Bonelli, J.-M. Carozza, E. Fogueng-Wafo, J. Burgat, N. Chaouch, R. Valois (2024) On the origin and distribution of internal erosion signatures in the floodplain protected by river dikes, *Journal Flood Risk Management*, doi :10.1111/jfr3.70104.

[20] A. Bondesan, **L. Girolami**, F. James, L. Rousseau (2024) A three-layers model for the flow of particulate suspensions driven by sedimentation, *Physics of Fluids*, 37, doi :10.1063/5.0261889.

[19] **L. Girolami**, F. Risso, A. Amin, L. Rousseau, A. Bondesan, S. Bonelli (2024) Sedimentation of short-lived fluid-solid suspensions, *Physics of Fluids*, 36, 113308, https ://doi.org/1063/5.0231788.

[18] A Ghorbani, A. Revil, S Bonelli, S Barde-Cabusson, **L. Girolami**, F Nicoleau, P Vaudelet (2024) Occurrence of sand boils landside of a river dike during flooding : A geophysical perspective, *Engineering Geology*, 329, 107403.

[17] **L. Girolami**, S. Bonelli, R. Valois, N. Chaouch, J. Burgat, F. Nicoleau (2024) Correlation entre morphodynamique fluviale et processus d'érosion autour des digues : observation multi-échelle d'une rivière aménagée, *Revue Française de Géotechnique*, 178(7),

https ://doi.org/10.1051/geotech/2024010.

[16] **L. Girolami**, S. Bonelli, R. Valois, N. Chaouch, J. Burgat (2023) On internal erosion of the pervious foundation of flood protection dikes, *Water*, 15, 3747, https ://doi.org/10.3390/w15213747.

[15] A. Amin, **L. Girolami**, F. Risso (2022) Fall of a large sphere in a suspension of small fluidized particles, *Physical Review Fluids Letters*, 7, L082301.

[14] A. Amin, **L. Girolami**, F. Risso (2021) On the fluidization/sedimentation velocity of a homogeneous suspension in a low-inertia fluid, *Powder Technology*, 391, doi.org/10.1016/j.powtec.2021.05.073.

[13] C. Soulaine, **L. Girolami**, L. Arbaret, S. Roman (2021) Digital Rock Physics : computation of hydrodynamic dispersion, *Oil & Gas Science and Technology*, 76 (51), doi.org/10.2516/ogst/2021032.

[12] **L. Girolami**, F. Risso (2020) Physical modeling of the dam-break flow of sedimenting suspensions, *Physical Review Fluids*, doi :10.1103/PhysRevFluids.5.084306.

[11] **L. Girolami**, F. Risso (2019) Sedimentation of gas-fluidized particles with random shape and size, *Physical Review Fluids*, doi :10.1103/PhysRevFluids/4.074301.

[10] **L. Girolami**, F. Risso (2018) Rheological behaviour and runout of short-lived fast-moving flows of dense suspensions, *J. Energy Challenges & Mechanics*, 5(1), 17-23.

[9] **L. Girolami**, J. D. Sherwood and F. Charru (2016) Dynamics of a slowly-varying sand bed in a circular pipe, *International Journal of Multiphase Flows*, 81, 113-129.

[8] **L. Girolami**, T. H. Druitt and O. Roche (2015) Towards a quantitative understanding of pyroclastic flows : Effects of expansion on the dynamics of laboratory fluidized granular flows, *Journal of Volcanology and Geothermal Research*, 296, 31-39.

[7] G. F. Bertrand, H. Celle-Jeanton, F. Huneau, A. Baillieux, G. Mauri, V. Lavastre, G. Undereiner, **L. Girolami** and J.S. Moquet (2015) Vulnerability of volcanic aquifers : evaluation of contaminant transfer and hydrodispersive parameters in basaltic lava flows through an artificial tracer test and implications for long-term water supply management, *Open Geosciences*, doi :10.1515/geo-2015-0037.

[6] **L. Girolami**, A. Wachs and G. Vinay (2013) Unchannelized dam-break flows : effects of the lateral spreading on the dynamics, *Phys. Fluids*, doi :10.1063/1.4799 129.

[5] A. Wachs, **L. Girolami**, G. Vinay and G. Ferrer (2012) GRAINS3D, a flexible DEM approach for particles of arbitrary convex shape : numerical model and validations, *Powder Technology*, doi :10.1016/ j.powtec.2012.03.023.

[4] **L. Girolami**, V. Hergault, G. Vinay and A. Wachs (2012) A Three-dimensional DEM for the simulation of dam-break granular collapses : comparison between numerical results and experiments, *Granular Matter*, doi :10.1007/s10035-012-0342-3.

[3] **L. Girolami**, O. Roche, T. H. Druitt and T. Corpetti (2010) Particle velocity fields and depositional processes in laboratory ash flows, with implications for the sedimentation of dense pyroclastic flows, *Bulletin of Volcanology*, doi :10.1007/s00445-010-0356-9.

[2] A. Wachs, G. Vinay, G. Ferrer, J. Kouakou, C. Dan and **L. Girolami** (2009) PeliGRIFF : a parallel Discrete Element Method-Distributed Lagrange Multiplier/ Fictitious Domain for a direct numerical simulation of particulate flows with collisions, *International Journal of Mechanical Systems Science and Engineering*, 1 (4), 185-191.

[1] **L. Girolami**, T. H. Druitt, O. Roche and Z. Khrabrykh (2008) Transport and hindered settling of laboratory ash flows, *Journal of Geophysical Research*, 113, doi :10.1029/ 2007JB005074.

· List of international meetings

† Oral presentation ‡ Poster

[37] E. Fogueng-Wafo, **L. Girolami**, S. Bonelli, C. Curt (2025) Delineation of the paleo-valley of a diked river using geophysical methods†, *EWG-IE*, June 23-28, Brno, Czech Republic.

[36] **L. Girolami**, F. Risso, A. Amin, L. Rousseau, A. Bondesan, S. Bonelli (2025) Sedimentation of fluid-solid suspensions†, *ICMF*, May 11-16, Toulouse, France.

[35] L. Rousseau, **L. Girolami**, F. Risso, M. Boussafir (2025) Propagation of concentrated waves in liquid-solid fluidized beds‡, *ICMF*, May 11-16, Toulouse, France.

[34] **L. Girolami** E. Fogueng-Wafo, S. Bonelli, J.-M. Carozza, C. Camerlynck (2024) Detection of the paleo-environment of a diked river : implications for the erosion of foundations soils†, *29th EWG-IE Workshop*, September 9-13, Bologna, Italy.

[33] S. Bonelli, **L. Girolami** (2024) Numerical modeling of internal erosion in the foundation of river dikes†, *29th EWG-IE Workshop*, September 9-13, Bologna, Italy.

[32] Z. Deng, S. Bonelli, **L. Girolami**, N. Benahmed, P. Philippe, G. Wang (2024) Numerical simulation of erosion mechanisms in Agly dikes†, *29th EWG-IE Workshop*, September 9-13, Bologna, Italy.

[31] Z. Deng, N. Benahmed, **L. Girolami**, P. Philippe, S. Bonelli, G. Wang (2024) Three-dimensional numerical study on the internal erosion mechanism of the Agly dike‡, *35th ALERT Workshop*, September 30th-October 5th, Aussois, France.

[30] **L. Girolami**, F. Risso, A. Amin, A. Bondesan, S. Bonelli (2024) Sedimentation of short-lived suspensions flows†, *ICTAM*, AO-FM07-0298, August 25-30, Daegu, Korea.

[29] A. Bondesan, **L. Girolami**, F. James, L. Rousseau (2024) A three-layer model for the dam-break flow of particulate suspensions driven by sedimentation†, *ICTAM*, AO-FM07-2251, August 25-30, Daegu, Republic of Korea.

[28] **L. Girolami**, E. Fogueng-Wafo, S. Bonelli, J.-M. Carozza, C. Camerlynck (2024) Detection of paleo-environments along a diked river to understand the origin and distribution of internal erosion processes : Application to the Agly embankment system†, *Meeting of advanced river monitoring systems*, June 20-21, Parma, Italy.

[27] M. Abily, G. Antoine, O. Delestre, **L. Girolami**, N. Goutal, F. Taccone (2024) Simulation of precipitation-generated debris flows in the Laval Basin, France†, *15th International Conference on Hydroinformatics*, May 27-30, Beijing, China.

[26] **L. Girolami**, S. Barde-Cabusson, A. Ghorbani, P.. Vaudelet, A. Revil, R. Valois, C. Vella, J-M. Carozza, J. Burgat, N. Chaouch, F. Nicoleau, S. Bonelli (2023) Correlation between paleo-channels and internal erosion around protecting dikes†, *29th EWG-IE Workshop*, Lyon, France.

[25] **L. Girolami**, F. Risso, A. Amin, L. Rousseau (2023) Sedimentation of a concen-

trated suspension during a dam-break flow†, *EuroMech*, June 26-30, Nice, France.

[24] F. Risso, **L. Girolami**, A. Amin (2023) Effect of particle inertia on the sedimentation and stability of a homogeneous suspension†, *EuroMech*, June 26-30, Nice, France.

[23] L. Rousseau, **L. Girolami**, F. Risso, M. Boussafir (2023) Fall of a sphere into a liquid-solid suspension of variable concentration†, *19th Multiphase Flow Conference : Simulation, Experiment & Application*, Dresden, Germany, June 19-23 2023.

[22] F. James, M. Gschwend, **L. Girolami**, F. Risso (2020) Physical modeling of small-volume pyroclastic flows†, *AGU Fall Meeting Abstracts 2020*, V008-0021.

[21] A. Amin, K. Conan, **L. Girolami**, F. James (2020) Sediment transfer from settled rivers to margins†, *AGU Fall Meeting Abstracts 2020*, NH002-0002.

[20] K. Conan, A. Amin, **L. Girolami**, F. James (2020) Dynamics of submarine avalanches : insights from small-scaled experiments†, *AGU Fall Meeting*, NH002-0003.

[19] **L. Girolami**, F. Risso (2019) Dam-break flow of a gas-particle suspension : application to pyroclastic flows†, 1*st International Conference on Multiphase Flows*, May 19-24, Rio de Janeiro, Brazil.

[18] **L. Girolami**, F. Risso (2018) Rheological behaviour and runout of short-lived, fast-moving suspensions flows†, 1*st Symposium on Mechanics*, July 9-12, Aberdeen, UK.

[17] **L. Girolami**, F. Godet, R. Morini, F. Risso (2017) Sediment transfer from settled rivers to margins‡, *The British Society of Rheology Mid-Winter Meeting 2017 : Rheology and flow of multiphase geological materials*, December 18-19, Bristol, UK.

[16] **L. Girolami** and F. Charru (2013), Fluid modeling in a partially-filled pipe†, *Workshop on Numerical Modeling of Fluid-Grains Mixtures*, ENS, Lyon, France.

[15] **L. Girolami**, A. Wachs, G. Vinay (2013), Unchannelized dam-break flows : effect of the lateral spreading on the flow dynamics†, IAVCEI Assembly, Kagoshima, Japan.

[14] **L. Girolami**, T. H. Druitt, O. Roche (2012), On the prediction of scaling relationships governing the runouts of short-lived fluidized granular flows‡, *1st Workshop of Asia-Pacific Earthquake and Volcanic Eruption Risk Management*, Tsukuba, Japan.

[13] **L. Girolami**, T. H. Druitt, O. Roche (2009), Insights from laboratory experi-

ments into the physics of pyroclastic flows†, *AGU*, 90(52), EOS Trans., V21G-07.

[12] **L. Girolami**, T. H. Druitt, O. Roche (2009), Laboratory ash flows†**,** *Commission on Explosive Volcanism Workshop*, Clermont-Ferrand, France.

[11] A. Wachs, G. Vinay, G. Ferrer, J. Kouakou, C. Dan, **L. Girolami** (2009), PeliGRIFF (Part 1) : a parallel Discrete Element Method-Distributed Lagrange Multiplier/ Fictitious Domain for a direct numerical simulation of particulate flows with collisions†, *International Conference on Chemical Engineering (W.C.S.E.T.)*, Tokyo, Japan.

[10] G. Vinay, A. Wachs, C. Dan, **L. Girolami** (2009), PeliGRIFF (Part 2) : a direct numerical simulation of heat transfer in particulate flows†,*International Conference on Chemical Engineering (W.C.S.E.T.)*, Tokyo, Japan.

[9] **L. Girolami**, T. H. Druitt, O. Roche (2007), Sedimentation of laboratory-scaled pyroclastic flows†, *Workshop on fluidization*, Department of Mechanical Engineering, University of Bristol, UK.

[8] **L. Girolami**, T. H. Druitt, T. Corpetti, O. Roche (2007), Dynamics of experimental rapid sheared flows‡, *American Geophysical Union*, 88(52), EOS Trans., V31E-0706.

[7] **L. Girolami**, T. H. Druitt, O. Roche (2007), Dynamics of laboratory ash flows†, *International Union of Geophysics and Geodesy (IAVCEI).*

[6] **L. Girolami**, T. Corpetti, O. Roche, T. H. Druitt (2007), High-speed video analysis of laboratory ash flows‡, *International Union of Geophysics and Geodesy (IAVCEI).*

[5] Z. Khrabrykh, T. H. Druitt, **L. Girolami**, K. Kelfoun (2007), Modelling of laboratory ash flows‡, *International Union of Geophysics and Geodesy (IAVCEI).*

[4] **L. Girolami**, T. H. Druitt, O. Roche (2007), Transport and sedimentation of laboratory ash flows†,*4th EGU General Assembly, Geophysical Research Abstract*, 9, 04891.

[3] **L. Girolami**, T. H. Druitt, O. Roche (2006), Propagation of experimental pyroclastic flows‡, *American Geophysical Union*, 87(52), EOS Trans., H53D-0656.

[2] H. Massol, **Girolami L.**, C. Jaupart (2005), The extrusion of spines during dome forming eruption‡, *2nd EGU General Assembly, Geophysical Research Abstract*, 7, 08931.

[1] H. Massol, C. Jaupart, **L. Girolami** (2004), A 2-D temperature dependant finite-

element model for non-fragmented conduit magma flow†, *1st EGU General Assembly, Geophysical Research Abstract*, 6, 06151.

4.4 Previous research activities

After having completed my Master degree in geophysics at the "Institut de Physique du Globe de Paris", I chose to complete my PhD at the Laboratory "Magmas et Volcans" (University of Clermont-Auvergne) under the direction of Tim Druitt (Pr U, LMV, Clermont-Ferrand), which was devoted to the description of the transport and deposition of pyroclastic flows reproduced in small-scale experiments. Upon my arrival, I designed and built a dam-break flume, in collaboration with Jean-Louis Fruquière (Research technician at LMV), capable of withstanding to high temperatures (200°C), in the aim of reproducing novel suspension flows composed of non-cohesive volcanic ash and air. The objective of this work lied on the detailed description of experiments to propose scaling laws for the prediction of their runouts from the control parameters. During this work, I developed a collaboration with Thomas Corpetti (DR. CNRS, LETG, University of Rennes 2) who developed a tool to optimize the estimation of motion from image sequences analysis, which allowed us to study the internal flow structures developed during propagation.

Then, I completed a postdoctoral project at the "Institut Français du Pétrole et Énergies Nouvelles" in collaboration with Anthony Wachs (Pr U, Department of Mathematics and Department of Chemical & Biological Engineering, University of British Columbia) where I worked on the parallelization and validation of a numerical code based on the discrete element method *Grains3D* in the aim of reproducing gravitational collapses of granular columns involving a reasonable number of particles. The philosophy of this approach consists in modeling the system at the scale of the grain, such as following the trajectory of each particle while detecting and simulating their collision with their

neighborhood. In this model, particles are represented as soft spheres which may slightly deform during collisions. The frictional forces resulting from these interactions are limited by the Coulomb criterion beyond which particles slide over each other. The objective of this work was twofold : first, contributing to the parallelization of the code using a static domain decomposition method, which consists of partitioning the computational domain into subdomains of identical size assigned to a processor, and then validating the model using pre-existing experiments. The parallelization step consisted in making each processor independent so that informations on particles (index, position, linear and angular velocities) remain local. The interaction forces between particles are then calculated in each subdomain, allowing a local update of the position of each particle at each time step. However, as particles move freely within the global domain, thus from one processor to another, a communication is required between processors to transfer informations between neighboring subdomains, especially concerning particles located near the boundaries and intended to depend to another subdomain at the next time step. Communication between the different subdomains was implemented in the DEM code using an MPI interface. Synchronization of the algorithm controlling the messages exchange and non-blocking communication routines allowed us to significantly reduce the computation time and thus to simulate a number of particles 10 times greater for an equivalent computation time. Numerical simulations were then validated with the reference experiments of Lajeunesse *et al.* (2005) (Figure 4.1).

After having worked on the size and density segregation developed in granular flows through a postdoctoral project performed between the “Center of GeoHazards Studies” at the University of Buffalo in collaboration with Eliza Calder (Pr U, CGS, University of Buffalo, USA) and the Geological Survey of Japan at the National Institute of Advanced Industrial Science and Technology (AIST) in collaboration with Shinji Takarada (CR AIST, GSJ, Tsukuba, Japan), I started working through a third post-doctoral position conducted at the “Institut de Mécanique des Fluides de Toulouse” in collaboration with François Charru (Pr U, IMFT, Paul Sabatier University) and John Sherwood (Pr

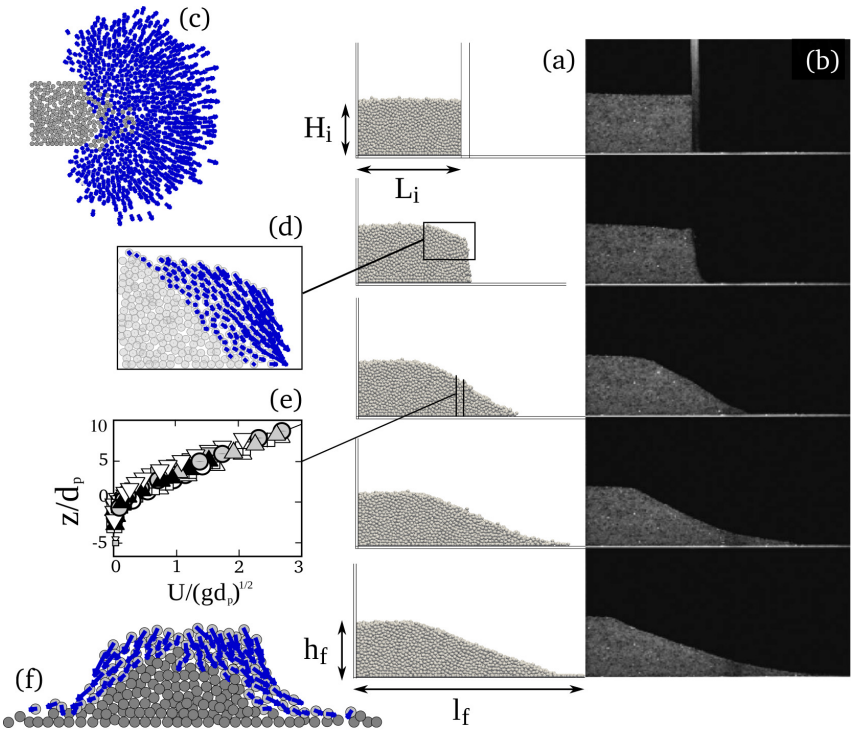

Figure 4.1

Image sequences of the temporal evolution of the collapse of a granular column reproduced (a) numerically and (b) experimentally [Lajeunesse *et al.* (2005)]. (c) Lateral spreading of unconfined flows ; (d) interface between the static region and the mobile zone at the heart of the avalanche ; (e) normalized velocity profiles determined for all experiments ; (f) transverse profile illustrating the lateral spreading of unconfined collapses.

U, DAMTP, University of Cambridge) on the sand transport in pipes through a theoretical study. The set of equations developed in this context describes a quasi-parallel flow confined between a slowly deformable sandy layer at the base and the upper wall of the pipe. The model assumes that the momentum is instantaneously diffused in the transverse direction so that the flow can be locally considered as fully established, without imposing a low Reynolds number. The solution of the problem involves an asymptotic expansion around a small parameter ϵ, which corresponds to the local slope and the bed aggradation rate. This decomposition allows to approximate the flow by a dominant solution, termed a

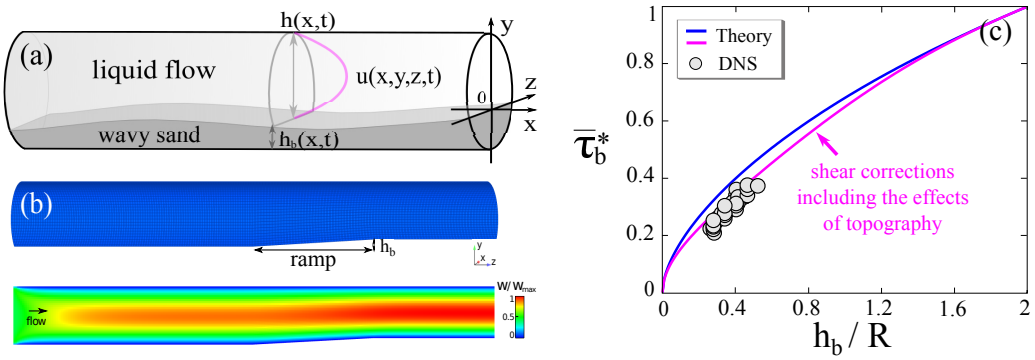

Figure 4.2

(a) Scheme of the theoretical model. (b) Simulation performed with Neptune in a truncated pipe with a gentle slope formed by the sandy layer. (c) Comparison between the theoretical prediction of the basal shear τ_b calculated at the zeroth order (*i.e* down a flat bottom) and including a first-order correction (*i.e*, the effect of a weak local slope) and the result of direct numerical simulations (DNS) obtained for different Reynolds numbers and sand heights h_b.

zeroth-order solution, that considers a negligible slope at each position and at each time, and a correction, termed a *first-order* correction, that includes a viscous and inertial term proportional to $\epsilon(x,t)$. The complete analytical expression of the shear stress τ_b at the bed surface was first obtained for the reference case of a flat channel. Considering the more realistic case of a partially filled cylindrical pipe, the analytical solution obtained at the dominant order was corrected by a numerical solution determined using the finite element method (using FreeFEM^{++}). These predictions were then compared with results obtained from direct numerical simulations, performed with the Neptune code available at IMFT, which imply the resolution of the complete Navier-Stokes equations to test the assumptions relevance. Theoretical results obtained were found to be in good agreement with simulations (Figure 4.2). The integration of these equations on the pipe section allowed us to obtain an operational 1D theoretical model whose coupling with the sandy layer is achieved through τ_b. A stability study, led by John Sherwood, then allowed us to determine the operational conditions favorable to oil extraction (patterns degrowth) and

to predict the characteristics of the sedimentary structures.

4.5 Teaching activities

Parallely to my research activity, I complete a teaching activity primarily based on lectures conducted in the initial and continuing University programs of the Bachelor degree in Physics-Chemistry-Geosciences ; in Life Sciences and PACES ; in Geosciences and Environment ; in the professional Bachelor degree, CAPES, as well as in the Master degree devoted to Water Sciences (LMD program), as well as in IUTs. This volume of teaching represents around 200-220 hours per year. The courses primarily focus on the study of geophysics (Internal Earth, Geophysics, Natural Hazards, Floods and Dam Failures), in the form of lectures, tutorials, practical and field works. Since my employment at the University of Tours, I have had the opportunity to create and implement all the teachings I made in the Bachelor and Master of Sciences programs devoted to environmental geosciences. I was also appointed as manager of the 1^{st} Year (L1-SVT) upon my arrival in 2015 for a period of 5 years. The detail of teachings taught is summarized in the following table 4.1.

Year	Degree	Diploma	Topic	Format	Num.	Vol.
2014–2016	BSc 1	SVT	Geosciences	12hCM–36hTD	670	58
	BSc 1	STU	Planetology	10hCM–6hTD	70	21
	BSc 2	IUT	Geosciences	3hCM–8hTD	30	12
	BSc 2	STU	Planetology	6hCM/Obs.	40	13
	BSc 2	STU	Comm.	TD	40	12
	BSc 2	STU	Geodynamics	Field work	40	35
	BSc 3	STU	Sed. Basins	16hCM-4hTD-4hTP	20	32
	BSc 3	STU	Risks	9hCM-6hTD-2hTP	60	23
	BSc 3	PRO	Tutoring	Internships	3	7
2016–2018	BSc 1	SVT	Internal Earth	6hCM–26hTD	600	42
	BSc 1	SVT	Risks	6hCM-20hTD-6hTP	600	42
	BSc 1	STU	Planetology	Observatory	70	4
	BSc 1	STU	Comm.	TD	70	4
	BSc 2	STU	Volcanology	CM	35	15
	BSc 2	STU	Geosciences	Field work	35	48
	BSc 3	STU	Marine Geo.	12hCM–4hTP	20	22
	BSc 3	STU	Risks	6hCM–6hTD	20	15
	BSc 3	PRO	Tutoring	Internships	3	7
2018–2022	BSc 1	PCG	Internal Earth	6hCM-30hTD-12hTP	180	51
	BSc 1	SVT	Comm.	TD	70/530	28
	BSc 2	STE	Earth Phys.	12hCM–20hTD	35	38
	BSc 2	STE	Volcanology	Field work	35	28
	BSc 3	STE	Fluid Dyn.	20hCM–12hTD	20	42
	BSc 3	STE	Risks	6hCM–4hTD	20	13
	MSc 2	STE	Flooding	6hCM–4hTD	12	13
	MSc 2	STE	Insertion	TD	12	3
	MSc 2	STE	Project	Internships	3	18
2015–2019	BSc 1	SVT	Responsability	Organisation	600/70	12

Table 4.1

Teaching service performed at the University of Tours.

Chapitre 5

Concluding remarks & prospects

This manuscript synthesizes the main research that I developed since my arrival as associate professor at the University of Tours and I am still conducting, while summarizing my career path including my supervision experiences. The first research project was developed with the aim of describing the role of the particle concentration as well as that of the particle inertia on the sedimentation velocity in fluid-solid suspensions. One of the specificities of this work was the use of fluidization techniques to generate well-calibrated homogeneous suspensions in a stable regime and to vary the mixture concentration over a wide range, from the dilute regime to the packing state. The dimensional analysis exposes that the sedimentation of suspensions depends on four non-dimensional groups : ϕ_s, ϕ_s/ϕ_{pack}, $\mathcal{R}e$, $\mathcal{S}t_0$. When the Reynolds number is low, which is the case for the sedimentation processes studied in suspensions made with fine particles, the problem only depends on ϕ_s, ϕ_s/ϕ_{pack}, and $\mathcal{S}t_0$. By varying these non-dimensional groups over a wide range, we obtained a unique, universal law valid in the low Reynolds-number regime, which indicates that the mean sedimentation (or fluidization) velocity in a homogeneous suspension can be obtained from the theoretical velocity of an isolated particle settling in a pure fluid at rest, to which a density correction (which affects the buoyancy force acting on the particle) and a viscosity correction (which affects the drag force acting on

the particle as well as its local agitation relative to that of the fluid) are applied. This physical model comes down to describing the settling of a particle into an equivalent fluid with properties similar to those of the suspension. The next step of this work may require the extension of this law to situations where the fluid inertia impacts the fluidization/sedimentation velocity, thus varying $\mathcal{R}e$ over a wide range. Previous experiments of gas-solid suspensions presented in this manuscript cover situations where $\mathcal{R}e \ll 1$, while experiments of liquid-solid suspensions made with particles of diameter of few hundreds of microns (typically GB^3 with water), also presented in this manuscript, range at the upper limit of this regime, where $\mathcal{R}e = \mathcal{O}(1)$. Additional experiments of liquid-solid suspensions, made with coarser (millimeter-sized) particles in a non-confined reservoir using different types of particles and fluids, are required to explore situations where $\mathcal{R}e > 1$. In such experiments, fluidization and sedimentation processes will be investigated, while similarly varying ϕ_s, ϕ_s/ϕ_{pack}, and $\mathcal{S}t_0$ over a wide range. The maximum expansion rate of the mixture ϕ_{low}/ϕ_{pack} will be also analyzed to describe the effect of $\mathcal{R}e$ on the limit of the bed stability. Moreover, if this approach allows the determination of the sedimentation viscosity, the use of a well-suited rheometer made with a rotating immersed spindle will allow the exploration of the shear viscosity of suspensions made with fine particles for a wide range of ϕ_s, ϕ_s/ϕ_{pack}, $\mathcal{S}t_0$, and could be explored with coarser particles, *i.e* at higher $\mathcal{R}e$, while proposing a systematic comparison of the sedimentation and shear viscosities in many different situations.

As long as the mixture remains homogeneous, we can describe the velocity of a macroscopic sphere (*i.e* much larger than the particles) falling into the suspension, considering the equivalent fluid described by the mixture density and effective sedimentation viscosity and the size ratio between the particles and the sphere. The investigation of the bed surface fluctuations allowed us to highlight the propagation of concentration waves within the suspension, traveling from the base to the surface. Their wavelength λ can be interpreted as a correlation length which corresponds to the size of the heterogeneities. When the bed is concentrated and particles are in contact with each other, λ diverges and highlights a

transition towards the packing state analog to a jamming process. When the suspension is dilute, λ significantly increases again, indicating that the bed becomes heterogeneous and starts sloshing, as U_f starts deviating from U_{sed}, until becoming unstable when the typical size of the heterogeneities may become of the order of that of the reservoir, which may provide a way to define the transition towards the heterogeneous regime.

After having described in detail the properties of static suspensions generated in the reservoir, we explored their behavior when released down a horizontal and impermeable flume. To describe experiments of free-surface flows made with gas-solid and liquid-solid suspensions taken at different concentrations, we proposed a physical model in which a quasi-parallel flow travels at high Reynolds number and progressively settles in the Stokes flow regime during the dominant phase of transport. The mixture, considered as homogeneous, is assumed to move and sediment at constant speed, while forming a deposit of constant slope that can be predicted from the ratio of the two characteristic velocities, U_{agg} and $U_{\mathcal{F}}$. The deposition velocity is supposed to not being disturbed by the flow, such as being similar to that measured in a static suspension of same concentration. Preliminary results of numerical simulations of liquid-solid experiments highlight that both the kinematics and deposits shape can be satisfyingly predicted by the model, provided that the mixture agitation does not disturb the particle deposition. The next step of this work will consist in carefully testing the model using experiments of both gas-solid and liquid-solid suspension flows, while improving when necessary the flow description, by possibly modifying the shape of the velocity profile, or considering a variable concentration $\Phi_s(x,t)$ and thus a variable deposition rate $U_{sed}(x,t)$ during propagation. Modifying the boundary conditions in experiments, namely filling the flume with water, allowed us to reproduce immersed suspension flows which gave rise to the formation of turbidity currents. Their dynamics, expansion, and life-span might be controled by that of the upper cloud which requires the description of the particle erosion from the suspension, and their sedimentation from a dilute, agitated dispersion, which may principally depend on $\mathcal{R}e$ and $\mathcal{S}t_0$, as the cloud concentration may remain constant, independently of that of the

suspension. Experiments of liquid-solid suspensions performed with various particles at different concentrations will be carefully analyzed in this way, with the aim of proposing a more general model of both immersed and free-surface flows.

Once accumulated down the valley, deposits can form a sedimentary reservoir which is likely to be reworked by upcoming extreme events. If these deposits outcrop on the surface, they can be eroded and resuspended in upcoming hazardous flows. If these deposits are located at a few dozen meters deep, such as having been formed a few thousand years ago, they can be reworked and eroded by internal seepage flows, during periods of high water levels, and ultimately rise the surface to settle down river banks or drive to a superficial soil collapse which can ultimately impact the safety of the hydraulic facility emplaced to protect proximal populations. In the aim of understanding the origin and distribution of erosion processes developed beneath a diked river, we conducted geophysical observations of the paleo-environment of the river which provided an overview of the situation, while representing the starting point for geomechanical simulations. Scenarii of internal seepage flows induced by successive episodes of floods, causing the erosion of the soil located beneath the river bed and dikes, were reproduced numerically and allowed us to explain the distribution of the surface signatures along the plain. As predictions, mainly based on the description of the soil rearrangement during floods, may be important for hazards studies developed in the context of land-use planning, a future important step may consist in proposing a more general erosion law gained from small-scale experiments and similarly based on a dimensional analysis that will allow us to define the relevant non-dimensional groups of the problem, while making them vary over a wide range of values. Experiments of annular plane Couette flows developed above an erodible bed of particles, involving different types of sediments and fluids, could be conducted in the laboratory RECOVER. Moreover, another important step will consist in observing the spatio-temporal evolution of the subsoil during floods. In doing so, the settlement of an observation set-up, capable of recording internal seepage flows, the water table level, as well as the soil movements, is being initiated down the Agly floodplain.

Bibliographie

Abrahamsen, A. R. & Geldart, D. 1980 Behaviour of gas-fluidized beds of fine powders part I. Homogeneous expansion. *Powder Technology* **26** (1), 35–46.

Al-Naafa, M. & Selim, M. S. 1992 Sedimentation of monodisperse and bidisperse hard-sphere colloidal suspensions. *AIChE Journal* **38** (10), 1618–1630.

Amin, A. 2022 Dynamics and sedimentation of fluid-solid suspensions. PhD thesis, Université de Tours (UT).

Amin, A., Girolami, L. & Risso, F. 2021 On the fluidization/sedimentation velocity of a homogeneous suspension in a low-inertia fluid. *Powder Tech.* **391**, 1–10.

Amin, A., Girolami, L. & Risso, F. 2022 Fall of a large sphere in a suspension of small fluidized particles. *Physical Review Fluids* **7** (8), L082301.

Andrews, B. J. & Manga, M. 2012 Experimental study of turbulence, sedimentation, and coignimbrite mass partitioning in dilute pyroclastic density currents. *Journal of Volcanology and Geothermal Research* **225**, 30–44.

Banchio, A., Bergenholtz, J. & Nägele, G. 1999 Rheology and dynamics of colloidal suspensions. *Physical review letters* **82** (8), 1792.

Batchelor, G. 1972 Sedimentation in a dilute dispersion of spheres. *Journal of fluid mechanics* **52** (2), 245–268.

Batchelor, G. 1988 A new theory of the instability of a uniform fluidized bed. *Journal of Fluid Mechanics* **193**, 75–110.

Batchelor, G. & Green, J.-T. 1972 The hydrodynamic interaction of two small freely-moving spheres in a linear flow field. *Journal Fluid Mech.* **56** (2), 375–400.

Berthon, C., Foucher, F. & Morales, T. 2015 An efficient splitting technique for two-layer shallow-water model. *Numerical Methods for Partial Differential Equations* **31** (5), 1396–1423.

Bondesan, A., Girolami, L., James, F. & Rousseau, L. 2025 A three-layer model for the flow of particulate suspensions driven by sedimentation. *Physics of Fluids* **37**, doi :10.1063/5.0261889.

Bonelli, S. 2012 *Erosion of geomaterials*. John Wiley & Sons.

Bonelli, S. 2013 *Erosion in geomechanics applied to dams and levees*. Wiley & Sons.

Bonelli, S. & Girolami, L. 2024 Internal erosion of sandy gravel and occurence of open-framework gravels in the subsoil of a river dike. *Geomechanics for Energy and Environment* pp. 100690, doi :10.1016/j.gete.2025.100690.

Branney, M. J. & Kokelaar, B. P. 2002 Pyroclastic density currents and the sedimentation of ignimbrites. Geological Society of London.

Brosch, E. & Lube, G. 2020 Spatiotemporal sediment transport and deposition processes in experimental dilute pyroclastic density currents. *Journal of Volcanology and Geothermal Research* **401**, 106946.

Castellanos, A., Valverde, J. & Quintanilla, M. 2001 Aggregation and sedimentation in gas-fluidized beds of cohesive powders. *Physical Review E* **64** (4), 041304.

Coulomb, C. A. 1785 Premier mémoire sur l'électricité et le magnétisme. *Histoire de l'Académie royale des sciences* **569**.

Davis, R. H. 1993 Microhydrodynamics of particulate : Suspensions. *Advances in colloid and interface science* **43** (1), 17–50.

Deng, Z., Girolami, L., Benahmed, N., Philippe, P., Bonelli, S. & Wang, G. 2025 Large-scale numerical insights of suffusion processes beneath river dikes : impact on erosion signatures. *Water Resources Research* (submitted).

Denlinger, R. P. & Iverson, R. M. 2001 Flow of variably fluidized granular masses across three-dimensional terrain : 2. numerical predictions and experimental tests. *Journal of Geophysical Research : Solid Earth* **106** (B1), 553–566.

Doyle, E., Hogg, A., Mader, H. & Sparks, R. 2008 Modeling dense pyroclastic basal flows from collapsing columns. *Geophysical Research Letters* **35** (4).

Druitt, T. H. & Kokelaar, B. P. 2002 The eruption of soufrière hills volcano, montserrat, from 1995 to 1999. Geological Society of London.

Dufek, J. 2016 The fluid mechanics of pyroclastic density currents. *Annual Review of Fluid Mechanics* **48** (1), 459–485.

Duvail, C. 2008 Expression des facteurs régionaux et locaux dans l'enregistrement sédimentaire d'une marge passive. exemple de la marge du golfe du lion, étudiée selon un continuum terre-mer. PhD thesis, Université de Montpellier 2.

Einstein, A. 1906 Neue bestimmung der moleküldimensionen. *Ann. Phys.* **19**, 289–306.

Einstein, A. 1911 Berichtigung zu meiner arbeit : Eine neue bestimmung der moleküldimensionen. *Ann. Phys.* **34**, 591–592.

Ergun, S. 1952 Fluid flow through packed colmuns. *Chem. Eng. Progress* **48** (2), 89–94.

Esposti Ongaro, T., Barsotti, S., Neri, A. & Salvetti, M. V. 2011 Large-eddy simulation of pyroclastic density currents. In *Quality and reliability of large-eddy simulations II*, pp. 161–170. Springer.

Fan, L.-S. & Zhu, C. 1999 *Principles of gas-solid flows*. Cambridge University Press, Port Chester, NY (United States).

Frankel, N. & Acrivos, A. 1967 On the viscosity of a concentrated suspension of solid spheres. *Chemical Engineering Science* **22** (6), 847–853.

Freundt, A. 2003 Entrance of hot pyroclastic flows into the sea : experimental observations. *Bulletin of Volcanology* **65** (2), 144–164.

Garner, S. & Fannin, R. 2010 Understanding internal erosion : a decade of research following a sinkhole event. *International Journal on Hydropower & Dams* **17** (3), 93.

Geldart, D. 1973 Types of gas fluidization. *Powder Technology* **7** (5), 285–292.

Giraud, M., Gatumel, C., Vaudez, S., Bernard-Granger, G., Nos, J., Gervais, T. & Berthiaux, H. 2020 Investigation of a granular bond number based rheological model for polydispersed particulate systems. *Chemical Eng. Sci.* **228**, 115971.

Girolami, L. 2008 Dynamique et sédimentation des écoulements pyroclastiques reproduits en laboratoire. PhD thesis, Clermont-Ferrand 2.

Girolami, L., Bonelli, S., Carozza, J.-M., Fogueng-Wafo, E., Burgat, J., Chaouch, N. & Valois, R. 2025 On the origin and distribution of internal erosion signatures in the floodplain protected by river dikes. *Journal Flood Risk Management* p. doi :10.1111/jfr3.70104.

Girolami, L., Bonelli, S., Valois, R., Chaouch, N. & Burgat, J. 2023 On erosion of the pervious foundation of flood protection dikes. *Water* **15** (21), 3747.

Girolami, L., Druitt, T., Roche, O. & Khrabrykh, Z. 2008 Propagation and hindered settling of laboratory ash flows. *Journal of Geophysical Research* **113** (B2).

Girolami, L. & Risso, F. 2019 Sedimentation of gas-fluidized particles with random shape and size. *Physical Review Fluids* **4** (7), 074301.

Girolami, L. & Risso, F. 2020 Physical modeling of the dam-break flow of sedimenting suspensions. *Physical Review Fluids* **5** (8), 084306.

Girolami, L., Risso, F., Amin, A., Rousseau, L., Bondesan, A. & Bonelli, S. 2024 Sedimentation of short-lived fluid-solid suspensions. *Physics of Fluids* **36** (11).

Girolami, L., Roche, O., Druitt, T. H. & Corpetti, T. 2010 Particle velocity fields and depositional processes in laboratory ash flows, with implications for the sedimentation of dense pyroclastic flows. *Bulletin of Volcanology* **72**, 747–759.

Guazzelli, E. 2024 Granular suspension : From single fluid to two-phase particulate systems. In *Physics of Granular Suspensions : Micro-mechanics of Geophysical Flows*, pp. 3–12. Springer.

Guazzelli, É. & Pouliquen, O. 2018 Rheology of dense granular suspensions. *Journal of Fluid Mechanics* **852**, 35–73.

Ham, J., Thomas, S., Guazzelli, E., Homsy, G. & Anselmet, M.-C. 1990 An experimental study of the stability of liquid-fluidized beds. *International journal of multiphase flow* **16** (2), 171–185.

Hinch, E. J. 1977 An averaged-equation approach to particle interactions in a fluid suspension. *Journal of Fluid Mechanics* **83** (4), 695–720.

Hoblitt, R. P. 1986 *Observations of the eruptions of July 22 and August 7, 1980, at Mount St. Helens, Washington*, , vol. 1335. US Government Printing Office.

Holzer, T. L. & Clark, M. M. 1993 Sand boils without earthquakes. *Geology* **21** (10), 873–876.

Koch, D. L. & Hill, R. J. 2001 Inertial effects in suspension and porous-media flows. *Annual Review of Fluid Mechanics* **33** (1), 619–647.

Kramer, O. J. I., de Moel, P. J., Baars, E. T., van Vugt, W. H., Padding, J. T. & van der Hoek, J. P. 2019 Improvement of the Richardson-Zaki liquid-solid fluidisation model on the basis of hydraulics. *Powder Technology* **343**, 465–478.

Krieger, I. M. & Dougherty, T. J. 1959 A mechanism for non-Newtonian flow in suspensions of rigid spheres. *Transactions of the Society of Rheology* **3** (1), 137–152.

Labaune, C., Tesson, M., Gensous, B., Parize, O., Imbert, P. & Delhaye-Prat, V. 2010 Detailed architecture of a compound incised valley system and correlation with forced regressive wedges : Example of late quaternary têt and agly rivers. *Sedimentary Geology* **223** (3-4), 360–379.

Lajeunesse, E., Monnier, J. & Homsy, G. 2005 Granular slumping on a horizontal surface. *Physics of fluids* **17** (10).

Larrieu, E., Staron, L. & Hinch, E. 2006 Raining into shallow water as a description of the collapse of a column of grains. *Journal of Fluid Mechanics* **554**, 259–270.

Leighton, D. & Acrivos, A. 1987 The shear-induced migration of particles in concentrated suspensions. *Journal of Fluid Mechanics* **181**, 415–439.

Levine, A. H. & Kieffer, S. W. 1991 Hydraulics of the august 7, 1980, pyroclastic flow at mount st. helens, washington. *Geology* **19** (11), 1121–1124.

Li, Y., Craven, J., Schweig, E. S. & Obermeier, S. F. 1996 Sand boils induced by the 1993 mississippi river flood : could they one day be misinterpreted as earthquake-induced liquefaction ? *Geology* **24** (2), 171–174.

Liang, Y., Yeh, T.-C. J., Wang, Y.-L., Liu, M., Wang, J. & Hao, Y. 2017 Numerical simulation of backward erosion piping in heterogeneous fields. *Water Resources Research* **53** (4), 3246–3261.

Loughlin, S., Calder, E., Clarke, A., Cole, P., Luckett, R., Mangan, M., Pyle, D., Sparks, R., Voight, B. & Watts, R. 2002 Pyroclastic flows and surges generated by the 25 june 1997 dome collapse, soufrière hills volcano, montserrat. *Geological Society, London, Memoirs* **21** (1), 191–209.

Lube, G., Huppert, H. E., Sparks, R. S. J. & Freundt, A. 2005 Collapses of two-dimensional granular columns. *Physical Review E ,ÄîStatistical, Nonlinear, and Soft Matter Physics* **72** (4), 041301.

Marchi, M., Martínez, M. F. G., Gottardi, G. & Tonni, L. 2021 Field measurements on a large natural sand boil along the river po, italy. *Quarterly Journal of Engineering Geology and Hydrogeology* **54** (4), qjegh2020–097.

Maron, S. H. & Pierce, P. E. 1956 Application of ree-eyring generalized flow theory to suspensions of spherical particles. *Journal of colloid science* **11** (1), 80–95.

Massimilla, L. & Donsì, G. 1976 Cohesive forces between particles of fluid-bed catalysts. *Powder Technology* **15** (2), 253–260.

Maude, A. & Whitmore, R. 1958 A generalized theory of sedimentation. *British journal of applied physics* **9** (12), 477.

Mériaux, P., Monier, T., Tourment, R., Mallet, T., Lopes, S. P., Maurin, J. & Pinhas, M. 2012 L'auscultation des digues de protection contre les inondations : un concept encore à inventer. In *Colloque CFBR," Auscultation des barrages et des digues : pratiques et perspectives"*, pp. 51–67. CFBR.

Morton, L. W. & Olson, K. R. 2015 Sinkholes and sand boils during 2011 record flooding in cairo, illinois. *Journal of Soil and Water Conservation* **70** (3), 49A–54A.

Nguyen, T.-K., Benahmed, N., Hicher, P.-Y. & Nicolas, M. 2014 Influence of fines content on the onset of instability and critical state line of silty sand. In *International Workshop on Bifurcation, Degradation in Geomaterials*, pp. 113–120. Springer.

Ongaro, T. E., Orsucci, S. & Cornolti, F. 2016 A fast, calibrated model for pyroclastic density currents kinematics and hazard. *Journal of Volcanology and Geothermal Research* **327**, 257–272.

Pierson, T. C., Daag, A. S., Delos Reyes, P., Regalado, M. T. M., Solidum, R. U. & Tubianosa, B. S. 1996 Flow and deposition of posteruption hot lahars on the east side of mount pinatubo, july–october 1991. *Fire and Mud : eruptions and lahars of Mount Pinatubo, Philippines* pp. 921–950.

Pu, C., Liu, F. & Wang, S. 2021 Liquid force and rupture distance between two particles. *Advances in Materials Science and Engineering* **2021** (1), 3542686.

Pudasaini, S. P. 2012 A general two-phase debris flow model. *Journal of Geophysical Research : Earth Surface* **117** (F3).

Pudasaini, S. P. & Krautblatter, M. 2021 The mechanics of landslide mobility with erosion. *Nature communications* **12** (1), 6793.

Rampino, M. R. & Self, S. 1992 Volcanic winter and accelerated glaciation following the toba super-eruption. *Nature* **359** (6390), 50–52.

Reed, C. & Anderson, J. L. 1980 Hindered settling of a suspension at low reynolds number. *AIChE Journal* **26** (5), 816–827.

Rhodes, M. 1998 Mixing and segregation. *Introduction to particle tech.* pp. 223–240.

Richardson, J. F. & Zaki, W. N. 1954 The sedimentation of a suspension of uniform spheres under conditions of viscous flow. *Chemical Engineering Science* **3** (2), 65–73.

Robbins, B. & Griffiths, D. 2021 A 2d, adaptive finite element approach for simulation of backward erosion piping. *Computers and Geotechnics* **129**, 103820.

Robbins, B. A., van Beek, V. M., López-Soto, J. F., Montalvo-Bartolomei, A. M. & Murphy, J. 2018 A novel laboratory test for backward erosion piping. *International Journal of Physical Modelling in Geotechnics* **18** (5), 266–279.

Robbins, B. A., Sharp, M. K. & Corcoran, M. K. 2015 Laboratory tests for backward erosion piping. In *Geotechnical Safety and Risk V*, pp. 849–854. IOS Press.

Roche, O. 2012 Depositional processes and gas pore pressure in pyroclastic flows : an experimental perspective. *Bulletin of Volcanology* **74**, 1807–1820.

Rousseau, L., Girolami, L., Risso, F. & Boussafir, M. 2025 Propagation of concentration waves in liquid-solid fluidized beds. *Physical Review Fluid* **in revision**.

Semmens, S. N. & Zhou, W. 2019 Evaluation of environmental predictors for sand boil formation : Rhine-meuse delta, netherlands. *Environmental Earth Sciences* **78**, 1–11.

Shimizu, H. A., Koyaguchi, T. & Suzuki, Y. J. 2019 The run-out distance of large-scale pyroclastic density currents : a two-layer depth-averaged model. *Journal of Volcanology and Geothermal Research* **381**, 168–184.

Shimizu, H. A., Koyaguchi, T., Suzuki, Y. J., Brosch, E., Lube, G. & Cerminara, M. 2021 Validation of a two-layer depth-averaged model by comparison with an experimental dilute stratified pyroclastic density current. *Bulletin of Volcanology* **83** (11), 73.

Sparks, R. S. J. 1976 Grain size variations in ignimbrites and implications for the transport of pyroclastic flows. *Sedimentology* **23** (2), 147–188.

Stokes, G. G. 1851 *On the effect of the internal friction of fluids on the motion of pendulums*. Pitt Press Cambridge.

Takahashi, A., Horikoshi, K. & Maruyama, T. 2017 Physical modelling of backward erosion piping in levee foundation subjected to repeated flooding. In *Book of*

Abstracts for 25th Meeting European Working Group on Internal Erosion in Embankment Dams & their Foundations, Delft, Netherlands, pp. 4–7.

Thouret, J.-C., Antoine, S., Magill, C. & Ollier, C. 2020 Lahars and debris flows : Characteristics and impacts. *Earth-Science Reviews* **201**, 103003.

Tourment, R., Benahmed, N., Nicaise, S., Meriaux, P., Salmi, A. & Rougé, M. 2018 Lessons learned on the damage on the levees of the agly river. analysis of the sand-boils phenomena. In *Twenty-Sixth International Congress on Large Dams*, pp. Q103_303–Q103_333. CRC Press.

Useo, K. 2024 Caractérisation expérimentale du comportement collectif de globules rouges : résistance au mouvement et migration. PhD thesis, Institut National Polytechnique de Toulouse.

Valentine, G. A. 2020 Initiation of dilute and concentrated pyroclastic currents from collapsing mixtures and origin of their proximal deposits. *Bull. Volcanology* **82** (2), 20.

Vallance, J. W. & Iverson, R. M. 2015 Lahars and their deposits. In *The encyclopedia of volcanoes*, pp. 649–664. Elsevier.

Van, M., Rosenbrand, E., Wopereis, L., Zwanenburg, C., Tourment, R. & Smith, P. 2022 Failure paths for levees-an international framework. *GeoHazards* **8**.

Van Beek, V. M., Knoeff, H. & Sellmeijer, H. 2011 Observations on the process of backward erosion piping in small-, medium-and full-scale experiments. *European Journal of Environmental and Civil Engineering* **15** (8), 1115–1137.

Wewer, M., Aguilar-López, J. P., Kok, M. & Bogaard, T. 2021 A transient backward erosion piping model based on laminar flow transport equations. *Computers and Geotechnics* **132**, 103992.

Zhang, L., Fu, Z., Li, J., Wang, R. & Bi, X. 2023 A review on multi-solids fluidized beds. *Powder Technology* **414**, 118091.

Brève synthèse du manuscrit

Mes activités de recherche portent principalement sur la modélisation physique d'événements extrêmes impliquant des suspensions fluide-particules soumis à des processus de sédimentation. L'objectif de ces travaux est de pouvoir décrire la phase d'arrêt et la mise en place d'une coulée de boue, d'une avalanche sous-marine, ou encore d'une coulée pyroclastique. J'ai choisi d'aborder cette problématique en utilisant différentes approches (expérimentale, numérique, théorique, ou encore naturaliste) avec toutefois une dominante expérimentale. L'intérêt de ce choix fût motivé par le développement de collaborations pluri-disciplinaires dans l'objectif de proposer des modèles prédictifs nécessaires à l'élaboration de simulations de grande échelle pour améliorer les cartes d'aléas liées à ces événements (Figure 5.1). Cette thématique de recherche, associée à des applications

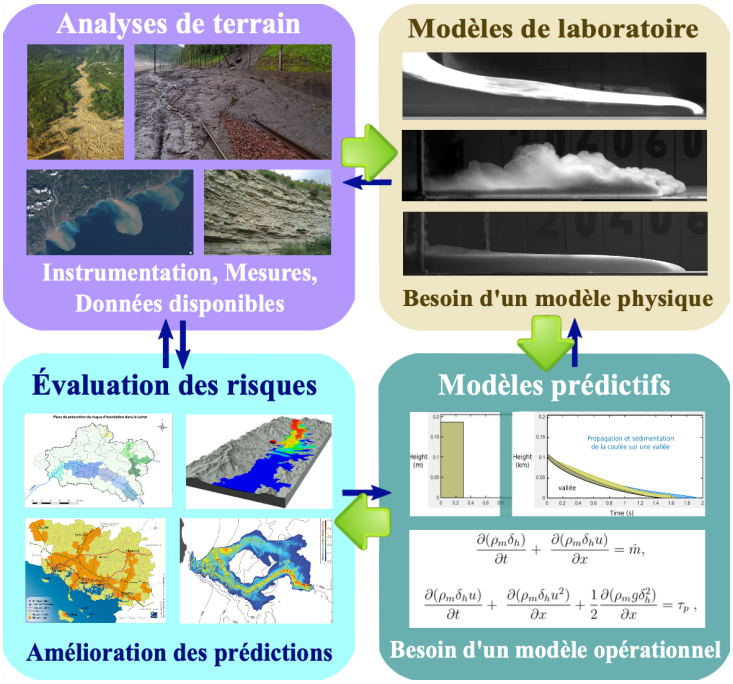

Figure 5.1

Différentes étapes nécessaires à la prédiction d'événements extrêmes.

aussi bien géophysiques qu'industrielles, me permet de travailler avec différentes structures (unités mixtes de recherche, établissements publics à caractère scientifique et tech-

nologique, bureaux d'études à vocation de recherche et de développement) et d'interagir avec des chercheurs dotés d'expertises variées (géosciences, géomécanique, mécanique des fluides, physique, mathématiques appliquées, archéologie), tout en développant des collaborations nationales et internationales. C'est en suivant cette ligne directrice que j'ai construit mes activités de recherche synthétisées dans cette annexe.

Depuis ma prise de fonction, j'ai mis en place une plateforme expérimentale, dotée d'une cuve de fluidisation, d'un canal hydraulique, d'une métrologie adaptée, d'un rhéomètre portatif, et dédiée à l'étude du transfert de sédiments sur le continuum Terre-Mer réalisé par le biais d'événements extrêmes survenant depuis les rivières anthropisées jusqu'aux milieux marins profonds. Dans ce projet, je m'intéresse plus particulièrement au rôle joué par la concentration en sédiments dans les suspensions sur leur dynamique de transport et de sédimentation. Pour cela, j'ai supervisé la conception et la construction d'un dispositif de type "rupture de barrage" (conceptualisé par Romain Morini, Ingénieur de Recherche sous ma direction) qui permet de reproduire des expériences inédites de coulées de boue et d'avalanches sous-marines (à concentration variable) que l'on étudie, depuis septembre 2020, à travers les parois transparentes du dispositif, en collaboration avec Frédéric Risso (Mécanicien des fluides à l'IMFT). Lorsque la fluidisation du mélange eau-sédiments est homogène et que le taux d'expansion est maîtrisé, l'ouverture de la trappe permet de relâcher la suspension dans le canal du dispositif. Durant sa propagation, le mélange se dépose progressivement jusqu'à son arrêt. L'analyse des expériences permet de mesurer la distance parcourue par la suspension, la durée et vitesse moyenne de l'écoulement, les champs et profils de vitesse sur l'épaisseur de l'écoulement, la vitesse de sédimentation des particules dans les différentes parties du mélange et la morphologie des dépôts en fin d'écoulement. Plusieurs séries d'écoulements, impliquant des mélanges homogènes de matériaux synthétiques ou naturels et d'eau, caractérisés par une fraction volumique de sédiments variable, ont été réalisées dans le cadre de la thèse de Ahmad Amin que j'ai encadré (directrice : Florentina Moatar, soutenue le 27.06.2022) et de plusieurs stages de Master 2 que j'ai supervisé. Ces résultats ont été comparés à ceux obtenus

à partir d'expériences d'écoulements de suspensions gaz-solides, réalisées au cours de ma thèse (au Laboratoire Magmas et Volcans sous la direction de Tim Druitt), et nous ont permis de proposer un modèle physique capable de prédire la durée et la longueur parcourue par la suspension, ainsi que la géométrie du dépôt laissé par l'écoulement, à partir des paramètres de contrôle des expériences. Ce modèle physique a pu être implémenté numériquement dans le cadre du post-doctorat d'Andrea Bondesan (que j'ai encadré avec François James) réalisé en 2020 et 2021, puis codé en C^{++} par Ibrahim Hmamou au démarrage de sa thèse que je co-dirige avec Carine Lucas et Olivier Delestre, ce qui nous permet désormais de pouvoir prédire numériquement ces expériences.

Les processus de sédimentation, qui contrôlent la phase d'arrêt des écoulements, ont été étudiés en détail dans le réservoir du dispositif et nous ont permis de proposer un modèle pour les suspensions homogènes stables, impliquant tous types de matériaux solides (synthétiques, naturels) et de fluides (air ou eau), pour les cas où l'inertie du fluide est négligeable, tel que :

$$U_{sed} = \underbrace{\frac{g(\rho_s - \rho_f)d^2}{18\ \mu_f}}_{\text{1.particule isolée, } U_0} \quad \underbrace{(1-\phi_s)}_{\text{2.densité du mélange}} \quad \underbrace{F_1\left(\frac{\phi_s}{\phi_{pack}}\right)}_{\text{3.concentration du mélange}} \quad \underbrace{F_2\left(\mathcal{S}t_0\right)}_{\text{4.inertie des particules}} \quad . \quad (5.1)$$

$$\text{avec } F_1\left(\frac{\phi_s}{\phi_{pack}}\right) = \frac{1}{\exp\left(1.9\frac{\phi_s}{\phi_{pack}}\right)+0.85\left(\frac{\phi_s}{\phi_{pack}}\right)^2\left(1-\frac{\phi_s}{\phi_{pack}}\right)^{-2/3}} \text{ et } F_2\left(St_0\right) = \frac{\frac{St_0}{45}+1}{\frac{3St_0}{45}+1}.$$

Ce modèle considère une particule isolée qui sédimente dans un fluide pur, au repos, dont les propriétés physiques (masse volumique, viscosité dynamique) sont semblables à celles de la suspension homogène considérée. Ceci nous permet de corriger la vitesse théorique de Stokes en tenant compte de la densité du mélange (qui affecte la force de flottabilité agissant sur chaque particule) et de la viscosité du mélange (qui affecte la force de trainée agissant sur chaque particule) qui implique deux corrections indépendantes : (1) une correction en concentration décrite par la fraction volumique solide normalisée par sa valeur au packing ; et (2) une correction sur l'inertie des particules décrite par le nombre de Stokes (qui compare le temps de réponse d'une particule relativement au

temps de sollicitation). Ce dernier paramètre sans dimension contrôle également la limite de stabilité du mélange. Plus les particules ont de l'inertie, plus le système se déstabilise rapidement, ce qui réduit la capacité d'expansion du mélange. Ces résultats permettent d'expliquer pourquoi les suspensions gaz-solides, caractérisées par un très grand nombre de Stokes, se dilatent peu alors que les suspensions liquide-solides, caractérisées par un faible nombre de Stokes, se dilatent davantage. Pour décrire ce mécanisme, nous avons alors observé les fluctuations de la surface du lit et pu mettre en lumière la propagation d'ondes de concentration au sein de la suspension, se propageant depuis la base vers la surface. Ces expériences ont été réalisées dans le cadre de la thèse de Loïc Rousseau que je co-encadre avec Frédéric Risso (directeur : Mohammed Boussafir, Laboratoire GéHCO). Leur longueur d'onde augmente avec la dilatation du lit si bien que le système devient instable lorsque celles-ci commencent à croître jusqu'à atteintre la taille du reservoir.

Depuis septembre 2022, je développe parallèlement une nouvelle thématique de recherche qui se concrétise par le développement de mon projet de délégation dans l'UMR RECOVER d'Aix-en-Provence, au côté de Stéphane Bonelli, qui me permet notamment de développer de nombreuses collaborations pluri-disciplinaires, nationales et internationales. Ce projet porte sur les processus d'érosion interne qui affectent les sols naturels sur lesquels reposent les digues de protection contre les inondations. Pendant les épisodes de crues et de décrues, de nombreuses signatures de surface (fuites, sand-boils, fontis) sont répertoriées à proximité des digues, laissant présumer de la formation de zones décompactées dans les dépôts fluviatiles superficiels, généralement très perméables. Contrairement aux ouvrages hydrauliques continuellement en charge, l'environnement des digues de protection souffrent d'un manque de système de surveillance adapté et réglementé. L'une des principales raisons de cette lacune est attribuée à la fréquence aléatoire des sollicitations hydrauliques, de courte durée, qui ne surviennent qu'en période de crue. Cette spécificité induit alors des verrous scientifiques et techniques qui limite l'organisation d'un système d'observation pertinent, à l'origine d'un manque de compréhension et de description physique des processus mis en jeu. C'est en nous plaçant à l'interface entre les communautés

de géomécanique, de géophysique, et de géomorphologie, que nous avons déployé une démarche d'observation et d'analyse, initiée par l'acquisition de mesures électriques in-situ, dans l'objectif de surmonter les verrous persistant de la littérature. Ces observations ont été réalisées sur les sols des digues de l'Agly (Pyrénées-Orientales). Construites dans les années 1970 pour protéger les populations de Claira, de Pia, et de Saint-Laurent-de-la-Salanque des risques d'inondation, elles constituent un véritable laboratoire naturel, sur lequel deux cas de rupture par brèche ont déjà été enregistrés en 1999 et 2013. Malgré les nombreuses expertises réalisées depuis 20 ans, ces phénomènes demeurent toujours inexpliqués.

Afin d'obtenir un panorama général des phénomènes, nous nous sommes tout d'abord intéressés au paléo-environnement de la rivière avant de concentrer nos efforts sur l'observation d'une zone d'érosion préférentielle principalement affectée pendant les crues, grâce à l'acquisition d'une cartographie surfacique de mesures de conductivité électrique du sol et de profils verticaux. La combinaison de ces mesures nous a permis d'obtenir la morphologie et les propriétés hydromécaniques du milieu, enrichies de carottes sédimentaires prélevées en pied de digue. Ces observations ont permis de mettre en évidence la présence d'une paléo-vallée incisée dans un substrat sablo-marneux, comblée de dépôts fluviatiles très perméables. La morphologie du réservoir sédimentaire, qui s'étend sur environ 350 mètres de large et environ 20 mètres de profondeur, représente le point de départ des simulations géomécaniques. Plusieurs scénarios d'écoulements internes générés lors d'épisodes successifs de crues, provoquant l'érosion des sols situés sous le lit de la rivière et sous les digues, ont été reproduits numériquement et nous ont permis d'expliquer la distribution des signatures de surface le long de la plaine. Ces travaux, en cours de valorisation, se poursuivent dans le cadre de la thèse d'Edouardo Fogueng-Wafo (que je co-dirige avec Corinne Curt et Stéphane Bonelli) et devront être complétés par des expériences de laboratoire réalisées sous conditions maîtrisées et la mise en place d'un atelier d'observation dans la plaine protégée des digues de l'Agly.